Felix Öhlinger, BSc

Precise orbit determination of BeiDou satellites focusing on solar radiation pressure models

Master's Thesis

to achieve the university degree of

Diplom-Ingenieur

Master's degree programme: Geodäsie

submitted to

Graz University of Technology

Supervisor

Univ.-Prof. Dr.-Ing. Torsten Mayer-Gürr

Institute of Geodesy

Graz, December 2021

Affidavit

I declare that I have authored this thesis independently, that I have not used other than the declared sources/resources, and that I have explicitly indicated all material which has been quoted either literally or by content from the sources used. The text document uploaded to TUGRAZonline is identical to the present master's thesis.

_____		_____
Date		Signature

Abstract

The Chinese BeiDou Navigation Satellite System (BeiDou) has become established as one of the four Global Navigation Satellite System (GNSS). Initially constructed as a regional system, China has launched 30 satellites within three years and declared the global system operational in 2020. A total of 55 satellites are in orbit, with three different types of orbit constellations. The precise determination of satellite orbits is a prerequisite for high-precision GNSS applications. However, the accuracy of BeiDou orbits cannot yet compete with established systems such as the Global Positioning System (GPS). Modeling of perturbing accelerations acting on the satellites caused by conservative and non-conservative forces is crucial for the quality of the orbit. Solar radiation pressure (SRP) is the dominant error source in precise orbit determination. The modeling of this influence is further complicated by the use of different satellite types and orbit constellations in the BeiDou system. The aim of this thesis was to integrate BeiDou into the processing of GNSS constellations at Graz University of Technology (TUG) and in particular to investigate the impact of SRP. Several SRP models were assessed and their applicability for BeiDou was analyzed. The period from June to December 2020 was investigated to determine the most suitable parameterization of the models for the different satellite types. The quality of the orbits was evaluated by internal orbit consistency checks, in the form of deviations at the midnight epoch of two consecutive 24 h orbit arcs. Based on the analyses conducted within the scope of this thesis, significant improvements in the orbit consistency could be achieved when specific variations of empirical SRP models were used. The BeiDou orbits obtained in this study are comparable to solutions by the analysis centers of the International GNSS Service (IGS).

Kurzfassung

Das chinesische System BeiDou hat sich als eines der vier globalen Satellitennavigationssysteme etabliert. Ursprünglich als regionales System konzipiert, hat China innerhalb von drei Jahren 30 Satelliten gestartet und das globale System im Jahr 2020 für einsatzbereit erklärt. Insgesamt befinden sich 55 Satelliten in den Umlaufbahnen, wobei drei verschiedene Arten von Orbitkonstellationen zum Einsatz kommen. Die genaue Bestimmung der Satellitenbahnen ist eine Voraussetzung für hochpräzise GNSS-Anwendungen. Jedoch kann die Genauigkeit der BeiDou-Orbits noch nicht mit etablierten Systemen wie dem Global Positioning System (GPS) mithalten. Die Modellierung der Störbeschleunigungen, welche durch konservative und nicht-konservative Kräfte auf die Satelliten einwirken, ist entscheidend für die Qualität der Orbits. Der Strahlungsdruck der Sonne ist die größte Fehlerquelle bei der präzisen Bahnbestimmung. Die Modellierung dieses Einflusses wird durch die Verwendung verschiedener Satellitentypen und Bahnkonstellationen im BeiDou-System zusätzlich erschwert. Ziel dieser Arbeit war es, BeiDou in die Prozessierung von GNSS-Konstellationen an der Technischen Universität Graz zu integrieren und insbesondere den Einfluss des Strahlungsdrucks der Sonne zu untersuchen. Es wurden verschiedene Arten von Strahlungsdruck-Modellen bewertet und ihre Anwendbarkeit für BeiDou analysiert. Der Zeitraum von Juni bis Dezember 2020 wurde untersucht, um die am besten geeignete Parametrisierung der Modelle für die verschiedenen Satellitentypen zu ermitteln. Die Qualität der Orbits wurde anhand von Prüfungen der internen Konsistenz der Satellitenbahnen in Form von Abweichungen zur Mitternachtsepoche von zwei aufeinanderfolgenden 24-Stunden Bahnbögen bewertet. Die im Rahmen dieser Arbeit durchgeführten Analysen ergaben, dass durch die spezifische Anpassung empirischer Modelle signifikante Verbesserungen in der Bahnkonsistenz erzielt werden konnten. Die in dieser Studie ermittelten BeiDou-Orbits sind qualitativ vergleichbar mit den Lösungen der Analysezentren des International GNSS Service (IGS).

Acknowledgement

First of all, I would like to thank my supervisor Univ.-Prof. Dr.-Ing. Torsten Mayer-Gürr for providing guidance, giving constructive feedback and showing patience during the course of this study.

I would particularly like to express my gratitude to Dipl.-Ing. Sebastian Strasser for his continuous support throughout the process of this thesis. His preceding work formed the basis of this study and since he functioned as my co-supervisor, I was able to benefit from his comprehensive knowledge and thoughtful advice. His effort at every stage of this project is highly appreciated.

My appreciation also goes the team of the working group Theoretical Geodesy and Satellite Geodesy of the Institute of Geodesy for their assistance with technical or software problems.

Finally, I would like to thank my parents for all their support throughout my studies and acknowledge my colleagues and friends for their encouragement.

Contents

Introduction

The BeiDou Navigation Satellite System (BeiDou) developed from a regional system applicable in the Asian-Pacific area to a global system in a relatively short period of time. Initiated in 2009, the constellation deployment of the global system started with the launch of two satellites in November 2017 and was formerly commissioned with 30 satellites in August 2020. Alongside the Global Positioning System (GPS), the Globalnaya Navigatsionnaya Sputnikovaya Sistema (GLONASS) and the European system Galileo, BeiDou is the fourth Global Navigation Satellite System (GNSS) providing positioning, navigation and timing services worldwide. The use of multi-constellation and multi-frequency observations will expand the the range of GNSS applications and enhance the accuracy, availability and reliability of existing services. In the field of geodesy, precise orbit determination is prerequisite for high-precision GNSS applications. The largest error source of precise orbit determination is the influence of solar radiation pressure (SRP). The Empirical CODE Orbit Model (ECOM) with a subset of five parameters is widely used for SRP modeling (Arnold et al., 2015). However, a common SRP model might not be appropriate for BeiDou due to the different orbit types and attitude modes adopted by the satellites. The objective of this thesis is to integrate BeiDou into the processing of GNSS constellations at Graz University of Technology (TUG) and to assess different empirical and analytical SRP models in order to find the most suitable approach for BeiDou.

Chapter 2 gives an overview about BeiDou. The development from a regional to a global navigation system is summarized and the coordinate and time system are described. The different satellite types and orbit constellations are presented together with the adopted attitude modes and reference frames. An overview of the signals and the existing BeiDou orbit solutions is given. Chapter 3 covers the processing strategy for precise orbit determination of GNSS satellites applied at TUG. It comprises orbit modeling and lists the forces that need be considered. Variational equations used during the linearization of the observation equations are depicted and an overview about the raw observation approach used for the processing is given. The different types of SRP models are presented in Chapter 4. Chapter 5 comprises the numerical analyses. The models and settings applied for preprocessing are listed and the analytical and empirical SRP models are assessed and evaluated in terms of internal orbit consistency. A summary of the analyses is given in Chapter 6 alongside possible improvements and incentives for further research.

BeiDou Navigation Satellite System

Following the United States and Russia, China was the third country to construct an independent satellite navigation system. First research was carried out by the end of the 1960s and the development of the system began in the 1990s (Sun et al., 2012). Besides the country's national security and economic development, the aim of the BeiDou Navigation Satellite System (BeiDou) is to provide continuous, reliable, and high-accuracy positioning, navigation and timing services to its users (China Satellite Navigation Office, 2019c).

BeiDou is independently developed and operated by China, but compatibility and interoperability with other Global Navigation Satellite Systems (GNSS) are being pursued to minimize interference and maximize mutual performance. As stated by Yang et al. (2011), the use of GNSS multi-constellation and multi-frequency observations will enhance the navigation accuracy, availability and continuity of the positioning, navigation and timing (PNT) service. This improvement can be attributed to an increased number of satellites and subsequently a decreased dilution of precision as well as less navigational blind areas caused by terrain or building sheltering. The overall GNSS integrity and reliability will also be improved, when multi-GNSS reception is used.

Analogous to other GNSS such as the U.S. Global Positioning System (GPS), the Russian Globalnaya Navigatsionnaya Sputnikovaya Sistema (GLONASS) or the European system Galileo, BeiDou is comprised of three major components: the space segment, the ground segment and the user segment. The space segment consists of satellites in three different orbit constellations: the geostationary Earth orbit (GEO) satellites, the inclined geosynchronous orbit (IGSO) satellites and the medium Earth orbit (MEO) satellites. The different satellite types and their orbit constellation will be discussed in Section 2.4. The ground segment comprises the master control station, monitoring stations and uplink stations (Yang et al., 2019a). The master control station collects and processes all data from the monitoring stations, determines satellite orbits and satellite clock biases and generates the navigation message. The radio determination satellite service (RDSS) and the short message service, which will be described in Section 2.1.1 are also carried out at the master control station. The monitoring stations provide the pseudorange and carrier

phase measurements for orbit determination and wide-area differential information. These measurements are transmitted to the master control station in real-time (Han et al., 2011). The navigation message and the wide-area differential corrections are transmitted to the satellites via the uplink stations. Another function of the uplink stations is the time synchronization of the satellite clocks. The user segment includes any terminals that can track BeiDou satellite signals for PNT or other provided services.

2.1 Development of BeiDou

The Chinese navigation satellite system BeiDou was gradually constructed following a "three-step" approach. Initially, the provided services were only applicable for users in the Asian-Pacific area, but they were extended for global usage. Following the BeiDou Navigation Satellite Demonstration System (BDS-1), the BeiDou Regional Navigation Satellite System (BDS-2) was established. On June 23, 2020, the last satellite was launched successfully, completing the constellation deployment of the BeiDou Global Navigation Satellite System (BDS-3) (China Satellite Navigation Office, 2020c). After a series of comprehensive tests, BDS-3 was formally commissioned on August 3, 2020 (China Satellite Navigation Office, 2020b). The three phases of development and the provided services of BeiDou will be described in the following sections.

2.1.1 BeiDou Navigation Satellite Demonstration System

The construction of BDS-1 began in 1994, and active regional services were provided by 2000 (Chengqi, 2012). The initial constellation was composed of two GEO satellites, launched in 2000 (Yang et al., 2017b). They were located at 80°E and 140°E, respectively. In 2003 a third satellite was added at 110.5°E for backup purposes. The service area of the BDS-1 covered China and its surrounding areas from longitude 70°E to 140°E and latitude 5°N to 55°N. The BDS-1 satellites had been operating until 2010 and were then substituted by BDS-2 satellites (Chengqi, 2012).

The functions provided by BDS-1 included positioning, a short message communication service and timing. Apart from that, the demonstration system was used to gain technical experience and train personnel. BDS-1 was used in fields such as surveying and mapping, telecommunications, water conservancy, transportation, fishery, prospecting, forest fire prevention and national security (Sun et al., 2012).

The basic principle of positioning of BDS-1 differs from the concept used by other satellite systems. Global Navigation Satellite Systems such as GPS, GLONASS or
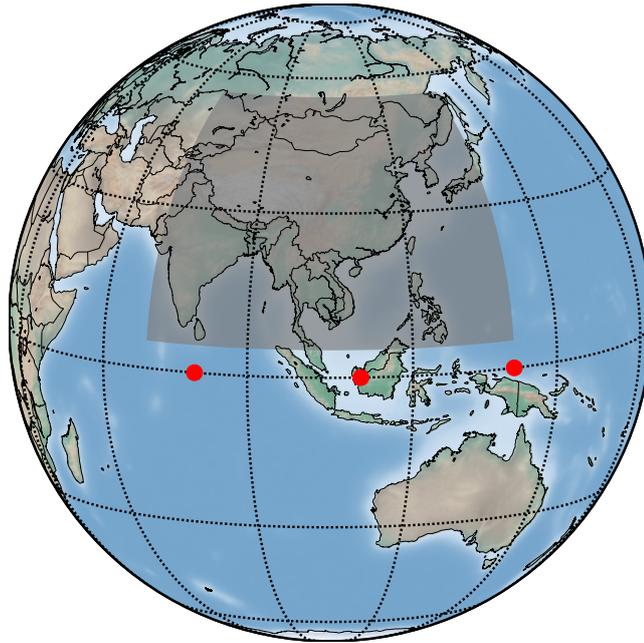
Fig. 2.1: The BDS-1 service area from longitude 70°E to 140°E and from latitude 5°N, as defined by Yang et al. (2017b). The red dots indicate the location of the GEO satellites.

Galileo use the concept known as radio navigation satellite service (RNSS). Here, the requested position is determined by the user. The three-dimensional coordinates and the receiver clock error can be obtained directly by measuring the pseudoranges from the receiver to at least four satellites. For more information about the mathematical models for positioning used by GNSS, refer to Hofmann-Wellenhof et al. (2007a). Since BDS-1 is based on a dual-satellite positioning mechanism, this direct approach is not possible. The concept of BDS-1 is known as radio determination satellite service (RDSS).

A profound description of the principle of RDSS and the different services provided by BDS-1 can be found in Yang et al. (2017b). The following paragraphs briefly summarize the basic characteristics. With RDSS, the determination of the user position is conducted at the master control station. It is based on the time measurement of the turn-around signal emitted by the master control station and responded by the user. The position can be determined with information about the height above the reference ellipsoid of the user queried by a digital database. This information is then sent back to the user. Since the transmit and receive times are measured by the same clock at the master control stations, clock offsets do not have to be considered. BDS-1 is not able to provide dynamic positioning and therefore cannot be called a navigation system but rather a positioning system to determine the location of the user. The horizontal positioning accuracy is 20 m to 100 m.

Besides providing user position information, the master control station also performs satellite orbit determination, short message communication and timing. Precise time corrections to synchronize the users with the BeiDou system time (BDT) are calculated and transmitted to the user. BDT is discussed in more detail in Section 2.3. Two different timing services are provided by BDS-1: one-way and two-way timing. The timing accuracies are 100 ns and 20 ns, respectively.

BDS-1 also included a satellite-based augmentation system (SBAS). Precise satellite orbits, grid ionospheric corrections and the equivalent satellite clock corrections for GPS were processed at the master control station and the corresponding corrections were broadcasted via the GEO satellites.

2.1.2 BeiDou Regional Navigation Satellite System

In 2004 the construction of BDS-2 started, and by December 2012, the system became fully operational (Yang et al., 2017b). The first MEO satellite was launched in 2007 and the first GEO satellite in 2009. With a total number of 14 operational satellites, the regional service was established. The initial constellation consisted of five GEO satellites, five IGSO satellites and four MEO satellites. The GEO satellites are located at 58.75°E, 80°E, 110.5°E, 140°E and 160°E, respectively. The service area of BDS-2 covers 94.6 % of the Asia-Pacific region from longitude 55°E to 180°E and latitude 55°S to 55°N (Yang et al., 2018). BDS-2 is still being maintained, and the precise orbit determination of the satellites is the object of this study. For the current satellite constellation status refer to Section 2.4.

BDS-2 provides positioning, navigation and timing services based on the concept of passive RNSS, but also continues the active RDSS and short message communication services from BDS-1. All BDS-2 satellites broadcast signals on three distinct frequency bands for the RNSS. Triple frequency signals enable different frequency combinations and provide the basis for advanced GNSS processing techniques, which are especially beneficial for ambiguity resolution, cycle slip correction and precise positioning (Li et al., 2017). The signals used in BDS-2 are discussed in more detail in Section 2.6. Two different levels of service are provided by BDS-2. The open service is commonly accessible to civilians, and the authorized service offers enhanced PNT, communication and integrity services (Sun et al., 2012). The open service was specified to offer a horizontal and vertical positioning accuracy of better than 10 m at a 95 % confidence interval within the BDS-2 service area (China Satellite Navigation Office, 2013). Three modes of timing services are provided by BDS-2: RDSS one-way, RDSS two-way and RNSS one-way. The uncertainty of the one-way timing service is designed to be less than 50 ns, and that of the two-way timing service is less than 10 ns (Han et al., 2011).
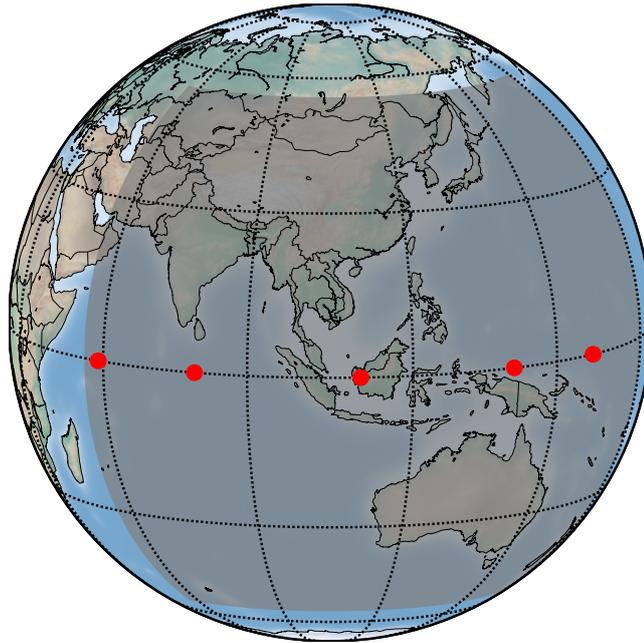
Fig. 2.2: The BDS-2 service area from longitude 55°E to 180°E and latitude 55°S to 55°N, as specified by Yang et al. (2018). The red dots indicate the location of the GEO satellites.

The BDS-2 GEO satellites still maintain the RDSS and additionally provide an improved SBAS service (Yang et al., 2017b). Apart from the features of the SBAS of BDS-1, the augmentations service of BDS-2 includes GPS and BeiDou signals and also provides integrity information.

2.1.3 BeiDou Global Navigation Satellite System

The development of the BeiDou Global Navigation Satellite System (BDS-3) began in 2009 and was formally commissioned in August, 2020 (China Satellite Navigation Office, 2020b). A demonstration system for BDS-3 was established between 2015 and 2016, consisting of three MEO satellites and two IGSO satellites. These satellites were launched in order to test the new payloads, the new signals and the new techniques designed for BDS-3 (Yang et al., 2018). The constellation deployment of BDS-3 started with the launch of two MEO satellites on November 5, 2017.

The global constellation of BDS-3 comprises 30 satellites, consisting of three GEO satellites, three IGSO satellites and 24 MEO satellites. The GEO satellites are located at 80°E, 110.5°E and 140°E, respectively. BDS-3 provides seven types of services. The global services include the fundamental service of positioning, navigation and timing (PNT) by RNSS, global short message communication (GSMC) and international search and rescue (SAR). The regional services comprise the satellite-based augmen-

tation system (SBAS), the ground-based augmentation system (GAS), the precise point positioning (PPP) and the regional short message communication (RSMC), which are provided in China and the surrounding areas from longitude 75°E to 135°E and latitude 10°N to 55°N (China Satellite Navigation Office, 2019c).

Analogous to its predecessor, BDS-3 provides an open service and an authorized service. The open service PNT is globally available but the overall performance is improved in the Asian-Pacific area (China Satellite Navigation Office, 2018a). The global positioning accuracy is better than 10 m, the velocity measurement accuracy is better than $0.2\,\mathrm{m\,s^{-1}}$ and the timing accuracy is better than 20 ns. The performance characteristics in the Asian-Pacific region of positioning, velocity measurement and timing are 5 m, $0.1\,\mathrm{m\,s^{-1}}$ and 10 ns, respectively.

2.2 Coordinate system

BeiDou adopts the BeiDou Coordinate System (BDCS), which follows the definition of the Chinese Geodetic Coordinate System 2000 (CGCS2000). The CGCS2000 is in accordance with the International Earth Rotation and Reference Systems Service (IERS) conventions and is aligned with the International Terrestrial Reference System (ITRS). The definition of the CGCS2000 is given in Yang (2009) and is summarized in the following paragraph.

The CGCS2000 is a right-handed, orthogonal, Earth-centered Earth-fixed (ECEF) system. Its origin coincides with the Earth's center of mass, including oceans and atmosphere. The initial orientation is constituted by the orientation of the Bureau International de l'Heure (BIH) at 1984.0. A no-net-rotation condition regarding the horizontal tectonic motions over the Earth ensures the time evolution of the orientation. The z-axis points in the direction of the IERS Reference Pole, and the intersection of the IERS Reference Meridian and the plane passing through the origin and normal to the z-axis defines the x-axis (Yang et al., 2017b). Meter is the unit of length. The defining constants of the reference ellipsoid used in the CGCS2000 are summarized in Table 2.1.

The constants of the reference ellipsoid used in different GNSS are not consistent. BeiDou differs in terms of GM, ω and f from those adopted by GPS. The value of a is the same as the one from GPS, but different values are used by GLONASS and Galileo. The variations in a and f usually do not affect the estimated position. Still, an incorrect value of GM in precise orbit determination could cause a maximum error of 2 m, and the wrong value of ω could cause orbit errors of up to several tens of meters (Yang et al., 2019a).

Tab. 2.1: The constants of the CGCS2000 as specified by China Satellite Navigation Office (2019a). The atmosphere is included in the gravitational constant GM.

Parameter		Value
semi major axis	a	$6\,378\,137.0\,\text{m}$
flattening	f	$1/298.257222101$
gravitational constant	GM	$3.986\,004\,418 \cdot 10^{14}\,\text{m}^3\,\text{s}^{-2}$
angular velocity	ω	$7.292\,115 \cdot 10^{-5}\,\text{rad}\,\text{s}^{-1}$

The Realization of CGCS2000 is denoted as China Terrestrial Reference Frame 2000 (CTRF2000) and is referenced to the International Terrestrial Reference Frame (ITRF) solution ITRF97 with the epoch of 2000.0 (Yang, 2009). BeiDou tracking stations and ITRF stations monitor the coordinate reference, using multi-GNSS receivers (Yang et al., 2019a). At least once a year, an integrated adjustment is performed where the coordinates and velocities of the stations are estimated, and the reference frame is updated. Additionally, coordinate parameters between BeiDou and other GNSS are determined to enhance the interoperability between the systems.

2.3 Time system

The time reference of BeiDou is called BeiDou system time (BDT) and is an internal and continuous uniform navigation time scale, accumulating without leap seconds (Han et al., 2011). The SI unit second is the basic unit adopted by BDT, and one week, defined as $604\,800\,\text{s}$, is the largest unit used. BDT is labeled by the week number and the second of week, starting from 0 to $604\,799$. Coordinated Universal Time (UTC) 00h 00min 00s, January 1, 2006, was the starting point of BDT.

BDT is maintained by the time and frequency system (TFS) at the master control station. The time-keeping is based on multiple hydrogen maser clocks, which realize BDT following the 'composite clocks' approach. The structure of the TFS is further elaborated in Han et al. (2011).

The time offset between BDT and UTC can be determined indirectly. BDT is aligned to the UTC realization of the National Timing Service Center of the Chinese Academy of Science (NTSC), and UTC(NTSC) aligns with UTC (Yang et al., 2019a). According to Han et al. (2011), BDT may be steered with an interposed frequency adjustment after a certain period, depending on the situation, to be as consistent as possible with UTC. The specified performance of BDT is summarized in Table 2.2.

Tab. 2.2: Performance specifications of BDT, as defined by China Satellite Navigation Office (2017c).

Parameter	Value
Time offset BDT-UTC	<100 ns (modulo 1 s)
Accuracy of correction BDT-UTC	5 ns
Stability of BDT	$<2 \cdot 10^{-14}$ / 1 d $<1 \cdot 10^{-14}$ / 7 d
Accuracy of satellite clock offset	2 ns

2.4 Satellite types and orbit constellation

As of November 2021, 15 BDS-2 satellites, four BDS-3-experimental satellites and 30 BDS-3 satellites are in orbit (China Satellite Navigation Office, 2021). The BDS-2 system comprises five GEO, seven IGSO and three MEO satellites. Two IGSO and two MEO BDS-3-experimental satellites are still in orbit. Three GEO, three IGSO and 24 MEO satellites form the BDS-3 constellation. All BDS-2 and BDS-3 satellites are operational besides the latest BDS-3 GEO satellite launched, which is still in testing mode. The BDS-3-experimental satellites have been part of the demonstration system and have been used to test new payloads and verify the design of BDS-3.

2.4.1 Orbit constellation

The GEO satellites are placed at an orbit altitude of 35 786 km directly over the equator. They orbit the Earth in the direction of the Earth rotation and exhibit an orbital period of one sidereal day (23 h 56 min). Since the orbital period of the GEO satellites matches the period of the rotation of the Earth relative to the fixed stars, they appear to be nearly stationary to a ground-based observer. However, the GEO satellites perform a certain north-south movement since they have a non-zero inclination of 0.7° to 1.7° (Steigenberger et al., 2013). Frequent orbital maneuvering is necessary to maintain the orbit of GEO satellites due to gravitational perturbations of Earth, Sun, and Moon. These station-keeping maneuvers are conducted in regular intervals. According to Xie et al. (2012), the station-keeping cycle in the east-west direction is between 25 and 35 days, the station-keeping cycle in the north-south direction is about two years. GEO satellites are well suited for regional navigation and satellite communication, but the accuracy of precise orbit determination is relatively low compared to other satellite constellations. Several factors contribute to this problem. The limitations of precise orbit determination of GEO satellites will be discussed in more detail in Section 5.3.1.
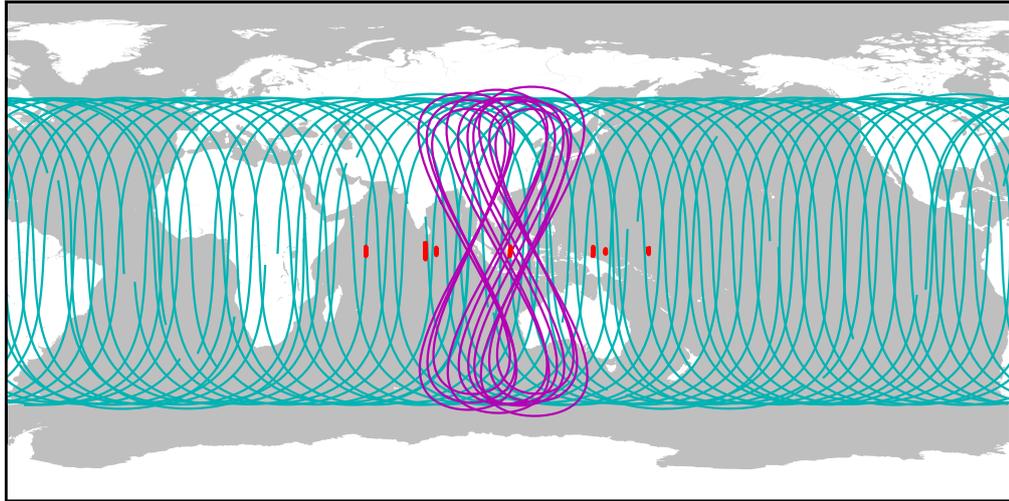
Fig. 2.3: Groundtracks of the BeiDou satellites on September 6, 2020. The cyan, purple and red trajectories indicate MEO, IGSO the GEO satellites, respectively.

The altitude of IGSO satellites is 35 786 km as well, but their orbit exhibits an inclination of 55° with respect to the equator. As a result, the continuously repeating ground tracks with a period of one sidereal day have a figure-of-eight shape that extends from latitude 55°S to 55°N. The satellites traverse the northern hemisphere in a clockwise direction and the southern hemisphere in a counter-clockwise direction. In order to control the equator crossing longitude (cross node), IGSO satellites also conduct orbit maneuvers in cycles of about half a year (Fan et al., 2017).

The MEO satellites orbit the Earth at an altitude of 21 528 km with an inclination angle of 55°. An orbital period of 12 h 53 min of the MEO satellites equals the completion of 13 revolutions in 7 days. The BDS-3 satellites are part of a 24/3/1 Walker constellation (Yang et al., 2018). The triplet 24/3/1 denoting the constellation implies that 24 satellites are evenly distributed in three orbital planes and that the phase difference between adjacent orbital planes is equally spaced. In this constellation, the ascending nodes of the orbital planes are separated by 120°. In order to avoid collision or interference at plane intersections, the relative spacing between satellites in neighboring planes, which corresponds to the change in true anomaly, is 15°. The BDS-2 MEO satellites have been placed between the official slot positions of the BDS-3 MEO satellites (International GNSS Service, 2021c).

2.4.2 Spacecraft characteristics

BDS-2 satellites

The MEO and IGSO satellites of BDS-2 utilize the DongFangHong-3 (DFH-3) satellite platform, developed by the China Academy of Space Technology (CAST). The BDS-2 GEO satellites adopt a slightly modified version (DFH-3A), which carries complementary equipment in addition to the navigation payload (Xie et al., 2012). The DFH-3 bus is three-axis stabilized and has a hexahedral shape. The satellite platform is equipped with an apogee boost motor and a liquid propulsion system used for initial orbit insertion and orbit keeping maneuvers and includes subsystems for power supply and distribution, thermal control, tracking, telemetry as well as attitude and orbit control (Yang et al., 2017b). The attitude control of the BDS-2 satellites is accomplished by an assembly of Earth and Sun sensors and four reaction wheels. BDS-2 satellites have a specified lifetime of eight years.


(a) BDS-2 MEO/IGSO satellite   **(b)** BDS-2 GEO satellite
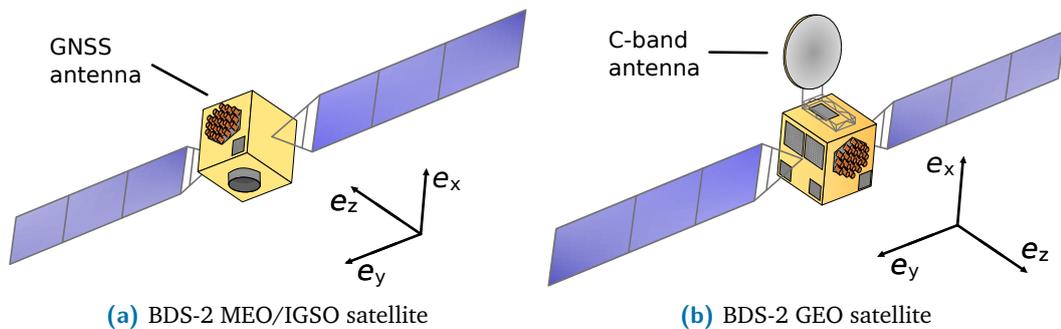
Fig. 2.4: BDS-2 satellites (based on Montenbruck et al., 2015).

All BDS-2 satellites carry the RNSS navigation payload, including the time and frequency subsystem, the navigation processor and a signal generation unit (Yang et al., 2017b). The primary clocks used in the BDS-2 satellites are Rubidium atomic frequency standards (RAFS) from Chinese manufacturers, while RAFS from European manufacturers serve as backup units (Zhao et al., 2018). According to Han et al. (2013), the frequency stability at a 1-day sample time is about $2.53 \cdot 10^{-14}$ to $9.38 \cdot 10^{-14}$. Phased-array antennas are used for transmission of the L-band navigation signals on three frequency bands (B1, B2 and B3), and laser retroreflector arrays are mounted to enable satellite laser ranging (SLR) (Yang et al., 2017b).

The GEO satellites are additionally equipped with the RDSS payload. It consists of a C-band antenna and an L/S-band antenna, used for BDS-1-type navigation, short messaging and two-way satellite time and frequency transfer (TWSTF) for time synchronization of the ground stations and data transmission (Han et al., 2011).

BDS-3 satellites

The BDS-3 satellites utilize platforms developed by two different manufacturers. The GEO and IGSO satellites adopt platforms by CAST; the MEO satellite platforms are either manufactured by CAST or the Shanghai Engineering Center for Microsatellites (SECM). In comparison with the CAST MEO satellites, the ones developed by SECM have different geometric configurations. The satellite surface pointing towards the Earth of the SECM platform is elongated, and the satellite is more cuboid than the cubic shape of the CAST satellites (Dilssner et al., 2020). The rectangular shape of the SECM MEO spacecraft is similar to Galileo satellites. The BDS-3 IGSO and GEO satellites are significantly larger and more than twice as heavy as the MEO satellites. Knowledge about the dimension of the satellites is crucial for precise orbit determination, particularly for the modeling of solar radiation pressure (SRP). More information about this topic is provided in Section 4.

BDS-3 has made significant adjustments in terms of the satellite payload. Instead of Sun and Earth sensors, a star camera is employed to determine the satellite's attitude and stabilize its orientation (Zhao et al., 2018). An important innovation of BDS-3 equipment is the inter-satellite link (ISL). As stated in Yang et al. (2017a), the satellites launched since March 2015 carry Ka-band ISL antennas, which can measure clock errors and ranges and transfer information between satellites. The authors conducted a combined orbit determination experiment using both ISL measurements and ranging observations from ground stations and reported substantial improvements in orbit determination accuracy. BDS-3 uses ISL to overcome the shortage of well-distributed ground stations and improve the performance and stability of the global service. The implementation of ISL in precise orbit determination is not part of this study but offers considerable potential for future investigations. More information about ISL and corresponding evaluation results can be found in Yang et al. (2017a) and Yang et al. (2019b).

The primary frequency standard for BDS-3 is based on passive hydrogen masers (PHM) developed by the Shanghai Astronomical Observatory and the Beijing Institute of Radio Metrology and Measurement, and improved RAFS by Chinese manufacturers serve as backup (Zhao et al., 2018). Wu et al. (2018) evaluated the performance of the PHM. They came to the result that the in-orbit frequency stability of the BDS-3 PHM is approximately $6 \cdot 10^{-15}$ at 1-day intervals, which is superior to the BDS-3 RAFS and most of the GPS Block IIF and Galileo onboard clocks. The antenna used for the transmission of the navigation signals broadcasts on six frequency bands. For more information on the different signals used by BeiDou, refer to Section 2.6.

2.5 Attitude modes

Knowledge about the satellite's orientation in space, also known as attitude, is essential for high-precision GNSS data processing. Incorrect modeling of the satellite's attitude leads to measurement correction errors and dynamic force errors. The attitude-related measurement correction errors comprise improper modeling of the phase center offset (PCO) and the phase wind-up effect (Bar-Sever, 1996; Wu et al., 1992). The PCO and its direction-specific deviation, the phase center variation (PCV), define the antenna position relative to the center-of-mass of the satellite in a body-fixed spacecraft coordinate system. The phase wind-up effect is a variation of the measured carrier-phase, which depends on the relative orientation of the transmitter and receiver antenna and the direction of the line of sight. The dynamical force errors imply the incorrect modeling of non-gravitational perturbations that act on the spacecraft. With solar radiation pressure (SRP) being the dominant non-gravitational force, these perturbing accelerations directly depend on the satellite's structure and orientation with respect to the incident radiation (Rodriguez-Solano et al., 2012).

In the following sections the different attitude modes used by BeiDou are presented. The definition of the reference frames and the labeling of the principal axes are in accordance with the International GNSS Service (IGS) conventions as formulated by Montenbruck et al. (2015).

2.5.1 Satellite-fixed reference frames

Body-fixed frame

A body-fixed reference frame is necessary to describe the orientation of a satellite in space. Since orbit information is usually related to the center-of-mass of the satellite, but the navigation signals are transmitted from an antenna at a different location, a reference frame that is tied to the mechanical structure of the spacecraft was defined to specify the PCO and the PCV (Montenbruck et al., 2015). This reference frame is also used to describe the position and alignment of individual surface elements, which is needed for the analytical modeling of the SRP. The uniform definition of the respective spacecraft axes, as defined by the IGS in Montenbruck et al. (2015), are as follows:

- The $+z_{\mathrm{BF,IGS}}$-axis is aligned with the boresight direction of the navigation antenna, which corresponds to the direction of the maximum beam intensity.

- The rotation axis of the solar panels is parallel to the $y_{\mathrm{BF,IGS}}$-axis.

- The $+x_{\text{BF,IGS}}$-axis is pointing towards the sun-lit hemisphere. This alignment ensures that the $+x_{\text{IGS}}$-panel is permanently exposed to the Sun while performing nominal yaw-steering.

- The axes of the body-fixed frame form a right-handed, orthonormal basis.

Local orbital frame

The radial (R), cross-track (C) and along-track (A) direction unit vectors

$$
\begin{aligned}
\boldsymbol{e}_{\text{R}} &= \frac{\boldsymbol{r}}{|\boldsymbol{r}|} \\
\boldsymbol{e}_{\text{C}} &= \frac{\boldsymbol{r} \times \boldsymbol{v}}{|\boldsymbol{r} \times \boldsymbol{v}|} \\
\boldsymbol{e}_{\text{A}} &= \boldsymbol{e}_{\text{C}} \times \boldsymbol{e}_{\text{R}}
\end{aligned}
\tag{2.1}
$$

define the local orbital frame, where $\boldsymbol{r}$ is the geocentric position vector of the satellite and $\boldsymbol{v}$ is the velocity vector of the geocentric satellite motion. With a series of three elementary rotations by the angles roll ϕ, pitch ϑ and yaw ψ

$$
\boldsymbol{x}_{\text{BF}} = \mathbf{R}_x(\phi) \cdot \mathbf{R}_y(\vartheta) \cdot \mathbf{R}_z(\psi) \cdot \boldsymbol{x}_{\text{RCA}}
\tag{2.2}
$$

the body-fixed frame can be transformed into the local orbital frame. Since the navigation antenna of GNSS satellites is pointing to the geocenter and therefore the $+z_{\text{BF,IGS}}$-axis and the $-\boldsymbol{e}_{\text{R}}$-axis coincide, the roll ϕ and pitch ϑ angles vanish. The yaw angle ψ, which describes the angle between the $+\boldsymbol{e}_{\text{A}}$-axis and the $+x_{\text{BF,IGS}}$-axis can fully determine the attitude of the satellite (Montenbruck et al., 2015).
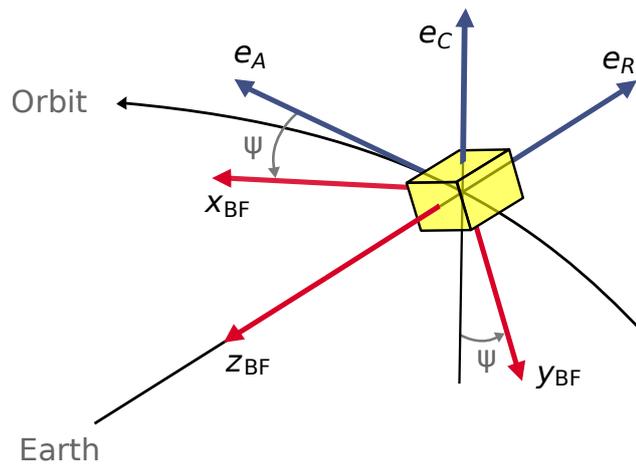

Fig. 2.5: Definition of the yaw-angle (based on Montenbruck et al., 2015).

2.5.2 Yaw-steering mode

The nominal attitude of a GNSS satellite is determined by satisfying two requirements: The navigation antenna needs to point towards the center of the Earth, and the solar array surface needs to be orientated towards the Sun. In order to meet these two conditions, the satellite has to constantly yaw about the Earth-pointing z-axis to keep the y-axis along the solar panel perpendicular to the Sun direction (Bar-Sever, 1996). The positive x-axis points to the same hemisphere as the Sun and completes the orthogonal, right-handed coordinate frame. This concept is known as the nominal yaw-steering (YS) mode. The three unit vectors

$$
\begin{aligned}
\boldsymbol{e}_{z,\mathrm{YS}} &= -\frac{\boldsymbol{r}}{|\boldsymbol{r}|} \\
\boldsymbol{e}_{y,\mathrm{YS}} &= \frac{\boldsymbol{e}_{\mathrm{D}} \times \boldsymbol{r}}{|\boldsymbol{e}_{\mathrm{D}} \times \boldsymbol{r}|} \\
\boldsymbol{e}_{x,\mathrm{YS}} &= \boldsymbol{e}_{y,\mathrm{YS}} \times \boldsymbol{e}_{z,\mathrm{YS}}
\end{aligned}
\tag{2.3}
$$

define the YS frame. Since $\boldsymbol{r}$ is the geocentric position vector of the satellite, $\boldsymbol{e}_{z,\mathrm{YS}}$ is a unit vector pointing to the center of the Earth. The unit vector

$$
\boldsymbol{e}_{\mathrm{D}} = \frac{\boldsymbol{r}_{\mathrm{S}} - \boldsymbol{r}}{|\boldsymbol{r}_{\mathrm{S}} - \boldsymbol{r}|},
\tag{2.4}
$$

where $\boldsymbol{r}_{\mathrm{S}}$ is the geocentric position vector of the Sun, is pointing from the satellite to the Sun. $\boldsymbol{e}_{y,\mathrm{YS}}$ is perpendicular to the Sun and nadir direction and the positive direction of $\boldsymbol{e}_{x,\mathrm{YS}}$ is pointing towards the sun-lit hemisphere. The body-fixed frame of a satellite moving in nominal YS mode and the YS frame are aligned (Montenbruck et al., 2015). The nominal yaw angle and the nominal yaw angle rate, as stated in Bar-Sever (1996), are given by

$$
\begin{aligned}
\psi &= \mathrm{atan2}(-\tan\beta, \sin\mu) \\
\dot{\psi} &= \frac{\dot{\mu}\tan\beta\cos\mu}{\sin^2\mu + \tan^2\beta},
\end{aligned}
\tag{2.5}
$$

where β is the acute angle between the position vector of the Sun $\boldsymbol{r}_{\mathrm{S}}$ and the orbit plane. μ is the orbit angle measured between the position vector of the satellite $\boldsymbol{r}$ and the midnight point of the orbit. The midnight point denotes the point farthest away from the Sun in the orbital plane. The point closest to the Sun in the orbital plane is called the noon point. The average orbit angular velocity $\dot{\mu}$ as stated in Wang et al. (2018b), is given by

$$
\begin{aligned}
\dot{\mu} &= \sqrt{\frac{\mathrm{GM}}{a^3}} \\
a &= \frac{r}{2 - \frac{rv}{\mathrm{GM}}},
\end{aligned}
\tag{2.6}
$$

where GM is the Earth's gravitational constant and r and v are the scalar quantities of the geocentric position vector r and the velocity vector v, respectively. Equation (2.5) becomes singular at the intersections of the geocentric position vector of the Sun with the satellite's orbit. The yaw angle ψ is undetermined, and the yaw angle rate $\dot{\psi}$ is unbounded at these points.
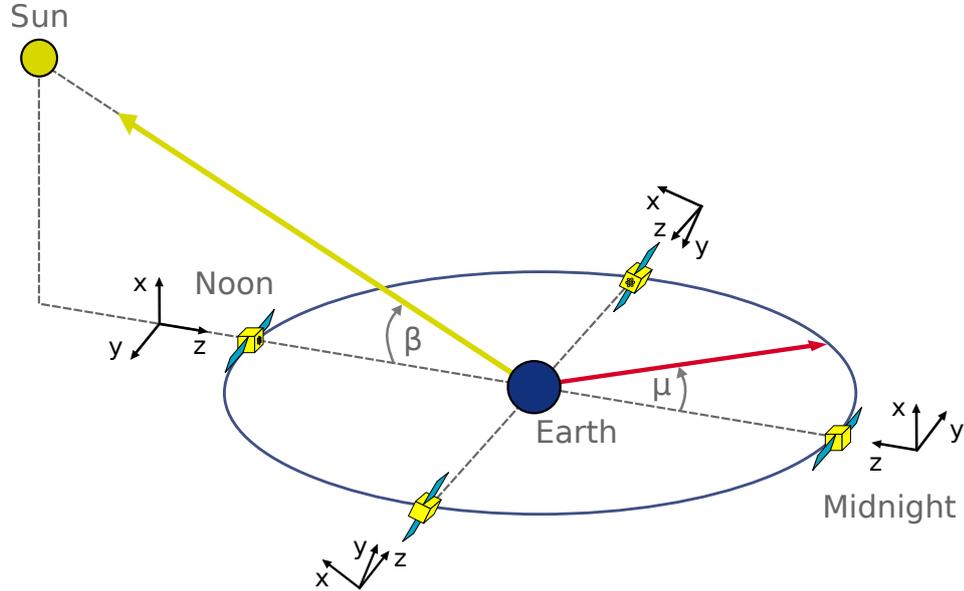

Fig. 2.6: Illustration of satellites moving in yaw-steering (YS) mode (based on Montenbruck et al., 2015).

2.5.3 Orbit-normal mode

In orbit-normal (ON) mode, the orientation of the satellite axes is aligned with the local orbital frame (Montenbruck et al., 2015). The z_{ON}-axis points towards the Earth's center; the y_{ON}-axis is perpendicular to the orbit plane and the x_{ON}-axis points in the direction of the velocity vector of the satellite v. The axes form an orthogonal, right-handed coordinate frame. The unit vectors of the orbit-normal frame

$$
\begin{aligned}
e_{z,ON} &= -\frac{r}{|r|} \\
e_{y,ON} &= -\frac{r \times v}{|r \times v|} \\
e_{x,ON} &= e_{y,ON} \times e_{z,ON}
\end{aligned}
\tag{2.7}
$$

coincide with the ones from the local orbital frame (see Equation (2.1)), but the y_{ON}- and the z_{ON}-axis point to the transverse direction. Since x_{ON} points in the direction of the satellite motion, it yields a yaw angle of zero. In ON mode, the surface area of the solar panels is not perpendicular to the Sun direction, except for $\beta = 0°$. The power generation of the solar panels in ON mode is elevation-dependent and decreases by the factor of $\cos \beta$ compared to the YS mode (Prange et al., 2020).

The solar panels perform a 360° rotation throughout one orbit revolution with respect to the satellite bus (Montenbruck et al., 2015). Hereby, the angle between the solar array surface normal and $e_{z,\mathrm{ON}}$ coincides with the orbit angle μ.
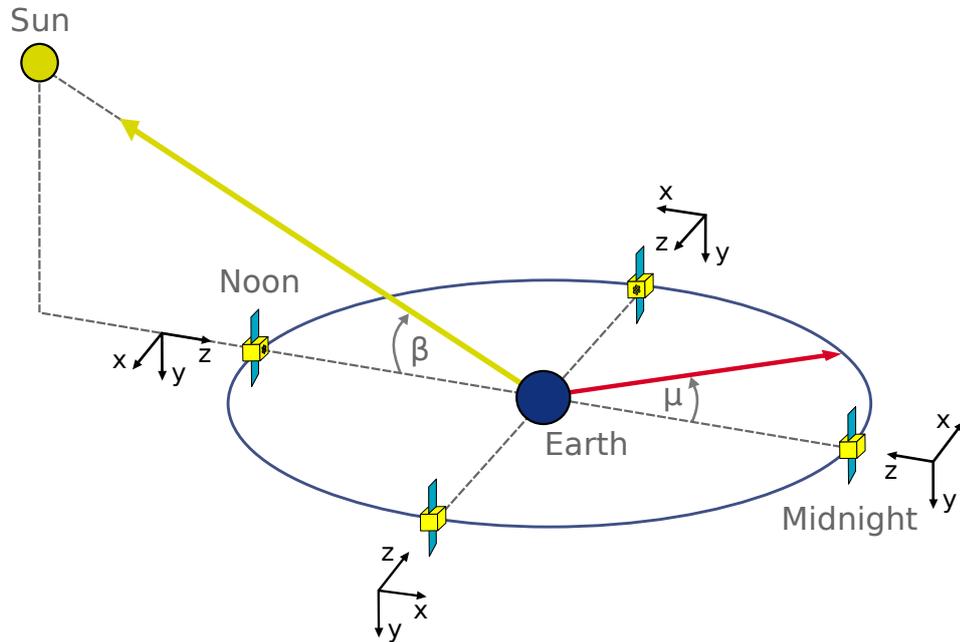

Fig. 2.7: Illustration of satellites moving in orbit-normal (ON) mode (based on Montenbruck et al., 2015).

2.5.4 Behaviour of BeiDou satellites during eclipse season

As already mentioned, the two constraints, namely that the navigation antenna has to point towards the Earth' center and that the solar panel normal has to point in the direction of the Sun, are met when the satellite is constantly yawing along the z-axis. However, this nominal yaw-steering mode cannot be performed when the Sun is close to the orbital plane. As can be seen from Equation (2.5), the nominal rotation rate of the yaw angle increases as the β angle decreases. When the satellite-Sun and satellite-Earth vectors are collinear, i.e., the β angle is zero, the satellite would theoretically have to rotate instantaneously by 180° at the midnight and noon points of the orbit (Prange et al., 2020). The onboard sensors of the attitude control system are used to monitor the position of the Sun and Earth, and the satellite can be adjusted to the required orientation by the momentum wheels (Wang et al., 2018b). During the midnight and noon crossings, the required yaw rate exceeds the maximum hardware rate, and the attitude control system cannot align the satellite to the nominal orientation. In order to avoid the problem of rapid yaw turns the BeiDou satellites adopt different strategies.

The BDS-2 MEO and IGSO satellites were originally designed to adopt the YS mode but to enter into ON mode when they are in deep eclipse season (Guo et al., 2013). The eclipse season is the period when β falls beneath a certain threshold and the satellite experiences Earth shadow crossings once per revolution. Kouba (2009) stated that assuming a point light source, the eclipse season of a satellite starts when

$$|\beta| < \frac{R_{\mathrm{E}}}{r},\tag{2.8}$$

where R_{E} is the mean radius of the Earth and r is the norm of the geocentric position vector of the satellite. Consequently, MEO and IGSO satellites cross the Earth's shadow when $|\beta|$ approximately falls below 13° and 8.5°, respectively. By changing the attitude mode during this time, the BDS-2 MEO and IGSO satellites avoid the rapid yaw turns during the midnight and noon points. Since the exact attitude control mechanism and the conditions for the switch between the attitude modes are not published, several studies have been carried out to estimate yaw-attitude, based on the reversed kinematic PPP approach (Dai et al., 2015; Wang et al., 2018b; Xia et al., 2019; Zhao et al., 2018). The common conclusion is that the switch is conducted when β is close to $\pm 4°$ and the YS and ON mode show similar orientation. A small difference in orientation is favorable since the attitude control system consumes the lowest energy this way. In this study, the requirements for the switch were set to be:

- The absolute amount of the Sun-elevation angle: $|\beta| < 4°$.

- The difference between the yaw-angles of YS and ON mode: $|\Delta\psi| < 5°$.

The ON mode for BDS-2 MEO and IGSO satellites can last 8 to 15 days (Li et al., 2018b). An empirical solar radiation pressure model for satellites moving in ON mode will be described in Section 4.3.2. Since the orbit accuracy of satellites in ON mode is inferior to those in YS mode, some BDS-2 satellites have already abandoned the ON mode in favor of the continuous yaw-steering (CYS) mode (Xia et al., 2019). More information about the BDS-2 satellites that have changed their attitude mode can be found in Section 5.3.2.

All the BDS-3 MEO and IGSO satellites maintain the CYS mode (Wang et al., 2018b). In this attitude mode, midnight and noon maneuvers have to be performed. Outside a β angle of $\pm 3°$, the satellites are able to maintain the nominal yaw attitude even when they are passing through the Earth's shadow. During the orbit maneuvers, the satellites rotate by 180° at an estimated, variable yaw rate, which can take up to 40 minutes (Wang et al., 2018b). The the actual yaw angle at the midnight and noon points equals $-90°$. This procedure ensures that the deviation between the nominal and the actual yaw angles is as small as possible. The CYS attitude control model

used in this study is based on the model for the Galileo FOC satellites published by the European GNSS Service Centre (2017) with adopted values, estimated by Wang et al. (2018b). The yaw angle in CYS mode can be expressed as

$$
\psi(\mu) = 90° \cdot \text{sign}(1, \psi(\mu_{\text{s}})
$$
$$
+ [\psi(\mu_{\text{s}}) - 90° \cdot \text{sign}(1, \psi(\mu_{\text{s}}))] \cdot \cos\left(\frac{2\pi}{t_{\text{max}}} \cdot \frac{\mu - \mu_{\text{s}}}{\dot{\mu}}\right),
\tag{2.9}
$$

where μ_{s} is the orbit angle at the start of the yaw maneuver, and $\psi(\mu_{\text{s}})$ is the associated nominal yaw angle. The constant t_{max} depicts the maximum yaw maneuver time. In this study, the requirements to be met were set to be:

- The absolute amount of the Sun-elevation angle: $|\beta| < 3°$.

- The colinearity angle at the start of the yaw maneuver: $\epsilon = 6°$ for the midnight turn; and $\epsilon = 174°$ for the noon turn.

The colinearity angle ϵ can be determined by

$$
\epsilon = \arccos\left(|\boldsymbol{r}| \cdot |\boldsymbol{n} \times (\boldsymbol{n} \times \boldsymbol{r}_{\text{S}})|\right)
\tag{2.10}
$$

where $\boldsymbol{n}$ is the orbit normal vector. The corresponding maximum yaw maneuver time was $3090\,\text{s}$ and $5740\,\text{s}$ for MEO and IGSO satellites, respectively. Figure 2.8 compares the yaw angles from the nominal YS mode and the CYS mode conducted on October 13, 2020.
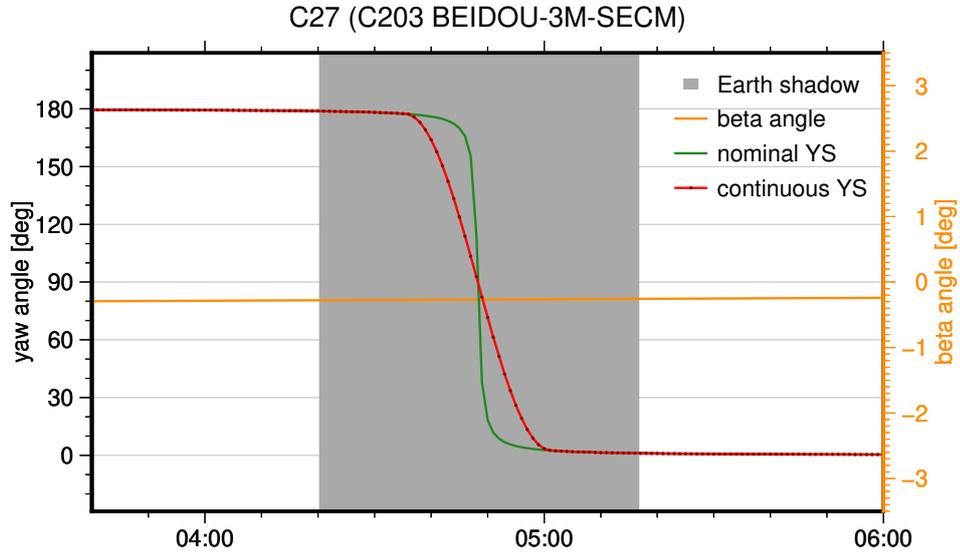

Fig. 2.8: Midnight maneuver of the BDS-3 MEO satellite C27 on October 13, 2020.

The GEO satellites of BDS-2 and BDS-3 maintain the ON mode at all times, so they constantly adapt a yaw angle of zero and do not have to perform any midnight or noon maneuvers (Prange et al., 2020).

2.6 Signals

BeiDou transmits navigation signals on multiple frequencies. Signals of the BDS-2 satellites are modulated on the B1, B2 and B3 frequency bands. BDS-3 satellites are broadcasting on the frequency bands B1C, B1A, B2a, B2b, B2(B2a+B2b) and B3A. BDS-3 is backward-compatible with BDS-2 and additionally continues to provide signals on B1 and B3. The different BeiDou signals are displayed in Table 2.3.

Tab. 2.3: BeiDou signals in Receiver Independent Exchange Format (RINEX) as stated in Romero (2020).

Frequency	System	Code	Phase	Service
B1 (1561.098)	BDS-2 BDS-3	C2I	L2I	Open
		C2Q	L2Q	Authorized
		C2X	L2X	Authorized
B1C (1575.420)	BDS-3	C1D	L1D	Open
		C1P	L1P	Open
		C1X	L1X	Open
B1A (1575.420)	BDS-3	C1S	L1S	Authorized
		C1L	L1L	Authorized
		C1Z	L1Z	Authorized
B2a (1176.450)	BDS-3	C5D	L5D	Open
		C5P	L5P	Open
		C5X	L5X	Open
B2 (1207.140)	BDS-2	C7I	L7I	Open
		C7Q	L7Q	Authorized
		C7X	L7X	Authorized
B2b (1207.140)	BDS-3	C7D	L7D	Open
		C7P	L7P	Open
		C7Z	L7Z	Open
B2(B2a+B2b) (1191.795)	BDS-3	C8D	L8D	Open
		C8P	L8P	Open
		C8X	L8X	Open
B3 (1268.520)	BDS-2 BDS-3	C6I	L6I	Open
		C6Q	L6Q	Authorized
		C6X	L6X	Authorized
B3A (1268.520)	BDS-3	C6D	L6D	Authorized
		C6P	L6P	Authorized
		C6Z	L6Z	Authorized

BeiDou offers two kinds of services: the open service and the authorized service. All open service signal specifications have officially been released in the form of Interface Control Documents by the China Satellite Navigation Office via its website (`http://en.beidou.gov.cn/SYSTEMS/ICD/`).

2.6.1 Signal characteristics

Each signal on the BDS-2 frequency bands B1, B2 and B3 is the sum of the channels I and Q, which are in phase quadrature of each other. The in-phase components I of the frequency bands are part of the open service, whereas the quadrature components Q are part of the authorized service. The signal is composed of the ranging code and the navigation message modulated on the carrier frequency. Binary Phase Shift Keying (BPSK) is used for the modulation of the open service signals of B1 and B3 (China Satellite Navigation Office, 2018b, 2019b), the signal of B2 is modulated by Quadrature Phase Shift Keying (QPSK) (China Satellite Navigation Office, 2016). The ranging code is a truncated Gold code. The transmitted signals of the BDS-2 frequency bands are Right-Handed Circularly Polarized (RHCP), and the method of signal multiplexing is Code Division Multiple Access (CDMA). A minimum received power level of -163 dBW is specified for all the BDS-2 signals.

The signals of the BDS-3 frequency bands consist of a data and a pilot component, except for B2b, which has an I and Q component (China Satellite Navigation Office, 2017a,b, 2020a). The data component is generated by modulation of the navigation message and the ranging code on the carrier frequency, whereas the pilot component only contains the ranging code. All BDS-3 signals are RHCP. The modulation process employed by the BDS-3 signals is either BPSK, Binary Offset Carrier (BOC) or Quadrature multiplexed Binary Offset Carrier (QMBOC). The specific signal characteristics of the open service BeiDou signals are represented in Table 2.4.

BeiDou employs different types of navigation messages based on their data rate and structure (China Satellite Navigation Office, 2016). The D1 navigation message contains the basic navigation information comprising fundamental navigation information of the broadcasting satellite, Almanac data and time offsets from other systems. The D2 navigation message additionally contains augmentation service information. A secondary Neumann-Hoffman code is modulated on the ranging code of signals containing the D1 navigation message. The D1 navigation message is part of the BDS-2 signals broadcasted by the MEO and IGSO satellites, whereas the D2 navigation message is transmitted by the BDS-2 signals of the GEO satellites. The signals of the GEO satellites are designed for high data rates, while the MEO and IGSO signals show improved properties at the expense of a lower data rate (Yang et al., 2017b). However, the data components of the BDS-3 signals B1C, B2a and B2b have different navigation messages modulated on their carriers (China Satellite Navigation Office, 2017a,b, 2020a). The B1C signal navigation message is called B-CNAV1, B-CNAV2 is the corresponding navigation message of B2a and B2b contains the B-CNAV3 navigations message. A distinction in signal structure for different satellite types of the same GNSS constellation is unique to BeiDou.

Tab. 2.4: BeiDou open service signal characteristics. The specific values shown in this table are taken from China Satellite Navigation Office (2016, 2017a,b, 2018b, 2019b, 2020a).

Frequency	Signal	Modulation	Chip rate [Mcps]	Bandwidth [MHz]	Power[a] [dBW]
B1	C2I	BPSK(2)	2.046	4.092	−163
	C2Q	n/a	n/a	n/a	n/a
B1C	C1D	BOC(1,1)	1.023	32.736	−159
	C1P	QMBOC[b]			−161
B2a	C5D	BPSK(10)	10.23	20.46	−156
	C5P	BPSK(10)			−158
B2	C7I	QPSK(2)	2.046	20.46	−163
	C7Q	n/a	n/a	n/a	n/a
B2b	C7D	BPSK(10)	10.23	20.46	−160
	C7P	n/a	n/a	n/a	−162
B3	C6I	BPSK(10)	10.23	20.46	−163
	C6Q	n/a	n/a	n/a	n/a

[a]For signals, which contain a data and a pilot component, the minimum received power level on ground is the combined power of both components; the first value in the corresponding cell is the power received from MEO satellites and the value below belongs to the IGSO satellites.
[b]The exact modulation of C1P is QMBOC(6,1,4/33).

2.6.2 Signal quality

The accuracy of the open service signals can be evaluated by the Signal in Space Ranging Error (SISRE). It represents the statistical value of the differences between the measured signal in space ranges and the pseudo-range values obtained from the navigation message parameters, excluding the user receiver clock offsets or measurement errors (China Satellite Navigation Office, 2018a). Ionospheric delay errors, tropospheric delay errors, multipath, receiver noise, etc., are not considered in the SISRE. The I-components of the B1 and B3 frequency bands have a SISRE of less than 1 m. The SISRE of the B1C and B2a signals is less than 0.6 m.

The frequencies of the BeiDou signals partly overlap with the signals of other global (GPS, Galileo) and regional (Quasi-Zenith Satellite System (QZSS), Indian Regional Navigation Satellite System (IRNSS)) navigation satellite systems. This allows for tightly combined observations and enhances the compatibility and interoperability among the systems. Table 2.5 lists the frequencies and the overlapping signals of the respective systems.

Tab. 2.5: BeiDou open service signals overlapping with other navigation systems.

Frequency	GPS	Galileo	BDS-2	BDS-3	QZSS	IRNSS
1561.098			B1			
1575.420	L1	E1		B1C	L1	
1176.450	L5	E5a		B2a	L5	L5
1207.140		E5b	B2	B2b		
1191.795		E5		B2(B2a+B2b)		
1268.520			B3			
1278.750		E6			L6	
1227.600	L2					

The overall signal quality of BDS-3 signals is expected to be better than that of BDS-2 since a more stable time and frequency standard is used (see Section 2.4.2). Numerous studies have been carried out to assess the signal quality of BDS-2 signals, yet fewer publications have been published about the performance of BDS-3. Zhang et al. (2017) and Yang et al. (2018) have evaluated the navigation signals and the performance of BDS-3 based on data of the BDS-3 demonstration system. Zhang et al. (2019) assessed the signal quality using the primary constellation of BDS-3. The conclusions of their studies are in agreement with each other, and their main findings are listed below:

- The observational quality of the BDS-3 signals is comparable to the GPS L1/L2/L5 and Galileo E1/E5a/E5b signals.

- The Carrier-to-Noise-density ratio of BDS-3 signals is slightly larger than those of BDS-2 and comparable to the signals of GPS and Galileo.

- The code noise of BDS-3 is smaller than that of BDS-2; the phase noise level of all systems is quite similar.

- Systematic biases in multipath combinations have been identified in BDS-2. These elevation-dependent biases are not obvious for the BDS-3 signals.

- Apparent systematic variations of triple-frequency carrier phase combinations, as observed in BDS-2, no longer exist in BDS-3.

- The incorporation of BDS-3 signals improves the ambiguity resolution performance with respect to positioning with BDS-2 only.

2.7 IGS products and analysis centers

The International GNSS Service (IGS) is an international federation of 350 organizations, involving self-funding agencies, universities and research institutions located in more than 100 countries (Johnston et al., 2017). The IGS aims to provide the highest-quality GNSS data and products in order to support the terrestrial reference frame, Earth observation and research, PNT and other applications for free and openly accessible. Officially established in 1994 as a service of the International Association of Geodesy (IAG), it supports scientific research primarily based on GPS, while GLONASS was integrated in 2005 (Dow et al., 2009). With the advent of new global (BeiDou, Galileo) and regional (QZSS, IRNSS) navigation satellite systems, the IGS has initiated the Multi-GNSS Experiment (MGEX) to incorporate the new constellations and provide high-quality data products (Montenbruck et al., 2014). The IGS collects, archives and distributes GNSS observation data sets, whereas a global network of over 500 permanent tracking stations serves as the backbone of their services. As of November 2021, the IGS states that 294 stations can track BeiDou signals (International GNSS Service, 2021e).

Official core products such as precise satellite orbits, satellite and station clocks, Earth orientation parameters as well as station coordinates are formed from a properly weighted combination of independent results produced by a number of analysis centers (International GNSS Service, 2021a). The institutions declared as official IGS analysis centers are listed in Table 2.6.

Tab. 2.6: Official analysis centers as stated on the IGS website (International GNSS Service, 2021b).

Institution	Abbreviation	Country
Natural Resources Canada	EMR	Canada
Wuhan University	WHU	China
Geodetic Observatory Pecny	GOP	Czech Republic
Space geodesy team of the CNES	GRGS	France
European Space Agency/ESOC	ESA/ESOC	Germany
GeoForschungsZentrum	GFZ	Germany
Center for Orbit Determination in Europe	CODE	Switzerland
Jet Propulsion Laboratory	JPL	USA
Massachusetts Institute of Technology	MIT	USA
NOAA/National Geodetic Survey	NGS	USA
Sripps Institution of Oceanography	SIO	USA
U.S. Naval Observatory	USNO	USA

The Center for Orbit Determination in Europe (CODE), the European Space Agency (ESA), the GeoForschungsZentrum (GFZ) in Potsdam and Wuhan University (WHU) implement the precise orbit determination of BDS-2 and BDS-3 satellites in their routines for the MGEX products and were therefore used for validation of the results of this study (see Section 5.3.3).

GNSS orbit determination 3

In this chapter, the processing strategy for precise orbit determination of GNSS satellites applied at Graz University of Technology (TUG) is presented. The underlying physical effects of orbit modeling and the mathematical fundamentals to fit the modeled orbits to GNSS observations are described in the following sections. The approach can be divided into two major parts: In the preprocessing step, orbit modeling is performed by numerical integration of the equation of motion (see Section 3.2 and 3.3). Subsequently, the modeled orbits are fitted to approximate orbits by estimating initial values for the position and velocity of the satellite, parameters of the applied solar radiation pressure (SRP) model and additional empirical parameters using a standard variational equation method (see Section 3.4 and 3.5). The actual processing is based on the linearization of the GNSS observation equations using variational equations. In this step, the initial parameters are updated, and parameters regarding systematic influences are estimated in an iterative least-squares adjustment. The processing is implemented using the raw observation approach, which is described in Section 3.6. The analyses presented in this thesis have been conducted using the Gravity Recovery Object Oriented Programming System (GROOPS) software toolkit. Some general information about GROOPS can be found in Section 3.7.

3.1 Methods of precise orbit determination

When determining precise satellite orbits, three different methods can be distinguished: kinematic, dynamic and reduced dynamic orbit determination. Kinematic orbit determination is based entirely on epoch-wise GNSS observations and is independent of satellite dynamics and orbit characteristics (Švehla and Rothacher, 2005). This direct approach of estimating the satellite positions is purely geometric and does not make use of any dynamical force models. Kinematic orbit determination is widely used in gravity field research (e.g. Zehentner and Mayer-Gürr, 2015) because no a priori information about the gravity field is needed. By discarding information about the spacecraft motion, the sensitivity to force model errors vanishes, and the process of determining a solution becomes less complex. However, kinematic orbits highly correlate with erroneous measurements, bad viewing geometry and outages (Montenbruck et al., 2005), which restricts their practical use in the precise orbit determination of GNSS satellites.

Dynamic orbit determination is based on the numerical integration of the perturbed equation of motion, which requires additional models of the forces acting on the satellite. GNSS measurements are used to estimate the initial position and velocity of the satellite in the least-squares adjustment. Hereby, the dynamical models constrain the position and velocity estimates, which reduces the sensitivity to measurement errors or a poor viewing geometry (Montenbruck, 2017). Dynamic modeling of the trajectory also allows for bridging possible data gaps, yielding a robust and continuous orbit. However, any mismodeling of the forces acting on the satellite results in systematic errors in the solution (Wu et al., 1991). The quality of the force models used is therefore crucial for the precision of the obtained orbits.

In order to overcome deficiencies in dynamic orbit determination due to the inaccuracy of the force models, the reduced dynamic orbit determination approach has been developed (Yunck et al., 1990). Hereby, additional empirical parameters are estimated in the least-squares adjustment to reduce the residuals of the modeled orbit when it is fitted to GNSS observations. The advantage of reduced dynamic orbits is that the accuracy of the GNSS measurements can be exploited better, whereas the robustness of dynamical orbits is being maintained (Montenbruck et al., 2005). The disadvantage of this method is that these empirical parameters have no physical meaning. Reduced dynamic orbit determination is applied by many analysis centers of the IGS (e.g., Guo et al., 2016; Prange et al., 2017) and it is the approach employed for the analyses conducted within the scope of this thesis.

3.2 Orbit modeling

The Keplerian motion describes the movement of two point-masses relative to each other, based solely on their mutual gravitational attraction. In this special case, which is also known as the two-body problem, Kepler's laws are rigorously valid. The motion is defined by the homogeneous differential equation of second order

$$\ddot{\boldsymbol{r}} + \frac{G(m_1 + m_2)}{r^2} \frac{\boldsymbol{r}}{r} = 0, \tag{3.1}$$

where $\boldsymbol{r}$ is the relative position vector, $r = \|\boldsymbol{r}\|$ is the distance between the related point masses m_1 and m_2, $\ddot{\boldsymbol{r}}$ is the relative acceleration vector and G is the universal constant of gravity (Hugentobler and Montenbruck, 2017). The orbits obtained from Equation (3.1) are elliptic, and their shape does not change with time. However, in the case of precise orbit determination of artificial satellites, additional factors must be taken into account to achieve a more realistic representation of satellite motion:

- The Earth cannot be considered a point mass but has a complex, inhomogeneous mass distribution, which is constantly changing due to Earth and ocean tides and global mass variations.

- The gravitational attraction of third bodies, particularly the Sun and the Moon, impact the motion of the satellite.

- Relativistic effects have to be considered.

- Direct and indirect solar radiation pressure as well as the thrust caused by the GNSS antenna of the satellite act as perturbing forces.

- The mass of the satellite is negligible in comparison to the magnitude of Earth's mass.

Considering these effects, Equation (3.1) may be reformulated to

$$\ddot{\boldsymbol{r}} = -\frac{GM}{r^2}\frac{\boldsymbol{r}}{r} + \boldsymbol{a}(t, \boldsymbol{r}, \dot{\boldsymbol{r}}, p_1, ..., p_n) = \boldsymbol{F}(t, \boldsymbol{r}, ...), \tag{3.2}$$

where GM is the product of the gravitational constant and the mass of the Earth and the acceleration vector $\boldsymbol{a}$ contains all perturbing forces acting on the satellite. $\boldsymbol{a}$ depends on the time t, the position $\boldsymbol{r}$ and velocity $\dot{\boldsymbol{r}}$ of the satellite and various parameters $p_1, ..., p_n$, which determine the applied force models (Montenbruck and Gill, 2000). The orientation and shape of a satellite's orbit are no longer stable in the presence of perturbing forces but vary with time. Equation (3.2) represents a simplified form of the perturbed equation of motion of a satellite orbiting the Earth in the inertial frame. The perturbed equation of motion in its entirety is so complex that efficient yet accurate solutions can only be achieved by numerical methods (Beutler, 2005a).

In order to obtain a particular solution of a differential equation, initial values at one specific position have to be defined. Since the equation of motion is a three-dimensional second-order differential equation, six constants of integration are required. In the case of satellite orbit determination, the initial position at epoch t_0 and its first derivative with respect to time, the initial velocity, is used. A first-order differential equation

$$\dot{\boldsymbol{y}} = \boldsymbol{f}(t, \boldsymbol{y}, \boldsymbol{p}) = \begin{pmatrix} \dot{\boldsymbol{r}} \\ \boldsymbol{F}(t, \boldsymbol{r}, ...) \end{pmatrix} \tag{3.3}$$

can be obtained, where $\boldsymbol{y} = \begin{pmatrix} \boldsymbol{r} & \dot{\boldsymbol{r}} \end{pmatrix}^T$ denotes the state vector and $\boldsymbol{F}(t, \boldsymbol{r}, ...)$ represents the perturbed equation of motion. Assuming all of the additional parameters

$p_1, ..., p_n$ are known, a satellite orbit can be uniquely determined by numerical integration starting from the initial state vector $\boldsymbol{y}(t_0)$. A large number of methods have been developed for the solution of differential equations, and several of them can be applied to satellite orbit determination. Montenbruck and Gill (2000) as well as Beutler (2005a) list some of the most important methods and assess their utility in the computation of satellite orbits. In the analysis conducted within the scope of this thesis, the forces are integrated twice using a moving polynomial method.

3.3 Force modeling

The perturbing accelerations acting on a satellite can be classified into conservative and non-conservative forces. Conservative forces perturb the motion of the satellite in the form of gravitational accelerations, which act on the center of mass of the satellite. Non-conservative forces do not act on the center of mass but on the surfaces of the satellite. Solar radiation pressure and Earth radiation pressure are induced by the interaction of radiation with the surface of the satellite body (Rodriguez-Solano, 2014). Consequently, information about the dimensions and the mass of the satellite, its orientation in space and the radiation (whether it is from the Sun, the Earth or generated by the satellite itself) is necessary to model non-conservative forces. The orders of magnitude of the different perturbing forces that have to be considered in the precise orbit determination of GNSS satellites are shown in Figure 3.1.

Conservative forces account for the largest perturbations of the satellite motion, yet models of gravitational accelerations are well established and of high quality. Non-conservative forces have smaller effects on GNSS satellite orbits in comparison to the main conservative forces, but they are more difficult to model. Solar radiation pressure (SRP) is the dominant error source in precise orbit determination (Rodriguez-Solano, 2014), which indicates that the correct modeling of non-conservative forces is crucial for the achievable orbit accuracy.

A comprehensive description of the forces involved in precise orbit determination can be found in Beutler (2005b) and Hugentobler and Montenbruck (2017). Conservative forces are thoroughly discussed in Petit and Luzum (2010). A summary of the conservative forces is given in the following section. Non-conservative forces are described in Section 3.3.2. The modeling of SRP is one of the main objectives of this thesis and is extensively discussed in Chapter 4.
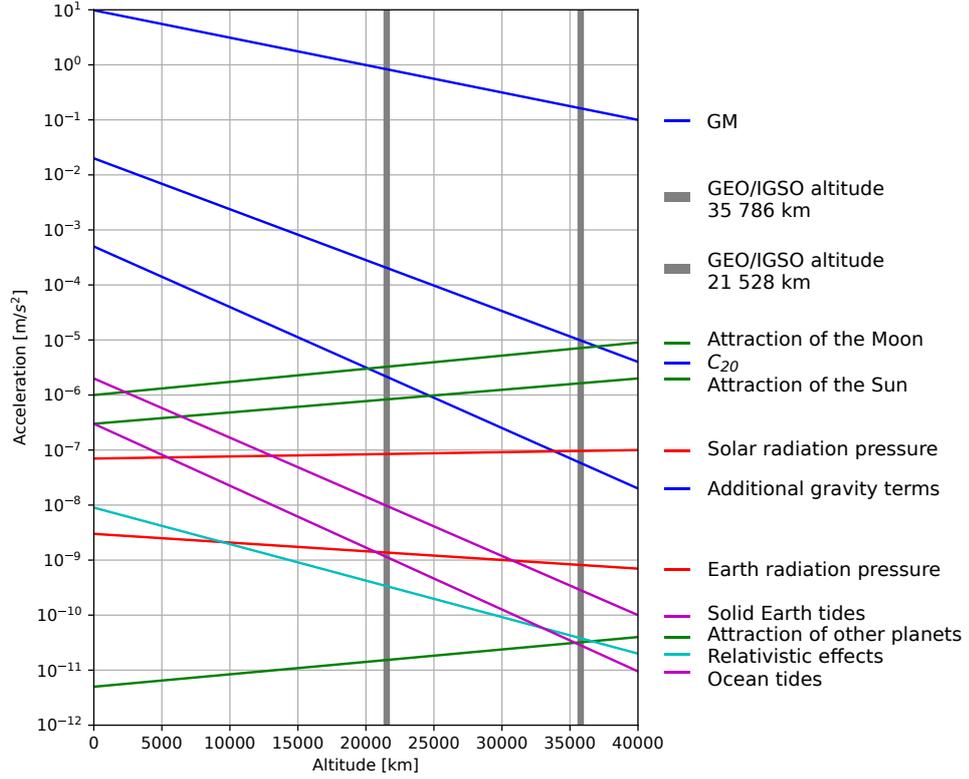
Fig. 3.1: Magnitude of forces acting on a satellite (based on Montenbruck and Gill, 2000 and Strasser, 2016).

3.3.1 Conservative forces

Earth's gravitational field

The perturbing accelerations caused by the inhomogeneous mass distribution inside the Earth can be expressed as the gradient ∇ of the Earth's gravitational potential $V(r, \vartheta, \lambda)$ (Hofmann-Wellenhof and Moritz, 2006)

$$\boldsymbol{a}_{GF} = \nabla V(r, \vartheta, \lambda). \tag{3.4}$$

Outside the Earth, $V(r, \vartheta, \lambda)$ represents a harmonic function and thus can be expanded into a series of spherical harmonics

$$V(r, \vartheta, \lambda) = \frac{GM}{r} \sum_{n=0}^{\infty} \left(\frac{R_E}{r}\right)^n \sum_{m=0}^{n} P_{nm}(\cos\vartheta) \left[C_{nm} \cos m\lambda + S_{nm} \sin m\lambda\right], \tag{3.5}$$

where the geocentric distance of the satellite r, the polar distance ϑ and the geocentric longitude λ denote the spherical coordinates in the Earth-fixed reference frame, and R_E is the mean equatorial radius. $P_{nm}(\cos\vartheta)$ are fully normalized associated Legendre functions of the first kind, where the subscripts n and m denote the degree and order of $P_{nm}(\cos\vartheta)$, respectively. The fully normalized Stokes coefficients C_{nm}

and S_{nm} describe the global structure of the gravitational potential field. These coefficients are obtained using data from gravity field recovery missions such as Challenging Minisatellite Payload (CHAMP), Gravity field and steady-state Ocean Circulation Explorer (GOCE), Gravity Recovery And Climate Experiment (GRACE) and GRACE Follow-On, or from a combination of satellite gravity data and additional data sources, such as surface gravimetry and satellite altimetry (Ince et al., 2019). An archive of static and temporal global gravitational models is provided by the International Centre for Global Earth Models (ICGEM) service via its website (`http://icgem.gfz-potsdam.de`).

The coefficient C_{00} is defined as a scaling factor for the value of GM and consequently represents the mass of the Earth (Ince et al., 2019). C_{00} is set to 1 per definition. The coefficients of degree $n = 1$ define the geocenter and vanish, if the origin of the Earth-fixed system coincides with Earth's center of mass. The nonsphericity of the Earth is represented by the coefficients of degree $n \geq 2$, where C_{20} denotes the oblateness and C_{21} and S_{21} are related to the position of the mean rotational pole.

If Equation (3.4) is evaluated for $n = 0$, it corresponds to the acceleration of a spherically symmetric mass distribution, which is equivalent to the acceleration of a point mass (Hugentobler and Montenbruck, 2017). This zero-degree term is the central force of the Keplerian motion. The higher-order terms can be considered as perturbing accelerations since they are significantly smaller. As can be seen from Figure 3.1, C_{20} induces the dominant perturbation for MEO satellites and, besides the attraction of the Moon, also the strongest perturbation for satellites at higher altitudes (e.g., IGSO satellites).

Third-body attractions

The perturbations acting on a satellite caused by the gravitational attraction of other celestial bodies

$$\boldsymbol{a}_{TB} = -GM_i \left(\frac{\boldsymbol{r} - \boldsymbol{r}_i}{\|\boldsymbol{r} - \boldsymbol{r}_i\|^3} + \frac{\boldsymbol{r}_i}{\|\boldsymbol{r}_i\|^3} \right) \tag{3.6}$$

can be modeled by considering the so-called third bodies as point masses. The geocentric position vectors of the satellite and the third body are represented by $\boldsymbol{r}$ and $\boldsymbol{r}_i$, respectively. The mass of the celestial body M_i exerts an acceleration not only on the satellite but also on the Earth. Since the motion of a satellite is described with respect to the Earth's center of mass, the perturbing accelerations acting on the Earth, represented by the second term inside the parentheses in Equation (3.6), have to be taken into account as well. The strongest perturbations by celestial bodies are caused by the Moon and the Sun. Accelerations due to the gravitational attraction

of the planets are considerably smaller, with Venus and Jupiter having the biggest impact (Montenbruck and Gill, 2000). The gravitational forces from celestial bodies perturbing the motion of a satellite are also known as astronomical tides.

Solid Earth tides

The gravitational attractions from Sun and Moon not only have a direct impact on the satellite orbits but also induce tidal deformations of the solid Earth (Hugentobler and Montenbruck, 2017). These time-dependent mass variations result in changes of Earth's gravitational potential $V(r, \vartheta, \lambda)$ and subsequently in perturbations of the satellite's motion. The changes of the gravitational potential caused by the solid Earth tides can be modeled as variations of the Stokes coefficients C_{nm} and S_{nm} (Petit and Luzum, 2010). Closed-form models exist to compute the time variable variations ΔC_{nm} and ΔS_{nm}.

Ocean tides

Besides solid Earth tides, tidal mass variations in the oceans induced by gravitational forces of the Sun and the Moon have to be considered as well. The effects of ocean tides are modeled as periodic variations in the Stokes coefficients C_{nm} and S_{nm} (Petit and Luzum, 2010). However, the computation of the effects of ocean tides on satellite motion is more sophisticated than the effects of solid Earth tides. Global ocean tide models are required, which are usually developed as gridded maps of tide height amplitudes. Both solid Earth tides and ocean tides can be considered indirect effects of the gravitational forces of the Sun and the Moon.

Solid Earth pole tides and ocean pole tides

Pole tides are generated by the centrifugal effect of polar motion, dominated by the 14-month Chandler wobble and annual variations (Petit and Luzum, 2010). Both solid Earth pole tides and ocean pole tides induce a variation in the gravitational potential and can be expressed as changes of the Stokes coefficients. In the case of the solid Earth pole tides, an adjustment of C_{21} and S_{22} depicts the variation and in the case of the ocean pole tides, about 99 % of the variance is represented by a spherical harmonic expansion up to degree $n = 10$.

Non-tidal global mass variations

Global mass variation models, such as the Atmosphere and Ocean De-aliasing Level-1B (AOD1B) product, are used to correct for the non-tidal high-frequency variations

in the atmosphere and the ocean (Dobslaw et al., 2013). These short-term variations include changes in atmospheric pressure, terrestrial water storage variations caused by heavy precipitations events, as well as wind-induced redistribution of oceanic water masses and hence changes in the ocean bottom pressure. With a temporal resolution of 3 hours, the release 06 of the AOD1B product (Dobslaw et al., 2017) is provided as a series of Stokes coefficients up to degree and order 180.

AOD1B is typically used as a time-variable background model for the GRACE gravity field estimation process. The model accounts for gravitational signals on submonthly time scales, which cannot be resolved by a global GRACE gravity field solution due to its temporal resolution of about 30 days. Since the non-tidal high-frequency atmospheric and oceanic mass variations cause small changes in the gravitational potential, global mass variation models are also used in the precise orbit determination of GNSS satellites.

Relativistic effects

According to Petit and Luzum (2010), the relativistic correction to the acceleration of an artificial Earth satellite in the Geocentric Celestial Reference System (GCRS) is defined as

$$
\begin{aligned}
\boldsymbol{a}_{RE} = {}& \frac{GM}{c^2 r^3} \left\{ \left[2(\beta + \gamma) \frac{GM}{r} - \gamma \dot{\boldsymbol{r}} \cdot \dot{\boldsymbol{r}} \right] \boldsymbol{r} + 2(1 + \gamma)(\boldsymbol{r} \cdot \dot{\boldsymbol{r}}) \dot{\boldsymbol{r}} \right\} \\
& + (1 + \gamma) \frac{GM}{c^2 r^3} \left[\frac{3}{r^2} (\boldsymbol{r} \times \dot{\boldsymbol{r}})(\boldsymbol{r} \cdot \boldsymbol{J}) + (\dot{\boldsymbol{r}} \times \boldsymbol{J}) \right] \\
& + \left\{ (1 + 2\gamma) \left[\dot{\boldsymbol{r}}_{\mathrm{SE}} \times \left(\frac{GM_S \boldsymbol{r}_{\mathrm{SE}}}{c^2 r_{\mathrm{SE}}^3} \right) \right] \times \dot{\boldsymbol{r}} \right\},
\end{aligned}
\tag{3.7}
$$

where GM and GM_S are the product of the gravitational constant and the mass of the Earth and the mass of the Sun, respectively. $\boldsymbol{r}$ is the geocentric position vector of the satellite, and $\boldsymbol{r}_{\mathrm{SE}}$ is the position vector of Earth with respect to the Sun. The speed of light is denoted as c, β and γ are the parameterized post-Newtonian parameters, which can be set to 1 in general relativity and $\boldsymbol{J}$ is Earth's angular momentum per unit mass.

3.3.2 Non-conservative forces

Earth radiation pressure

Besides direct solar radiation also indirect solar radiation, named Earth radiation, perturbs the motion of the satellite. Earth radiation is composed of two parts (Montenbruck and Gill, 2000): the shortwave optical radiation, reflected from

Earth's surface (Earth albedo); and the longwave infrared radiation emitted by the Earth (thermal re-radiation). A widely used model, proposed by Rodriguez-Solano (2009), decomposes the Earth into surface elements and determines the irradiance received by the satellite based on reflectivity and emissivity coefficients for each of these surface elements. The model is based on a box-wing model of the satellite and applied coefficients provided by the Clouds and the Earth's Radiant Energy System (CERES) project from the National Aeronautics and Space Administration (NASA).

Antenna thrust

The power emitted from the antenna along its boresight while transmitting signals towards the Earth causes an equal reactive force in the opposite direction (Ziebart et al., 2004). The antenna thrust induces a radial acceleration

$$\boldsymbol{a}_{AT} = -\frac{P}{Mc}\boldsymbol{e}_z, \tag{3.8}$$

where P denotes the antenna transmit power, c the speed of light, M the mass of the satellite and $\boldsymbol{e}_Z$ the unit vector of the antenna boresight in Earth direction.

3.4 Empirical parameters

As mentioned in Chapter 3.1, the quality of dynamic orbits highly relies on the applied force models. Inaccuracies of the models deteriorate the precision of the orbits. SRP parameters are estimated empirically in order to model the perturbing accelerations without depending on a priori satellite metadata (see Chapter 4.3). However, in the case of reduced dynamic orbit determination, additional empirical parameters are estimated when the dynamic orbit is fitted to GNSS observations to overcome force model imperfections. Usually, a priori information is used to assign constraints and weighting to those parameters (Montenbruck et al., 2005). The more parameters are estimated, and the fewer constraints are imposed, the more the dynamics of the orbit are attenuated (Swatschina, 2012).

Due to their a priori stochastic properties, these empirical parameters are also called pseudo-stochastic parameters. A number of parametrization methods are given by Jäggi et al. (2006). The models considered in the analysis conducted within the scope of this thesis are instantaneous velocity changes, also known as pseudo-stochastic pulses, and piecewise constant accelerations in the along-track direction.

3.5 Variational equations

The force models discussed in the previous section are required to describe the perturbed motion of a satellite orbiting the Earth. These models depend on various dynamical parameters $p_1, ..., p_n$. A particular orbit solution can be obtained by numerically integrating the forces, starting from the initial state vector $\boldsymbol{y}(t_0)$. In order to determine an orbit that best fits observations, the partial derivatives of the modeled orbit with respect to the initial state vector

$$\left(\frac{\partial \boldsymbol{y}(t)}{\partial \boldsymbol{y}(t_0)}\right)_{6\times 6} = \boldsymbol{\Phi}(t, t_0), \tag{3.9}$$

known as the state transition matrix, and the partial derivatives with respect to the dynamical parameters

$$\left(\frac{\partial \boldsymbol{y}(t)}{\partial \boldsymbol{p}(t_0)}\right)_{6\times n_p} = \mathbf{S}(t), \tag{3.10}$$

called the parameter sensitivity matrix, are required. Due to the complexity of the perturbed equation of motion, an analytical solution of $\boldsymbol{\Phi}(t, t_0)$ and $\mathbf{S}(t, t_0)$ is no longer possible. Instead, a set of differential equations, known as the variational equations, has to be solved by numerical integration. The following derivation of the variational equations is based on Montenbruck and Gill (2000). A first-order differential equation

$$\dot{\boldsymbol{y}} = \boldsymbol{f}(t, \boldsymbol{y}, \boldsymbol{p}) = \begin{pmatrix} \dot{\boldsymbol{r}} \\ \boldsymbol{F}(t, \boldsymbol{r}, ...) \end{pmatrix} \tag{3.11}$$

is defined for the state vector $\boldsymbol{y}$, where $\boldsymbol{F}(t, \boldsymbol{r}, ...)$ denotes the perturbed equation of motion. By derivating Equation (3.11) with respect to $\boldsymbol{y}(t_0)$

$$\frac{\partial \dot{\boldsymbol{y}}(t)}{\partial \boldsymbol{y}(t_0)} = \frac{\partial \boldsymbol{f}(t, \boldsymbol{y}, \boldsymbol{p})}{\partial \boldsymbol{y}(t_0)} = \frac{\partial \boldsymbol{f}(t, \boldsymbol{y}, \boldsymbol{p})}{\partial \boldsymbol{y}(t)} \cdot \frac{\partial \boldsymbol{y}(t)}{\partial \boldsymbol{y}(t_0)} \tag{3.12}$$

and substituting Equation (3.9), the state transition matrix can be determined from the differential equation

$$\dot{\boldsymbol{\Phi}}(t, t_0) = \frac{\partial \boldsymbol{f}(t, \boldsymbol{y}, \boldsymbol{p})}{\partial \boldsymbol{y}(t)} \cdot \boldsymbol{\Phi}(t, t_0) \tag{3.13}$$

starting from the initial value $\boldsymbol{\Phi}(t_0, t_0) = \mathbf{I}_{6\times 6}$. Analogous to the approach described above, the differential equation of the parameter sensitivity matrix

$$\dot{\mathbf{S}}(t) = \frac{\partial \boldsymbol{f}(t, \boldsymbol{y}, \boldsymbol{p})}{\partial \boldsymbol{y}(t)} \cdot \mathbf{S}(t) + \frac{\partial \boldsymbol{f}(t, \boldsymbol{y}, \boldsymbol{p})}{\partial \boldsymbol{p}} \tag{3.14}$$

can be derived. The initial state vector does not depend on the dynamical parameters, thus the initial value $\mathbf{S}(t_0) = \mathbf{0}_{6\times n_p}$.

In order to fit the modeled orbit to GNSS observations, the partial derivatives of the observation equation with respect to $\boldsymbol{y}(t_0)$ and $p_1, ..., p_n$ need to be determined. These partial derivatives can be obtained by

$$\frac{\partial \rho(t)}{\partial \boldsymbol{y}(t_0)} = \frac{\partial \rho(t)}{\partial \boldsymbol{y}(t)} \cdot \frac{\partial \boldsymbol{y}(t)}{\partial \boldsymbol{y}(t_0)} = \frac{\partial \rho(t)}{\partial \boldsymbol{y}(t)} \boldsymbol{\Phi}(t) \tag{3.15}$$

and

$$\frac{\partial \rho(t)}{\partial \boldsymbol{p}} = \frac{\partial \rho(t)}{\partial \boldsymbol{y}(t)} \cdot \frac{\partial \boldsymbol{y}(t)}{\partial \boldsymbol{p}} = \frac{\partial \rho(t)}{\partial \boldsymbol{y}(t)} \mathbf{S}(t), \tag{3.16}$$

where $\rho(t)$ denotes the observation equation of the respective measurement type.

3.6 Raw observation approach

The raw observation approach is a GNSS processing technique, which directly uses all available observations as they are observed by the receivers without forming any linear combinations or observation differences. The approach of using raw observations in GNSS analysis was first proposed by Schönemann et al. (2011) and further elaborated by Schönemann (2013). Zehentner and Mayer-Gürr (2014, 2015) made use of raw GPS observations to determine kinematic satellite positions of low Earth orbit (LEO) satellites, based on the principles of precise point positioning (PPP). The raw observation approach was further developed by Strasser (2016) and Strasser et al. (2019) at Graz University of Technology (TUG) to adopt for precise orbit determination of GNSS satellites. In the course of this thesis, the approach was used to integrate the BeiDou Navigation Satellite System (BeiDou) in the processing of GNSS constellations applied at TUG. This section provides an overview of the raw observation approach and briefly summarizes the influences that have to be addressed. A more profound description of the approach and the processing strategy can be found in Strasser et al. (2019).

The direct use of the observations implicates that the original physical characteristics are preserved, and the information contained in the observations can be fully exploited. It enables the analysis of all individual components of the signal and the conservation of the original measurement accuracy (Strasser et al., 2019). The renunciation of linear combinations and observation differences also greatly facilitates the incorporation of new observables. This is especially beneficial for the processing of BeiDou signals due to the different signal structures used for the specific satellite types. As stated in Yang et al. (2017b), half-cycle intersatellite-type biases can result from inconsistent interpretations of the Neumann-Hoffman code sign (see Chapter 2.6.1), when double-differences of phase observations between GEO and MEO/IGSO BDS-2 satellites are formed and different receiver types are used.

The approach of using all observations as they are observed implies the correction of all known systematic influences in advance by using state-of-the-art models and the determination of all remaining influences as additional parameters in the least-squares adjustment. This leads to a significant increase in the number of parameters to be estimated compared to commonly used methods, such as the ionosphere-free linear combination, which eliminates the first-order ionospheric delay. The raw observation approach is based on setting up observation equations for each measurement individually. The observation equations for code and phase measurements can be written as

$$
\begin{aligned}
R_{r,j}^s - \Delta R_{r,j}^s = {} & \rho_r^s + c\left(\delta_r - \delta^s\right) \\
& + I_{r,j}^{s,(1)} + I_{r,j}^{s,(2)} + I_{r,j}^{(s,3)} + I_{r,j}^{s,\text{EPL}} + I_{r,j}^{s,\Delta\text{TEC}} \\
& + m_\text{w}(e)\Delta D_\text{zw} + m_\text{g}(e)[G_\text{N}\cos\alpha + G_\text{E}\sin\alpha] \\
& + B_{r,j} + B_j^s + \epsilon_{r,j}^s
\end{aligned}
\tag{3.17}
$$

and

$$
\begin{aligned}
\lambda_j\Phi_{r,j}^s - \lambda_j\Delta\Phi_{r,j}^s = {} & \rho_r^s + c\left(\delta_r - \delta^s\right) \\
& + I_{r,j}^{s,(1)} + I_{r,j}^{s,(2)} + I_{r,j}^{(s,3)} + I_{r,j}^{s,\text{EPL}} + I_{r,j}^{s,\Delta\text{TEC}} \\
& + m_\text{w}(e)\Delta D_\text{zw} + m_\text{g}(e)[G_\text{N}\cos\alpha + G_\text{E}\sin\alpha] \\
& + \lambda_j(b_{r,j} + b_j^s + n_j), + \epsilon_{r,j}^s,
\end{aligned}
\tag{3.18}
$$

where the indices denote the dependence on the receiver r, the transmitter (or satellite) s and the signal type j (implying frequency and observation type). The wavelength λ_j of the respective signal is multiplied to the phase observation in order to obtain the measurement in units of meters.

The terms $\Delta R_{r,j}^s$ and $\lambda_j\Delta\Phi_{r,j}^s$ on the left-hand side of the observation equations represent the systematic influences that can be adequately modeled a priori for the code and phase measurements. These code and phase corrections can be expressed as

$$
\begin{aligned}
\Delta R_{r,j}^s = {} & PCO_{r,j} + PCO_j^s + PCV_{r,j} + PCV_j^s \\
& + \Delta\text{rel}_r^s + \Delta\text{stc}_r^s + \Delta\text{station}_r \\
& + m_\text{h}(e)D_\text{zh} + m_\text{w}(e)D_\text{zw}
\end{aligned}
\tag{3.19}
$$

and

$$
\begin{aligned}
\lambda\Delta\Phi_{r,j}^s = {} & PCO_{r,j} + PCO_j^s + PCV_{r,j} + PCV_j^s \\
& + \Delta\text{rel}_r^s + \Delta\text{stc}_r^s + \Delta\text{station}_r + PWU_{r,j}^s \\
& + m_\text{h}(e)D_\text{zh} + m_\text{w}(e)D_\text{zw}.
\end{aligned}
\tag{3.20}
$$

GNSS observations refer to the electrical phase center of the antenna. However, this point is not physically accessible but depends on the antenna type as well as

on the intensity, frequency and direction of the signal (Hofmann-Wellenhof et al., 2007b). The misalignment between a mean phase center and the antenna reference point (ARP) is denoted as antenna phase center offset PCO. The corrections PCO_r and PCO^s specify the offset between the mean antenna phase center and the ARP position of the receiver and the satellite's center of mass, respectively. The specific azimuth- and elevation-dependent deviations of the electrical phase center from the mean phase center are denoted as antenna phase center variations PCV.

Formulas to account for relativistic effects $\Delta\mathrm{rel}_r^s$ and space-time curvature $\Delta\mathrm{stc}_r^s$ caused by Earth's gravitational field can be found in Hofmann-Wellenhof et al. (2007b). Station displacement corrections $\Delta\mathrm{station}_r$ have to be applied to account for tidal and loading effects and the eccentricity between the ARP and the station marker. Phase observations are additionally affected by phase wind-up $PWU_{r,j}^s$, a variation of the measured carrier-phase range depending on the relative orientation of the transmitter and receiver antenna.

The non-dispersive delay induced by the troposphere is commonly divided into a hydrostatic and a wet component (Petit and Luzum, 2010). The majority of the tropospheric delay is constituted by the zenith hydrostatic component D_{zh}, which can be accurately modeled and applied as an a priori correction. The zenith wet delay component D_{zw} can only be modeled to some extent, and a residual delay ΔD_{zw} is estimated as an additional parameter in the least-squares adjustment. As can be seen from Equation (3.17) and (3.18), a horizontal delay gradient with a north G_{N} and east G_{E} component is estimated as well. Horizontal delay gradient parameters are required to account for systematic errors and random effects due to weather systems (Petit and Luzum, 2010). Combining the components, that can be modeled and the ones that have to be estimated, the tropospheric delay function for line-of-sight observations can be expressed as

$$T_r^s = m_{\mathrm{h}}(e)D_{\mathrm{zh}} + m_{\mathrm{w}}(e)[D_{\mathrm{zw}} + \Delta D_{\mathrm{zw}}] + m_{\mathrm{g}}(e)[G_{\mathrm{N}}\cos\alpha + G_{\mathrm{E}}\sin\alpha], \qquad (3.21)$$

where $m_{\mathrm{h}}(e)$, $m_{\mathrm{w}}(e)$ and $m_{\mathrm{g}}(e)$ are the hydrostatic, wet and gradient mapping functions, e is the elevation angle of the observation direction and a is the azimuth angle of the received signal (Petit and Luzum, 2010).

The terms in the first line on the right-hand side of the observation equations represent the geometrical distance between the satellite and the receiver ρ_r^s, the speed of light c, the clock error of the receiver δ_r and the clock error of the satellite δ^s. The satellite position to be determined and the station position are included in ρ_r^s. Since both the receiver and the satellite clock error are determined in one common least-squares adjustment, the inherent rank deficiency is solved by adding a zero-mean constraint to the transmitter clock parameters at every epoch.

The second line of the observation equations comprises the terms required to correct for the ionospheric delay. $I_{r,j}^{s,(1)}$, $I_{r,j}^{s,(2)}$ and $I_{r,j}^{s,(3)}$ denote the first-, second- and third-order ionospheric terms, respectively. The first-order term accounts for more than 99 % of the ionospheric delay and is typically eliminated by forming linear combinations of multi-frequency observations (Petit and Luzum, 2010). However, neglecting the higher-order terms results in errors of the computed time of propagation, which affects the determination of satellite orbits at the centimeter level (Fritsche et al., 2005). The ionospheric delay is different for code and phase measurements. The ionospheric code correction is positive, delaying the measurement, whereas the ionospheric phase correction is negative, advancing the measurement. The additional terms $I_{r,j}^{s,\mathrm{EPL}}$ and $I_{r,j}^{s,\Delta\mathrm{TEC}}$ account for the excess path length due to the ray curvature of the signal and the range error due to a different slant total electron content (STEC) for different frequencies, respectively (Hoque and Jakowski, 2008). All of the ionospheric terms are functions of STEC, and to correct for the total ionospheric delay, a common STEC parameter is estimated in the least-squares adjustment for all code and phase measurements between a satellite and a receiver at every epoch (Strasser et al., 2019).

As can be seen from Equation (3.17), code biases are estimated per receiver $B_{r,j}$ and transmitter B_j^s for each code signal. A transmitter code bias is set up for every data and pilot component, whereas a receiver code bias is also determined for the combined data + pilot signals (e.g., C1X). The arising rank deficiency from the mutual determination of receiver and transmitter code bias is solved by zero-mean constraints to the transmitter code biases. Code biases cannot be separated from the parameters required for the modeling the ionospheric delay in one common least-squares adjustment, resulting in biased STEC parameters. The approach on how this problem was solved during processing is outlined in Strasser et al. (2019).

The last line of Equation (3.18) includes the receiver phase bias $b_{r,j}$, the transmitter phase bias b_j^s and the integer ambiguities n_j. Ambiguity resolution in the form of a zero-difference method, as necessary for the raw observation approach, requires the determination of phase biases, which are usually eliminated when classic double-difference approaches are used. These biases prevent direct access to integer ambiguities. The integer ambiguity resolution method used at TUG is described in Strasser et al. (2019). A transmitter phase bias is estimated for each frequency and a receiver phase bias is determined for each signal. A zero-mean constraint is applied to the transmitter phase biases to account for the arising rank deficiency when determining both transmitter and receiver phase biases. The residual error term $\epsilon_{r,j}^s$ in Equation (3.17) and (3.18) contains observation noise as well as all not or insufficiently modeled effects such as multipath.

3.7 GROOPS

The Gravity Recovery Object Oriented Programming System (GROOPS) is a software toolkit developed to perform core geodetic tasks, such as gravity field recovery from satellite and terrestrial data, processing of GNSS constellations and ground station networks, determination of satellite orbits from GNSS measurements as well as statistical analysis and visualization of time series and spatial data sets (Mayer-Gürr et al., 2021). Since 2010, GROOPS has been developed and maintained by the working group Theoretical Geodesy and Satellite Geodesy of the Institute of Geodesy at TUG.

The GROOPS software package includes a graphical user interface to set up workflows based on XML configurations files. These configuration files are denoted as programs. Programs perform specific tasks and interact with each other via input and output files. The source code of the GROOPS software is written in C++ and is designed for extensibility. Along with the documentation, guided examples and installation instructions, the source code is publicly available on GitHub (`https://github.com/groops-devs/groops`). For more information about GROOPS refer to Mayer-Gürr et al. (2021).

Solar radiation pressure models

Solar radiation pressure (SRP) is the dominant non-conservative orbit perturbation and the largest error source in GNSS orbit modeling (Rodriguez-Solano, 2014). The acting acceleration depends on the physical and geometrical properties of the satellite, its mass, and its orientation with respect to the incident radiation of the Sun. Non-conservative forces are not acting on the center of mass of the satellite but on its surfaces. In order to model the SRP, information about the dimensions and the optical properties of these surfaces is required. Since the perturbing accelerations correlate with the orientation of the satellite to the Sun, the SRP model has to incorporate the employed attitude model. Three main types of SRP models can be distinguished: analytical models, semi-empirical models and empirical models.

4.1 Analytical models

Analytical models allow for a physical representation of the perturbing accelerations caused by SRP. Since these models are based on details about the satellite structure, they depend on the information provided by the satellite manufacturers. Representatives of analytical SRP models are different versions of the ROCK model (Fliegel et al., 1992) and the box-wing model, originally developed by Marshall and Luthcke (1994).

4.1.1 Box-wing model

By simplifying the satellite structure to a combination of a box and two flat wings representing the satellite bus and the solar panels, the effect of SRP on the satellite can be determined by summarizing the accelerations for each illuminated surface (Wang et al., 2019). Milani et al. (1987) formulated that the acceleration of an illuminated, flat surface in an inertial system can be expressed as:

$$\boldsymbol{a} = -\frac{A}{M}\frac{S_0}{c}\left(\frac{1\text{AU}}{\boldsymbol{r}_\text{D}}\right)^2 \cos\theta \left[(1-\rho)\boldsymbol{e}_\text{D} + 2\left(\frac{\delta}{3} + \rho\cos\theta\right)\boldsymbol{e}_\text{N}\right], \qquad (4.1)$$

where α, ρ and δ denote the optical properties, which represent the fraction of the absorbed, specularly reflected and diffusely reflected photons, respectively. The condition for the optical properties of $\alpha + \rho + \delta = 1$ is implicit. Referring to

Equation (4.1), the dependency of the acceleration on the mass M, the area A and the orientation of the surface to the Sun θ becomes apparent. $\boldsymbol{e}_{\mathrm{D}}$ denotes the unit vector from the satellite to the Sun, $\boldsymbol{e}_{\mathrm{N}}$ denotes the normal vector of the surface and θ is the angle between the two vectors. S_0 is the solar irradiance at 1 astronomical unit (AU) and c is the speed of light in vacuum. The term $\left(\frac{1\mathrm{AU}}{\boldsymbol{r}_{\mathrm{D}}}\right)^2$ is added to the formula to scale the solar irradiance to the current distance of the satellite to the Sun $\boldsymbol{r}_{\mathrm{D}}$. Equation (4.1) can be used for SRP modeling of the solar panels. However, the satellite bus is assumed to be covered with multilayer insulation, a common material in spacecraft design that has zero thermal capacity. According to Rodriguez-Solano et al. (2012), the SRP-induced acceleration can be reformulated for materials with zero thermal capacity as follows:

$$\boldsymbol{a} = -\frac{A}{M}\frac{S_0}{c}\left(\frac{1\mathrm{AU}}{\boldsymbol{r}_{\mathrm{D}}}\right)^2 \cos\theta \left[(\alpha+\delta)\left(\boldsymbol{e}_{\mathrm{D}}+\frac{2}{3}\boldsymbol{e}_{\mathrm{N}}\right) + 2\rho\cos\theta\,\boldsymbol{e}_{\mathrm{N}}\right]. \qquad (4.2)$$

Equation (4.2) can therefore be used for the surfaces of the satellite bus.

The main disadvantage of analytical SRP models is that they highly depend on the metadata of the satellite. Rodriguez-Solano et al. (2012) stated that analytical models are not able to compensate accurately enough for the actual in-orbit behavior of the satellites due to the aging or uncertainty of the a priori optical properties. Information about the spacecraft characteristics, for the most part, is not publicly available with a sufficient level of detail. The BDS-3 metadata was not published up until December 2019, and in terms of optical properties, only the absorption coefficient is listed. Therefore, parameters such as the optical properties are often determined empirically (e.g., Duan et al., 2019).

4.2 Semi-empirical models

An intermediate approach between analytical and empirical SRP models is given by semi-empirical models, which combine the physical understanding of SRP with real satellite tracking measurements (Guo et al., 2017). The shortcoming of the uncertainty of the satellite characteristics can therefore be overcome while maintaining the physical background. An example of a semi-empirical SRP model is the adjustable box-wing model proposed by Rodriguez-Solano et al. (2012). In this model, the optical properties, an additional bias and a rotation lag angle of the solar panels are estimated when the orbits are fitted to the tracking data.

The main disadvantage of the adjustable box-wing model is the strong correlation between the estimated parameters. Additional constraints must be put on most of these parameters in order to achieve reasonable results (Wang et al., 2018a).

4.3 Empirical models

The parameters of empirical models are estimated in the process of orbit determination. They represent the total SRP-induced acceleration and can therefore be used for any kind of satellite without depending on a priori metadata. However, the physical processes causing the perturbations are not taken into account. This results in the loss of the physical understanding of the acting forces and the potential introduction of systematic errors (Rodriguez-Solano, 2014).

4.3.1 ECOM model

The Center for Orbit Determination in Europe (CODE) has developed a widely used empirical SRP model. The Empirical CODE Orbit Model (ECOM) was first introduced by Beutler et al. (1994). It considers up to 9 parameters and was initially used together with an a priori model. The original ECOM with a reduced set of 5 parameters was found to significantly improve the orbit quality (Springer et al., 1999) and has been applied by CODE and other analysis centers of the IGS (Li et al., 2018a; Steigenberger et al., 2015). Initially developed for GPS satellites, the ECOM is also used for other GNSS satellites. However, deficiencies in orbit determination were first identified for GLONASS and later for Galileo, BeiDou and QZSS (Montenbruck et al., 2014).

Since the original ECOM insufficiently parametrizes the orbits of satellites that have a more elongated shape than GPS satellites, Arnold et al. (2015) reassessed the model and introduced an updated version, known as the extended ECOM or ECOM2. The perturbing accelerations caused by SRP are decomposed into three orthogonal directions

$$
\begin{aligned}
\boldsymbol{e}_{\mathrm{D}} &= \frac{\boldsymbol{r}_{\mathrm{S}} - \boldsymbol{r}}{|\boldsymbol{r}_{\mathrm{S}} - \boldsymbol{r}|} \\
\boldsymbol{e}_{\mathrm{Y}} &= -\frac{\boldsymbol{e}_{\mathrm{D}} \times \boldsymbol{r}}{|\boldsymbol{e}_{\mathrm{D}} \times \boldsymbol{r}|} \\
\boldsymbol{e}_{\mathrm{B}} &= \boldsymbol{e}_{\mathrm{D}} \times \boldsymbol{e}_{\mathrm{Y}},
\end{aligned} \tag{4.3}
$$

where $\boldsymbol{r}_{\mathrm{S}}$ is the geocentric position vector of the Sun and $\boldsymbol{r}$ is the geocentric position vector of the satellite. The unit vector $\boldsymbol{e}_{\mathrm{D}}$ is pointing from the satellite to the Sun, $\boldsymbol{e}_{\mathrm{Y}}$ coincides with the rotation axis of the solar panels and $\boldsymbol{e}_{\mathrm{B}}$ completes the orthogonal, right-handed frame. The total perturbing acceleration can be formulated as

$$
\boldsymbol{a}_{\mathrm{SRP}} = \boldsymbol{a}_0 + D(\Delta u)\boldsymbol{e}_{\mathrm{D}} + Y(\Delta u)\boldsymbol{e}_{\mathrm{Y}} + B(\Delta u)\boldsymbol{e}_{\mathrm{B}}, \tag{4.4}
$$

where $\boldsymbol{a}_0$ is an optional a priori model and $\Delta u = u - u_S$ is the difference of the argument of latitude of the satellite u and the Sun u_S in the satellite's orbital plane.

According to Arnold et al. (2015), the components of the extended ECOM can be written as a truncated Fourier series

$$
\begin{aligned}
D(\Delta u) &= D_0 + D_{2,c} \cos 2\Delta u + D_{2,s} \sin 2\Delta u \\
&\quad + D_{4,c} \cos 4\Delta u + D_{4,s} \sin 4\Delta u \\
Y(\Delta u) &= Y_0 \\
B(\Delta u) &= B_0 + B_{1,c} \cos 1\Delta u + B_{1,s} \sin 1\Delta u,
\end{aligned}
\tag{4.5}
$$

where the constant (D_0, Y_0, B_0), the one-cycle-per-revolution (B_1), the two-cycles-per-revolution (D_2) and the four-cycles-per-revolution (D_4) terms represent the SRP coefficients to be estimated. Analogous to its predecessor, the extended ECOM has been specifically designed for yaw-steering (YS) mode. Comparing Equation (4.3) and (2.3), it can be seen that e_Y from the ECOM frame coincides with $e_{y,\mathrm{YS}}$ from the YS frame but points in the opposite direction. Assuming a perfect YS mode, the solar panels are always perpendicular to the satellite-sun vector e_D. Therefore, the resulting acceleration is theoretically constant, and only the satellite body is causing SRP variations (Arnold et al., 2015). Referring to Equation (4.5), the coefficient D_0 represents the acceleration caused by the solar panels, whereas all other coefficients are needed to model the accelerations caused by the satellite body, which is rotating with respect to the Sun. However, this assumption is not true for satellites in orbit-normal (ON) mode, where a fixed yaw angle is maintained, and the SRP acceleration caused by the solar panels depends on the Sun-elevation angle β. In this case, the SRP acceleration is not only acting in the direction from the Sun to the satellite but has an additional component normal to it (Prange et al., 2020). Several studies have identified deficiencies in orbit determination when ECOM-type models are used in ON mode (e.g., Guo et al., 2013; Lou et al., 2014; Prange et al., 2017).

4.3.2 TERM model

In order to overcome the shortcomings of the traditional ECOM models, Prange et al. (2020) developed an empirical model for satellites in ON mode using a different decomposition of the SRP accelerations. The proposed model will be referred to as the TERM model. The SRP accelerations in the TERM system are decomposed into three orthogonal directions

$$
\begin{aligned}
e_{T_3} &= e_D \\
e_{T_2} &= e_D \times e_{T_1} \\
e_{T_1} &= e_D \times e_C,
\end{aligned}
\tag{4.6}
$$

where e_C is the cross-track direction from the local orbital frame (see Equation (2.1)). The positive e_{T_3} axis is pointing towards the Sun, and the so-called terminator plane, spanned by e_{T_1} and e_{T_2}, depicts the light-shadow boundary on a spherical Earth.

**(a)** ECOM system   **(b)** TERM system
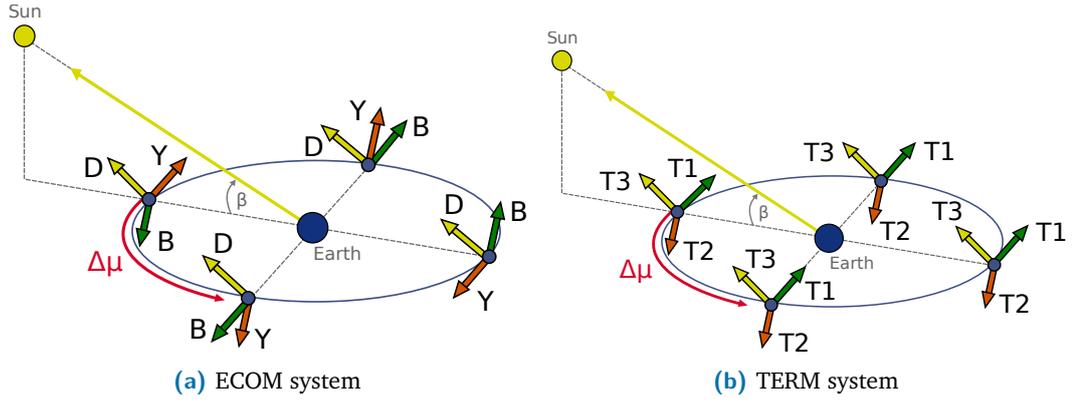
Fig. 4.1: ECOM and TERM coordinate system (based on Prange et al., 2020).

As illustrated in Figure 4.1, the TERM system, in contrast to the ECOM system, does not rotate with the satellite in inertial space. This condition seems obvious, since in ON mode, the satellite is not yawing around the Earth-pointing axis. However, the SRP acceleration caused by the solar panels in ON mode depends on the incident angle of the solar radiation on the satellite, which corresponds to the Sun-elevation angle β. Analogous to Equation (4.4), the total perturbing acceleration can be formulated as

$$\boldsymbol{a}_{\mathrm{SRP}} = \boldsymbol{a}_0 + T1(\Delta u, \beta)\boldsymbol{e}_{\mathrm{T}_1} + T2(\Delta u, \beta)\boldsymbol{e}_{\mathrm{T}_2} + T3(\Delta u, \beta)\boldsymbol{e}_{\mathrm{T}_3}. \tag{4.7}$$

According to Arnold et al. (2015), the absorbed radiation accelerates the satellite in Sun-satellite direction (which corresponds to the reverse $\boldsymbol{e}_{\mathrm{T}_3}$ direction), the specularly reflected radiation is causing an acceleration in the direction of the surface normal (pointing inside the satellite) and the diffusely reflected radiation accelerates the satellite in the direction of a vector lying in the plane spanned by $\boldsymbol{e}_{\mathrm{T}_3}$ and the surface normal. When only the solar panels are taken into account, a minimized parametrization of the TERM model

$$\begin{aligned}
T3(\Delta u, \beta) &= T30C1b \cos\beta \\
T2(\Delta u, \beta) &= T20S2b \sin 3\beta \\
T1(\Delta u, \beta) &= 0
\end{aligned} \tag{4.8}$$

is obtained, where $T2$ is solely caused by the reflected part of the solar radiation and $T3$ is caused by the absorbed and the reflected part (Prange et al., 2020). Both components are constant with respect to the difference of the argument of latitude of the satellite and the sun Δu. If the satellite body is also taken into account, a more complex parametrization of the TERM model was proposed by the authors, where all three components contain significant accelerations depending on β as well

as on Δu. The components of the full TERM model can be written as a truncated Fourier series

$$
\begin{aligned}
T3(\Delta u, \beta) = T30C1b\cos\beta \quad &+ \quad T3C2uC1b\cos 2\Delta u\cos\beta \\
&+ \quad T3S2uC1b\sin 2\Delta u\cos\beta \\
&+ \quad T3C4uC1b\cos 4\Delta u\cos\beta \\
&+ \quad T3S4uC1b\sin 4\Delta u\cos\beta \quad\quad (4.9) \\
T2(\Delta u, \beta) = T20S3b\sin 3\beta \quad &+ \quad T2C2uS2b\cos 2\Delta u\sin 2\beta \\
&+ \quad T2S2uS2b\sin 2\Delta u\sin 2\beta \\
T1(\Delta u, \beta) = \quad\quad\quad\quad\quad &\quad T1S2uC1b\sin 2\Delta u\cos\beta.
\end{aligned}
$$

According to Prange et al. (2020), different versions of the TERM model have been used by CODE during periods with ON mode since Summer 2018.

4.4 SRP model for BeiDou satellites

All of the SRP models mentioned above have advantages and disadvantages and are more or less suitable for different attitude modes. The main challenge is to find the most appropriate model for BeiDou satellites. A common SRP model for all BeiDou satellites is not favorable because of the different orbit types and the distinct behavior of the satellites during certain orbit phases. Accurate modeling of the effects due to SRP in BeiDou orbit determination is complicated by several factors:

- Different attitude modes and orbit types are adopted by the satellites.

- Certain maneuvers are carried out by the satellites when they enter deep eclipse season (continuous yaw-steering (CYS) or change from YS to ON mode)

- The spacecraft structure varies depending on the manufacturer and the satellite type (GEO, IGSO or MEO satellites).

- GEO satellites carry a large C-band antenna, which has to be considered in SRP modeling.

- Satellite surface properties are not known to a sufficient extend to rely on analytical models alone.

Numerical analysis

5

In the previous chapters, the BeiDou Navigation Satellite System (BeiDou) was detailed, the physical and mathematical fundamentals for precise orbit determination of GNSS satellites were described and the different types of solar radiation pressure (SRP) models were presented. In this chapter, real data is used to assess the SRP models and to determine the parametrization best suited for the processing of the BeiDou constellation. Considering the challenges mentioned in Section 4.4, several strategies were examined in the analyses conducted within the scope of this thesis:

- Usage of the extended ECOM with a varying number of coefficients to be estimated.

- Evaluation of the impact of an a priori box-wing model (considering the C-band antenna as an additional surface).

- Usage of the TERM model when satellites are in ON mode and modification of the number of coefficients.

- Determination of additional empirical parameters (piecewise-constant acceleration in the along-track direction).

Section 5.1 gives information about the models used for precise orbit determination and characterizes the requirements for the observation data. In Section 5.2, the influence of an analytical a priori box-wing model gets evaluated and Section 5.3 presents the results and the assessment of the different empirical SRP models.

5.1 Model description and data collection

5.1.1 Orbit preprocessing

Orbit modeling was performed by numerically integrating the perturbed equation of motion, which includes all known forces acting on a satellite (see Section 3.2 and 3.3). The orbits were integrated in the form of 24 h arcs at a 60 s sampling period. The force models used for orbit modeling are summarized in Table 5.4.

Besides the notation of the applied models, also specification values are listed. In the case of forces that were modeled as spherical harmonics, the maximum degree of the series expansion is given. The gravitational model GOCO06s (Kvas et al., 2021) comprises not only a static component but also includes additionally modeled temporal variations in the form of a regularized trend and an annual oscillation. A box-wing model was used to account for earth radiation pressure and solar radiation pressure. This model requires information about the structure and attitude of the satellite. Table 5.1 displays the applied attitude modes of the specific satellite types and the threshold of the Sun-elevation angle β. The value of β indicates when the satellites change their attitude modes or perform midnight and noon maneuvers (see Section 2.5.4). Information about the satellite structure was taken from the official BeiDou document (China Satellite Navigation Office, 2019d).

Tab. 5.1: Attitude modes of the different satellite types.

Satellite block	Attitude mode	β threshold [°]
BeiDou-2G-CAST	orbit-normal	-
BeiDou-2M-CAST	yaw-steering + orbit-normal	4
BeiDou-2I-CAST	yaw-steering + orbit-normal	4
BeiDou-3M-CAST	continuous yaw-steering	3
BeiDou-3M-SECM-A	continuous yaw-steering	3
BeiDou-3M-SECM-B	continuous yaw-steering	3
BeiDou-3I-CAST	continuous yaw-steering	3
BeiDou-3G-CAST	orbit-normal	-

The integrated orbits were fitted to approximate orbits using a standard variational method (see Section 3.5). Hereby, IGS MGEX orbit solutions from GFZ were employed as pseudo-observations to estimate initial values for the state vector and the parameters of the empirical SRP models. The specific parametrizations of the SRP models that were used are depicted in Section 5.3.

5.1.2 Observation preprocessing

The method used for precise orbit determination of BeiDou satellites is a single-system mode, thus all parameters were estimated using only BeiDou observations. No other GNSS were considered in the processing. Different approaches, such as a two-step GPS-assisted method adopted by Lou et al. (2014), which uses GPS observations to determine parameters common to both GNSS and introduces these parameters as known in the BeiDou processing, may benefit from the precision of the GPS parameters. However, the analyses conducted within the scope of this thesis aim to evaluate BeiDou as a standalone system.

Observation data was processed from a selection of IGS14 core stations. A balanced tracking station network is essential to ensure consistent quality of the estimated orbits. Otherwise, orbits would be determined more accurately in regions with a high station density, and more discrepancies would occur in regions with sparse station coverage. However, BeiDou tracking stations are unevenly distributed worldwide, and most of them only support BDS-2. The station network used for the analyses was chosen according to specified criteria:

- The tracking stations should be well-distributed globally.

- A sufficient amount of the stations should support BDS-3.

- Quality and integrity of the tracking data must be ensured.

- The processing time should be reasonable.

The chosen network with 82 stations satisfying the requirements is shown in Figure 5.1. All of these stations were tracking BDS-2 satellites; 47 stations additionally provided BDS-3 tracking data.
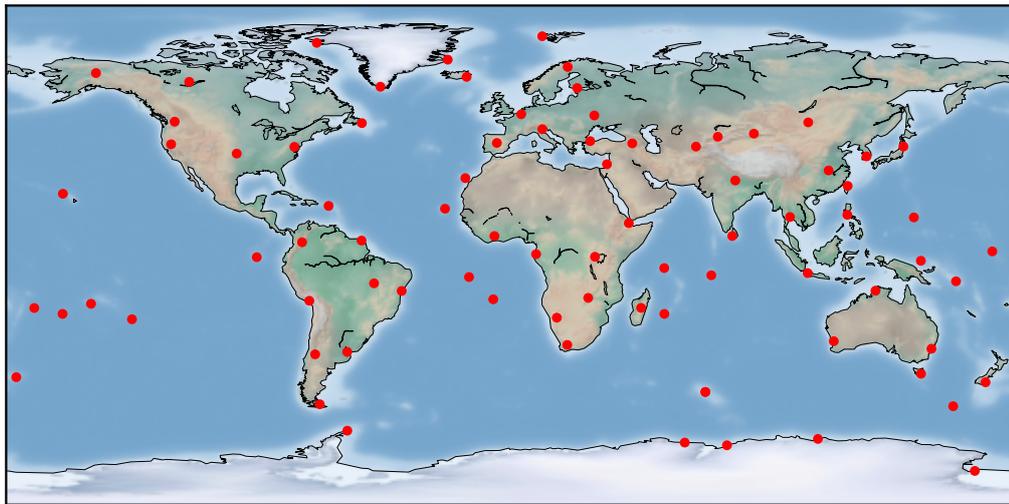
Fig. 5.1: Tracking station network used for processing.

Observation data from the station network over different periods in 2020 with a sampling period of 30 s was used for the analyses. Stations were excluded from processing if more than 25 % of the estimable epochs were missing. Code and phase observations of all open service signals with an elevation angle of more than 5° were used. The initial weighting of the observations depends on the a priori standard

deviation of the code and phase measurement $\sigma_{0,j}$, as well as on the zenith angle z. The respective standard deviation can be determined by

$$\sigma_j(z) = \frac{\sigma_{0,j}}{\cos z}. \tag{5.1}$$

If a station tracked less than five satellites, the specific epochs were not considered. Using the remaining observations, continuous tracks were set up. Two complementary methods were applied for cycle-slip detection for each track based on the Melbourne-Wübbena combination (Melbourne, 1985; Wübbena, 1985) and the geometry-free linear combination (Hauschild, 2017), respectively. A minimum elevation of 15° and at least 30 estimable epochs were required for each track, otherwise it was ignored. Outlier detection was performed track-wise using a robust Huber M-estimator (Huber, 1981; Koch, 1999). The number of satellites of a specific type as well as the received signals used for processing are depicted in Table 5.2. The required settings of the observations and their specifications are listed in Table 5.3.

Tab. 5.2: Number of operational satellites and the received open signals used for processing.

System	Satellite Type	Signals	Satellites
BDS-2	GEO	B1I, B2I, B3I	5
	IGSO	B1I, B2I, B3I	7
	MEO	B1I, B2I, B3I	3
BDS-3	MEO	B1C, B2a, B2b, B2(B2a+B2b), B1I, B3I	24
	IGSO	B1C, B2a, B2b, B2(B2a+B2b), B1I, B3I	3
	GEO	B1C, B2a, B2b, B2(B2a+B2b), B1I, B3I	$2+1^a$

[a]The latest launched BDS-3 satellite is still in testing mode and is not operational yet.

Tab. 5.3: Applied default settings of the observations.

Settings	Specifications
Observation	code + phase
a priori standard deviation	22 cm + 1 mm
Sampling period	30 s
Cutoff elevation	5°
Satellites per station and epoch	≥5
Cycle-slip detection	Melbourne-Wübbena, Geometry-free LC
Min. track elevation	15°
Epochs per track	≥30
Outlier detection	Huber M-estimator

Tab. 5.4: Force models used for precise orbit determination of BeiDou satellites.

Force	Model	Specification	References
Earth's gravitational field (static + trend and annual oscillation)	GOCO06s	$n_{max}^{static} = 60$ $n_{max}^{variable} = 60$	Kvas et al., 2021
Third-body attractions	JPL DE432	Planetary and Lunar ephemerides	Folkner et al., 2014[a]
Solid Earth tides	IERS 2010		Petit and Luzum, 2010
Ocean tides	FES2014b	$n_{max} = 10$	Carrere et al., 2015
Solid Earth pole tides	IERS 2010	linear mean pole	Petit and Luzum, 2010
Ocean pole tides	Desai, 2002	linear mean pole	Desai, 2002
Non-tidal global mass variations	AOD1B RL06	$n_{max} = 60$	Dobslaw et al., 2017
Relativistic effects	IERS 2010		Petit and Luzum, 2010
	Box-wing	a priori model	Rodriguez-Solano, 2014
Solar radiation pressure	ECOM	$n_{DYB} = 7, 9$	Arnold et al., 2015
	TERM	$n_{TERM} = 2, 9$	Prange et al., 2020
Earth radiation pressure	Box-wing	based on CERES data	Rodriguez-Solano, 2009
Antenna thrust	IGS model values	satellite block-specific transmit power	International GNSS Service, 2021d

[a]DE432 is a minor update to DE430 and does not include nutations (*JPL Planetary and Lunar Ephemerides*)

5.1.3 Processing

The processing of the BeiDou constellation was conducted at a 5 min sampling period based on the linearization of the observation equations. Using code and phase observations, updates for the initial state vector and the SRP parameters were estimated in an iterative least-squares adjustment using variational equations. Parameters required for the modeling of systematic influences which could not be corrected adequately in advance were determined, and additional empirical parameters were estimated to overcome force model deficiencies. The additional empirical parameters comprised pseudo-stochastic pulses that were set up at the center of every 24 h arc for each satellite and a piece-wise constant acceleration in the along-track direction that was estimated for the GEO satellites.

The ionospheric delay correction can be divided into first-, second- and third-order terms as well as two terms to account for the excess path length due to signal curvature and a frequency-dependent range error. A common STEC parameter for code and phase measurements was estimated epoch-wise between a satellite and a receiver since all terms are functions of STEC. The third-order term, the excess path length and the range error are nonlinear functions of STEC, and therefore these influences could be corrected from the second iteration onward.

The tropospheric delay was partly modeled a priori and partly estimated in the least-squares adjustment. Hydrostatic and wet mapping functions, as well as discrete values for zenith hydrostatic and zenith wet delay, were provided on a global grid by the Vienna Mapping Functions 3 (VMF3) (Landskron and Böhm, 2018). The approach on how the zenith hydrostatic delay was computed for each station is outlined in Strasser et al. (2019). Meteorological quantities from the empirical Global Pressure and Temperature 3 (GPT3) model on a $1° \times 1°$ grid were used to correct the hydrostatic delay to station height. The zenith wet delay was modeled at grid height since the residual delay was estimated in the least-squares adjustment. Additional horizontal north and east delay gradients were also estimated to account for azimuthal asymmetry. The corresponding gradient mapping function suggested by Chen and Herring (1997) was applied here. Bilinear degree 1 spline interpolation was used to compute the specific delay components per station, with 2-hourly nodes for the zenith wet delay and a constant and trend part for the delay gradients.

Station and satellite clock errors were estimated for every epoch. A transmitter code bias was determined for every data and pilot component of a signal, and a receiver code bias was additionally set up for the combined data + pilot signals for each satellite per day. Receiver phase biases were estimated for each signal and transmitter phase biases were determined for each frequency.

Integer ambiguities had to be resolved to exploit the high precision of phase observations. Ambiguities were initially determined as float values and subsequently decorrelated and fixed to integer values. However, phase biases prevent direct access to integer ambiguities. The approach on how phase biases and integer ambiguities are set up is outlined in Strasser et al. (2019). The integer ambiguity resolution is based on the vectorial integer bootstrapping (VIB) estimator, as described in Teunissen et al. (2021). The implementation algorithm applied at TUG is a blocked search approach, following the least-squares ambiguity decorrelation adjustment (LAMBDA) method. More information about the integer ambiguity resolution used at TUG can be found in Massarweh et al. (2021).

Station positions were not estimated in the processing of the BeiDou constellation, but coordinates from the TUG contribution (Strasser and Mayer-Gürr, 2021) to the third reprocessing campaign of the IGS (repro3) were used. The station position estimates were corrected for sub-daily changes. Solid Earth tides, ocean tides, solid Earth pole tides, ocean pole tides and non-tidal global mass variations were modeled to their maximum degree to account for the station displacement (see Table 5.4). Introducing the station positions as known allows for more focused analyses on the impact of different SRP models and parametrizations on the orbit solutions.

Station coordinates refer to the International Terrestrial Reference System (ITRS), whereas satellite orbits refer to the International Celestial Reference System (ICRS). Earth rotation parameters are required to transform between the two systems. These parameters comprise pole coordinates, the difference between Universal Time (UT1) and Coordinated Universal Time (UTC), as well as two nutation corrections. However, the parameters were not estimated during processing, but they were introduced as known in the form of a time series and the conventional models of the parameters provided by the IERS (Bizouard et al., 2019).

The observations were corrected for phase center offsets (PCOs) and phase center variations (PCVs) a priori. The corresponding values were taken from the IGS metadata files (International GNSS Service, 2021d).

The satellite state, the SRP and all additional parameters were determined in an iterative least-squares adjustment. During this process, the observation weighting was determined from observation residuals and redundancies using variance component estimation (VCE) (Koch, 1999). Due to problems that occurred during the processing of phase observations of the B2b frequency, the respective observations L7D, L7P and L7Z were ignored. Table 5.5 summarizes the parameters which were estimated during the daily processing of the BeiDou constellation.

Tab. 5.5: Parameters to be estimated in the least squares adjustment, when processing a 24 h arc of the BeiDou constellation. An average number of 72 stations received signals on a daily basis, where all of them tracked BDS-2 signals and 40 tracked both BDS-2 and BDS-3 signals.

Parameter		Count	Average
Initial satellite state	$\boldsymbol{y}(t_0)$	$6 \cdot n_{\text{satellite}}$	264
Solar radiation pressure	$\boldsymbol{a}_{\text{SRP}}$	$2 - 9 \cdot n_{\text{satellite}}$	322
Station clock error	δ_r	$n_{\text{epoch}} \cdot n_{\text{station}}$	207360
Satellite clock error	δ^s	$n_{\text{epoch}} \cdot n_{\text{satellite}}$	126720
Slant total electron content	STEC	$n_{\text{obs}}/n_{\text{obs.group}}$	1609744
Tropo. residual wet delay	ΔD_{zw}	$25 \cdot n_{\text{station}}$	1800
Tropo. delay gradient	$G_{\text{N}}, G_{\text{E}}$	$4 \cdot n_{\text{station}}$	288
Receiver code bias	$B_{r,j}$	$n_{\text{code\_signal}} \cdot n_{\text{station}}$	320
Transmitter code bias	B_j^s	$n_{\text{code\_signal}}{}^a \cdot n_{\text{satellite}}$	294
Receiver phase bias	$b_{r,j}$	$n_{\text{phase\_signal}} \cdot n_{\text{station}}$	300
Transmitter phase bias	b_j^s	$n_{\text{freq}} \cdot n_{\text{satellite}}$	170
Ambiguities	n_j	$n_{\text{freq}} \cdot n_{\text{track}}$	20527
Pseudo-stochastic pulse	$\Delta \boldsymbol{v}_{\text{pulse}}$	$3 \cdot n_{\text{satellite}}$	132
Piece-wise const. acc.	$\Delta \boldsymbol{a}_{\text{emp}}$	$1 \cdot n_{\text{GEO}}$	7

[a] A transmitter code bias is set up for the data and pilot component but not for the combined signal

In order to assess the impact of the different SRP models and parametrizations, the root mean square (RMS) of orbit overlap discontinuities at day boundaries was analyzed. The comparison of two consecutive orbit arcs at their common midnight epoch was used to evaluate the internal orbit consistency. This midnight discontinuity RMS indicates how much the last epoch of a 24 h orbit arc differs from the first epoch of the consecutive arc.

5.2 Evaluation of analytical box-wing models

The perturbing acceleration acting on a satellite caused by SRP depends on its mass and attitude as well as on the area and optical properties of the satellite's surfaces (see Equation (4.2)). Information about the effective area and the absorption coefficient of the surfaces were provided by the satellite manufacturers. The geometrical and optical properties are satellite block dependent, which means they are not only different for all satellite types (GEO, IGSO, MEO), but they also vary depending whether the satellite was manufactured by the China Academy of Space Technology (CAST) or the Shanghai Engineering Center for Microsatellites (SECM). Table 5.1 lists the satellite blocks that were distinguished for the box-wing models.

Tab. 5.6: Assignment of BDS-2 and BDS-3 satellites to the respective PRN and SVN.

Satellite type	PRN	SVN	Launch date
	C01	C020	2019-05-17
	C02	C016	2012-10-25
BDS-2 GEO	C03	C018	2016-06-12
	C04	C006	2010-11-01
	C05	C011	2012-02-25
	C06	C005	2010-08-01
	C07	C007	2010-12-18
BDS-2 ISO	C08	C008	2011-04-10
	C09	C009	2011-07-27
	C10	C010	2011-12-02
	C11	C012	2012-04-30
BDS-2 MEO	C12	C013	2012-04-30
	C14	C015	2012-09-19
BDS-2 IGSO	C13	C017	2016-03-30
	C16	C019	2018-07-10

(a) BDS-2 satellites

Satellite type	PRN	SVN	Launch date
	C19	C201	2017-11-05
	C20	C202	2017-11-05
	C21	C206	2018-02-12
	C22	C205	2018-02-12
	C23	C209	2018-07-29
	C24	C210	2018-07-29
	C25	C212	2018-08-25
	C26	C211	2018-08-25
	C27	C203	2018-01-12
BDS-3 MEO	C28	C204	2018-01-12
	C29	C207	2018-03-30
	C30	C208	2018-03-30
	C32	C213	2018-09-19
	C33	C214	2018-09-19
	C34	C216	2018-10-15
	C35	C215	2018-10-15
	C36	C218	2018-11-19
	C37	C219	2018-11-19
	C38	C220	2019-04-20
BDS-3 IGSO	C39	C221	2019-06-25
	C40	C224	2019-11-05
	C41	C227	2019-12-16
	C42	C228	2019-12-16
BDS-3 MEO	C43	C226	2019-11-23
	C44	C225	2019-11-23
	C45	C223	2019-09-23
	C46	C222	2019-09-23
BDS-3 GEO	C59	C217	2018-11-01
	C60	C229	2020-03-09

(b) BDS-3 satellites

The complex structure of the satellite was simplified to a combination of a box and two flat wings. In the case of the GEO satellites, the C-band antenna (see Figure 2.4b) was considered as an additional surface. Similar to the approach stated by Wang et al. (2019), an effective surface area of $3.14\,\mathrm{m}^2$ was assumed. The C-band antenna should point towards the Earth, hence the additional surface was assumed to be perpendicular to the $+z_\mathrm{BF,IGS}$-axis (see Section 2.5.1). Since no information about its optical properties is published, the same values as those for the satellite bus panels perpendicular to $+z_\mathrm{BF,IGS}$ were used. Analogous to the solar panels, the optical properties were set to be equal for the front- and backside of the C-band antenna. The box-wing model was solely used as an a priori model, and therefore the optical properties were not re-estimated during processing, as is the case when using a semi-empirical model such as the adjustable box-wing proposed by Rodriguez-Solano et al. (2012). Effects such as self-shadowing or re-reflection from one satellite surface to another were also not taken into account.

In order to evaluate the overall impact of an a priori box-wing model, the midnight discontinuity RMS was formed over the investigated period from June 1 to December 31, 2020 for each GEO satellite and per satellite type for the IGSO and MEO satellites. An outlier detection using the median and the median absolute deviation was performed to get comparable results. Values greater than the median plus four times the median absolute deviation were considered outliers and rejected. Table 5.7 compares the RMS values of an orbit solution using or omitting an a priori box-wing model. The ECOM model considering 7 parameters was applied for the IGSO and MEO satellites and the TERM model with 9 parameters was used for the GEO satellites (see Table 5.8). An assignment of the satellites to their pseudo-random noise (PRN) and space vehicle number (SVN) is depicted in Table 5.6.

The RMS of the BDS-2 GEO satellites C02 and C03 significantly decreased by almost 25 % using the a priori model, yet the RMS of C01, C04 and C05 increased by 8 % to 10 %. An increase by 8 % and 6 % was determined for the BDS-2 IGSO and BDS-2 MEO satellites. The BDS-3 MEO satellites were further distinguished between satellites C19 to C37 and C41 to C46. This distinction was made since the accuracy of precise orbit determination of the satellites C41 to C46 is worse compared to the other BDS-3 MEO satellites, and the overall RMS would be biased. The degradation of the RMS can be attributed to the smaller number of stations tracking these satellites. While the satellites C19 to C37 were tracked by an average number of 34 stations, only about 16 stations received signals from the satellites C41 to C46. The RMS of the BDS-3 MEO satellites increased by 4 % and 5 % for C19 to C37 and C41 to C46 when using an a priori box-wing model. A significant decrease by 19 % was observed for the BDS-3 IGSO satellites. The RMS of the BDS-3 GEO satellites C59 and C60 remained at the same very high level. The BDS-3 GEO satellite's poor internal orbit consistency is further discussed in Section 5.3.1.

Tab. 5.7: Midnight discontinuity RMS values of the BeiDou GEO, IGSO and MEO satellites using or omitting an a priori box-wing model. The period from June 1 to December 31, 2020 was investigated and an outlier detection using the median and the median absolute deviation was performed. The values are given in cm.

Box-wing model	C01	C02	C03	C04	C05	C59	C60
no	29.7	20.4	20.1	35.7	19.1	356.1	541.4
yes	32.3	15.4	15.5	38.6	21.1	359.9	537.0

(a) Comparison of the GEO satellites.

Box-wing model	IGSO2	MEO2	MEO3 C19-C37	MEO3 C41-C46	IGSO3
no	12.4	5.1	5.2	9.9	22.0
yes	13.4	5.4	5.4	10.4	17.8

(b) Comparison of the IGSO and MEO satellites.

As can be seen in Figure 5.2, using an a priori box-wing model decreased the daily RMS of the midnight discontinuities for all BDS-2 IGSO and MEO satellites (C06 to C16) as well as for BDS-3 MEO satellites C19 to C37 during June, July and August 2020. However, the RMS increased in September, October and November. It seems as if there is a temporal dependency whether the a priori model improves or deteriorates the internal orbit consistency. During the months where the a priori model had a negative impact on the orbit solutions, many orbit planes formed a small angle with the position vector of the Sun β (see Figure 5.3). However, this anomalous impact of the box-wing model cannot be interpreted without speculation at this point. Since only the absorption coefficient α of the surface optical properties was published, it was assumed that the specular reflection coefficient $\rho = 1 - \alpha$ and the diffuse reflection coefficient $\delta = 0$. This assumption may not be true and a semi-empirical approach where the coefficients are re-estimated in the least-squares adjustment may be more accurate.

A particularly positive influence of the box-wing model was assumed for the GEO satellites since the additionally modeled C-band antenna has a similarly large area as the panels of the satellite bus. However, an improvement of the internal orbit consistency could only be verified for C02 and C03. No information about the optical properties of the C-band antenna is currently available and assuming the values to be the same as those of the satellite bus panels may be wrong. The different impact of an a priori model for satellites of the same type was unexpected and requires further investigations.
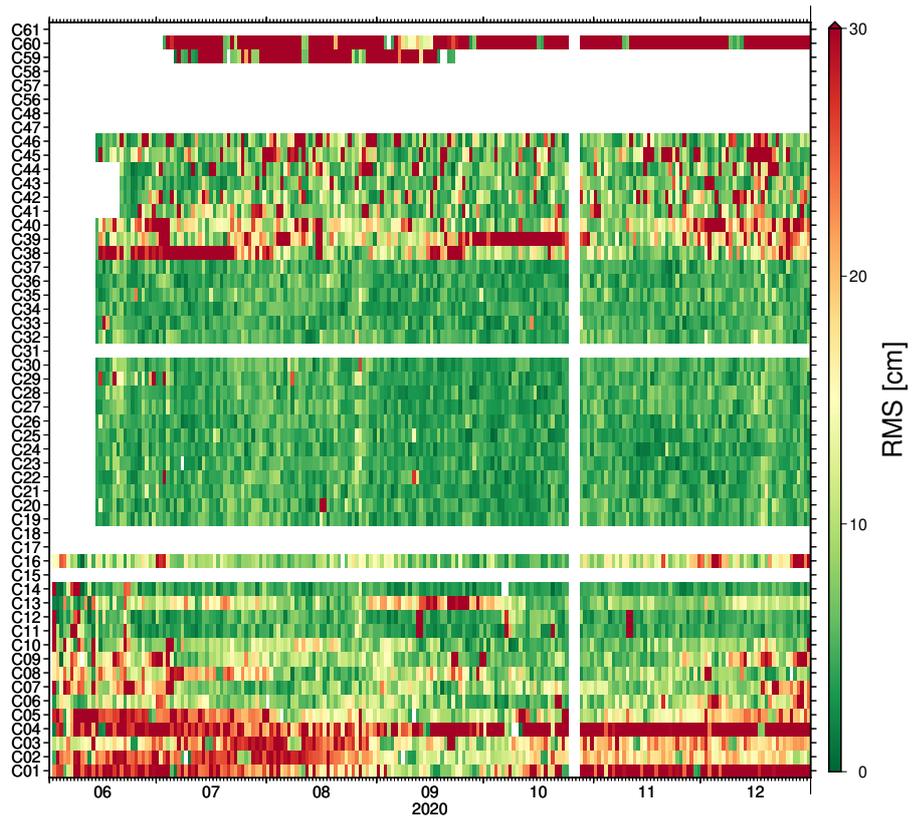
(a) Internal orbit consistency without box-wing model.
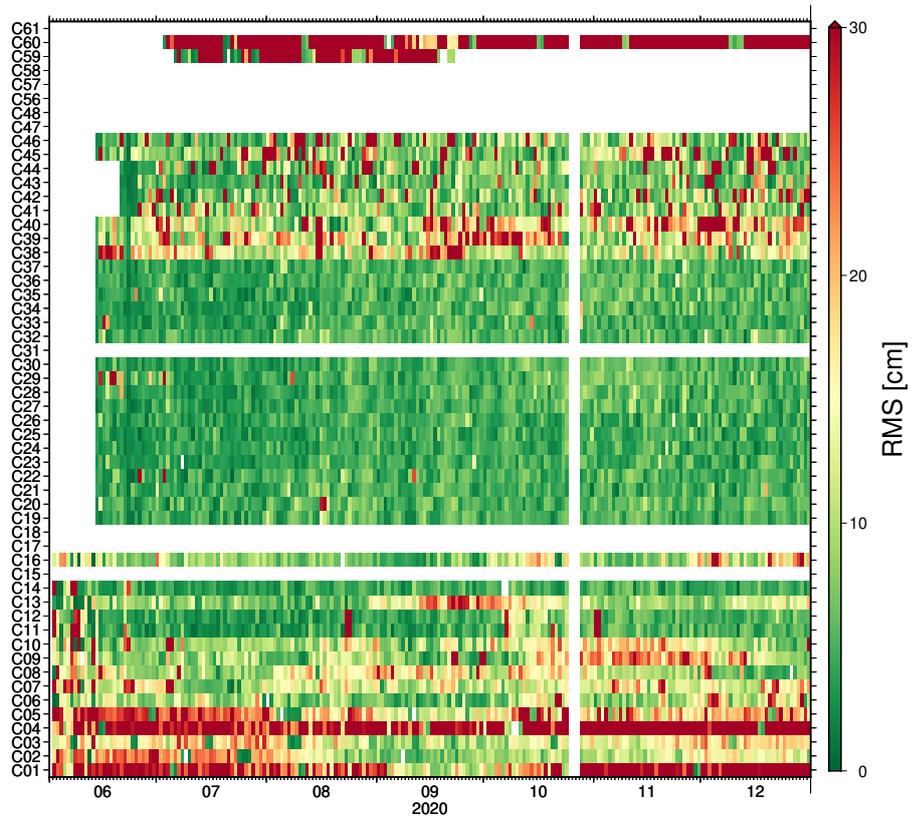
(b) Internal orbit consistency with box-wing model.

Fig. 5.2: Comparison of the midnight discontinuity RMS with and without using an a priori box-wing model during the period from June 1 to December 31, 2020.

Analytical models allow for a physical interpretation of the SRP-induced accelerations acting on the satellite. The a priori box-wing model accounts for systematic effects which cannot be fully represented by the empirical models. The ECOM and TERM models include constant, one-cycle-, two-cycle- and four-cycle-per-revolution terms, depending on the selected parametrization. However, other effects are not considered. Hence the slight degradation of the internal orbit consistency of some satellites was accepted, and the a priori model was used throughout further analyses.

5.3 Evaluation of empirical SRP models

The extended ECOM has been designed for satellites in YS mode and considers up to 9 parameters. In this study, subsets with 5, 7 and 9 parameters were assessed. These parametrizations are subsequently denoted as ECOM5, ECOM7 and ECOM9. The TERM model has been developed for satellites in ON mode and is either parameterized as a minimized version with 2 components (taking only the solar panels into account) or as the full version with 9 components (additionally considering the satellite bus). The minimized TERM model is referred to as TERM2, and the full TERM model as TERM9. The assignment of the parameters of the Equations (4.5), (4.8) and (4.9) to the respective model versions is depicted in Table 5.8.

Tab. 5.8: Parametrization of the empirical ECOM and TERM SRP model.

Parameter	ECOM5	ECOM7	ECOM9
D0	✓	✓	✓
D2	✗	✓	✓
D4	✗	✗	✓
Y0	✓	✓	✓
B0	✓	✓	✓
B1	✓	✓	✓
B2	✗	✗	✗

(a) ECOM SRP model

Parameter	TERM2	TERM9
T1-S2u-C1b	✗	✓
T2-0-S2b	✓	✗
T2-0-S3b	✗	✓
T2-2-S2b	✗	✓
T3-0-C1b	✓	✓
T3-2-C1b	✗	✓
T3-4-C1b	✗	✓

(b) TERM SRP model

Different periods in the second half of 2020 were examined to assess the specific parametrizations of the respective empirical SRP models. The acute angle between the position vector of the Sun and the satellite's orbit plane β is decisive for the adaption of a certain attitude mode. Figure 5.3 illustrates β for all BeiDou satellites from June to December 2020. The condition for satellites in CYS to no longer maintain nominal YS but to perform midnight and noon maneuvers was set to an absolute β angle smaller than 3°. The conditions for a switch between YS mode and ON mode were set to an absolute β angle smaller than 4° and a yaw angle difference of less than 5° between the two attitude modes.
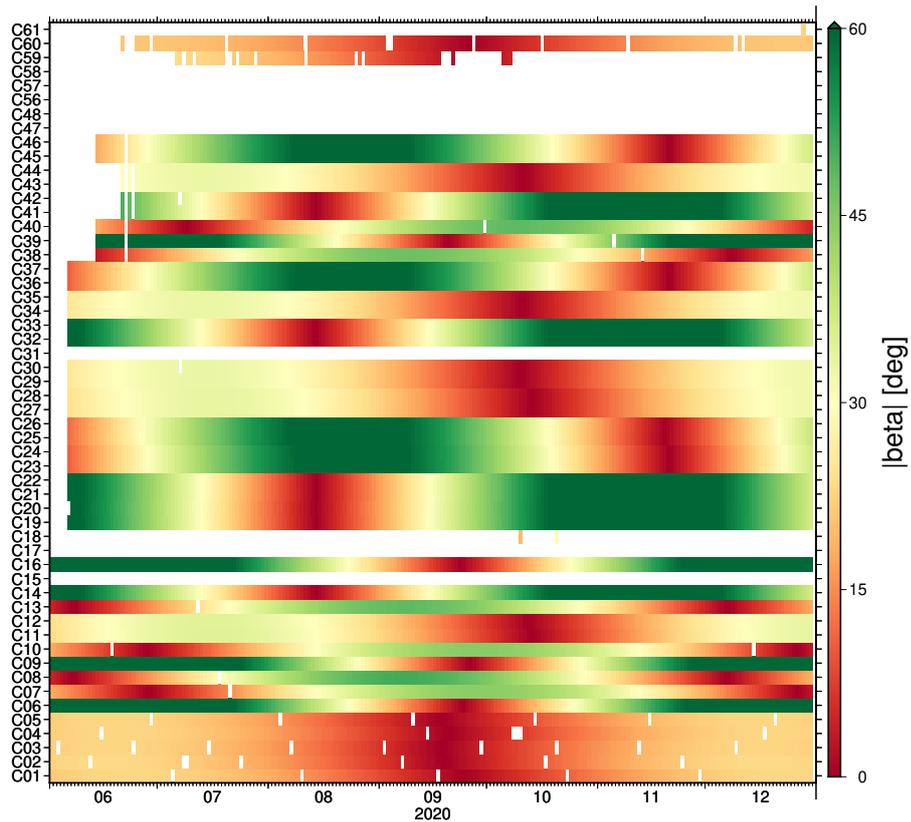
Fig. 5.3: β angle for all BeiDou satellites from June to December 2020.

5.3.1 GEO satellites

BeiDou is unique as a Global Navigation Satellite System (GNSS) in terms of incorporating GEO satellites in its nominal satellite constellation. Five BDS-2 and two BDS-3 GEO satellites are currently operational. However, the accuracy of precise orbit determination is low in comparison to MEO and IGSO satellites. Several studies identified the limiting factors in for the achievable accuracy of GEO satellite orbits (e.g. Steigenberger et al., 2013; Sun et al., 2012; Wang et al., 2019): The high altitude of GEO satellites and the small range of stations that can track those satellites results in a poor observation geometry. Since GEO satellites are positioned almost stationary relative to the tracking stations, small changes of the observation geometry lead to strong correlations among the initial state vector, the SRP parameters, and the ambiguities. Due to a non-zero inclination and gravitational perturbations, regular orbit maneuvers have to be performed to maintain the designated orbits. BeiDou GEO satellites adopt ON mode at all times. The perturbing acceleration due to SRP becomes greater with increasing altitude, yet empirical modeling of SRP in ON mode is more difficult than in YS mode. Additionally, GEO satellites carry a large C-band antenna with an area comparable to the satellite panels.

The BDS-3 GEO satellites C59 and C60 are declared to be operational. However, precise orbit determination of C59 was only possible from July to October 2020. During this time, observations were available on 76 days. So far, the GeoForschungsZentrum (GFZ) is the only IGS analysis center publishing BDS-3 GEO MGEX solutions. When the BDS-3 GEO satellites were examined in this study, very large discrepancies in the internal orbit consistency could be observed. Midnight discontinuity RMS values of C59 were in the order of several meters. Only 4 stations of the network used in this study were tracking this satellite. Observation data of the satellite C60 was available as of mid-June 2020. An average number of 10 stations provided tracking data. However, the internal orbit consistency of C60 was even worse compared to C59. Average midnight discontinuity RMS values of more than 3.6 m and 5.4 m for C59 and C60 indicated that an assessment of the SRP parametrization was not meaningful at this point. No clear distinction could be made among the different SRP models. The assessment of different parametrizations for GEO satellites was therefore restricted to BDS-2 satellites.

Figures 5.4 and 5.5 compare different versions of the ECOM and TERM model as well as the impact of an additional piecewise constant acceleration in the along-track direction, referred to as acceleration bias. On average, 22 stations were tracking the BDS-2 GEO satellites during the investigated period from June 1 to July 31, 2020.

Both ECOM7 and ECOM9 showed midnight discontinuity RMS values of several decimeters to more than one meter. ECOM has been developed for satellites in YS mode and has deficiencies representing SRP-induced accelerations in ON mode. Using the TERM model, an increased internal orbit consistency can be achieved, where TERM9 is best suited for BDS-2 GEO satellites. The satellite C01 showed even larger RMS values using TERM2 than ECOM7 or ECOM9. However, TERM9 significantly decreases the midnight discontinuity RMS of all GEO satellites.

Additionally estimating a constant acceleration in along-track direction was assessed since several studies identified larger along-track RMS values and the main velocity changes due to east-west orbit maneuvers occur in this direction (Steigenberger et al., 2013). As can be seen in Figure 5.5, estimating an acceleration Bias improves the consistency of the C01 TERM2 solution. An overall improvement of the RMS cannot be observed. The RMS level of the TERM9 solution seems to be lifted when the additional parameter is determined.
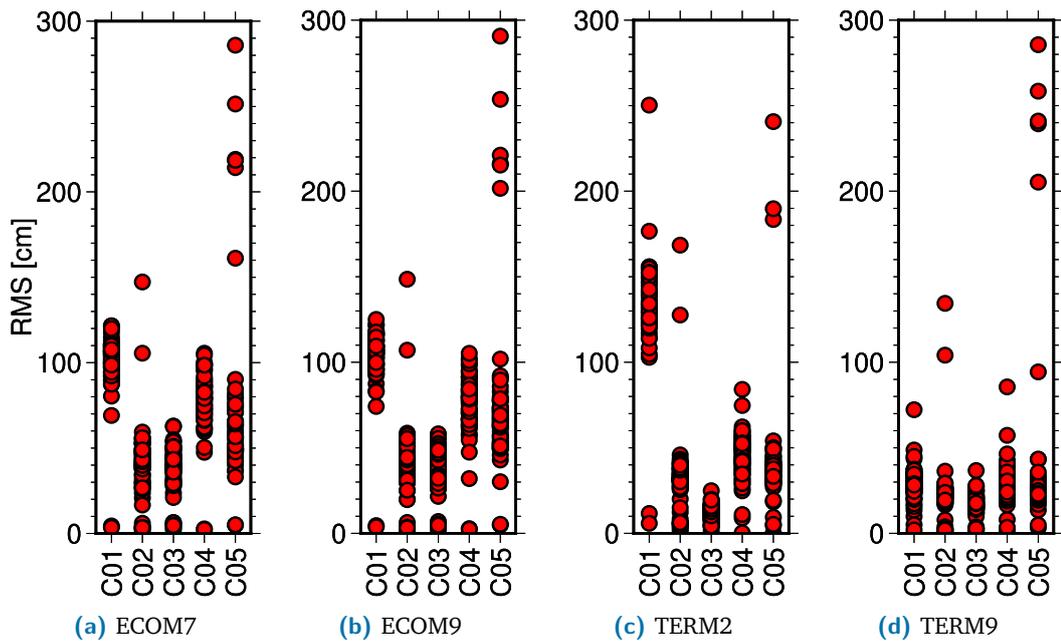
Fig. 5.4: Midnight discontinuity RMS of BDS-2 GEO satellite orbits from June 1 to July 31, 2020; estimated with different parametrizations of the ECOM and TERM model.
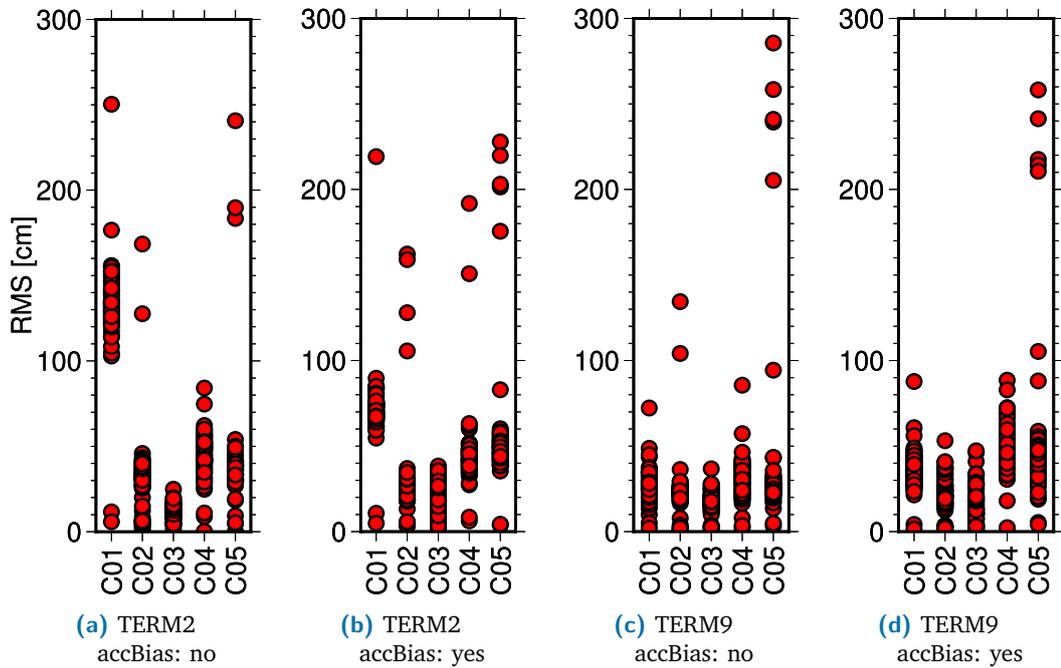
Fig. 5.5: Influence of additionally estimated piecewise-constant acceleration in the along-track direction on precise orbit determination of BDS-2 GEO satellites; evaluated on the basis of midnight discontinuity RMS values from June 1 to July 31, 2020.

5.3.2 IGSO and MEO satellites

The Empirical CODE Orbit Model (ECOM) is widely used for SRP modeling of GNSS satellites. The extended ECOM, as introduced by Arnold et al. (2015), with different subsets of parameters was assessed for all BeiDou MEO and IGSO satellites. Midnight discontinuity RMS values from June 16 to July 31, 2020 were used for evaluation. Three different parametrizations were assessed: ECOM5, ECOM7 and ECOM9, all of them with an a priori box-wing model. The RMS over each satellite type was formed, further distinguishing between BDS-3 MEO satellites C19 to C37 and C41 to C46.

Tab. 5.9: Midnight discontinuity RMS values per satellite block of the different ECOM parametrizations for IGSO and MEO satellites. The period from June 16, 2020 to July 31, 2020 was investigated. The values are given in cm. No outlier detection was performed.

Parametrization	IGSO2	MEO2	MEO3 C19-C37	MEO3 C41-C46	IGSO3
ECOM5	25.0	7.3	8.3	16.6	45.9
ECOM7	15.1	6.2	7.1	17.0	19.2
ECOM9	15.5	6.1	7.1	18.0	25.0

As can be seen from Table 5.9, ECOM7 and ECOM9 show comparable results for all satellite types beside for BDS-3 IGSO satellites. No outliers were removed when the RMS was formed. Estimating a subset of 5 parameters of the ECOM does not seem to be sufficient to fully model the SRP-induced accelerations, yielding the highest RMS values for all satellite types but for MEO satellites C41 to C46. The ECOM7 parametrization significantly reduces the RMS of the BDS-3 IGSO satellites compared to the other parameter subsets. An average number of 16 to 17 stations tracked the MEO satellites C41 to C46. 10 to 11 stations provided data for the BDS-3 IGSO satellites. The higher RMS might be attributed to the smaller amount of data.

As stated by Steigenberger et al. (2013), estimating a smaller subset of parameters generally yields a more robust orbit determination, yet by estimating more parameters, the actual orbit dynamics may be modeled more accurately. Based on the results of this study, the extended ECOM with a subset of seven parameters was found to be most suitable for SRP modeling.

BDS-2 satellites were originally designed to switch from YS to ON mode when they enter deep eclipse season. However, more and more satellites abandon the ON mode in favor of the CYS mode. Xia et al. (2019) examined the yaw mode history during eclipse season using a reverse kinematic precise point positioning approach and inferred that C06 and C14 have changed to CYS mode. The satellites C13 and C16

have adopted CYS since they were launched. Table 5.10 lists the attitude modes employed by the BDS-2 MEO and IGSO satellites, as well as the time when they first used CYS instead of switching from yaw-steering to ON mode.

Tab. 5.10: Attitude modes of BDS-2 IGSO and MEO satellites.

SVN	PRN	Type	Attitude mode	First CYS maneuvers
C005	C06	IGSO	CYS	March, 2017
C007	C07	IGSO	YS-ON	-
C008	C08	IGSO	YS-ON	-
C009	C09	IGSO	YS-ON	-
C010	C10	IGSO	YS-ON	-
C012	C11	MEO	YS-ON	-
C013	C12	MEO	YS-ON	-
C017	C13	IGSO	CYS	June, 2016
C015	C14	MEO	CYS	September, 2017
C019	C16	IGSO	CYS	October, 2018

The impact of using the TERM model in ON mode for satellites that still change their attitude mode in deep eclipse season was assessed. Figure 5.6 shows the midnight discontinuity RMS values as a grid for the BDS-2 MEO and IGSO satellites from June 16 to July 11, 2020. A significant deterioration of the internal orbit consistency from June 22 to July 5 is visible for C07 and C10 when the ECOM model was maintained. In both solutions, the days when the switches were performed have very high RMS values. However, the RMS level in ON mode is significantly lower when the TERM model was applied during this time.

Tab. 5.11: Midnight discontinuity RMS values of BDS-2 IGSO and MEO satellites during ON mode. Comparision of ECOM and TERM parametrizations. The values are given in cm.

Parametrization	C07	C08	C09	C10	C11	C12
ECOM7	39.9	7.0	8.1	16.1	14.2	18.0
TERM2	16.5	6.5	4.5	7.2	33.9	21.3
TERM9	13.2	8.9	5.7	9.0	11.3	12.2

Table 5.11 shows the RMS of all BDS-2 satellites that switch to ON mode in deep eclipse season. The respective periods used for evaluation of the parametrizations ECOM7, TERM2 and TERM9 were: June 25 to July 3 for C07 and C10, December 4 to December 11 for C08, September 24 to September 29 for C09 and October 8 to October 19 for C11 and C12.
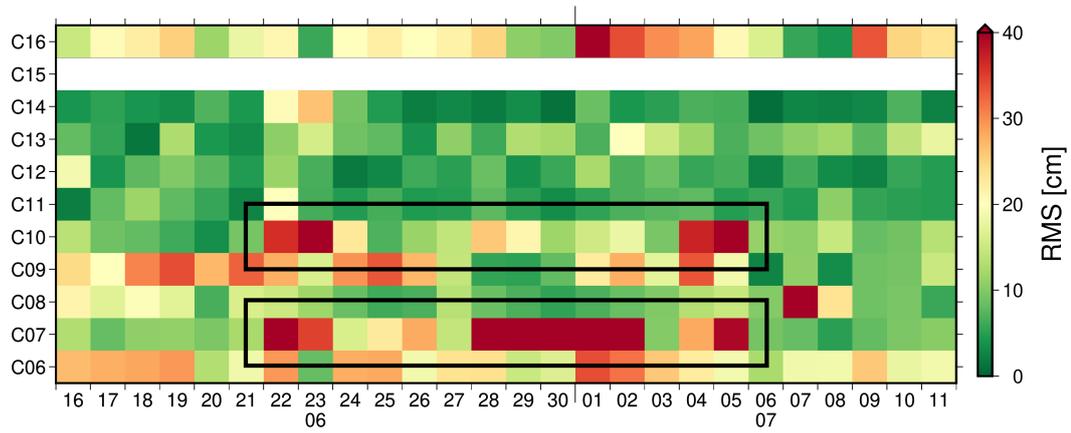
(a) ECOM7 parametrization during ON mode.
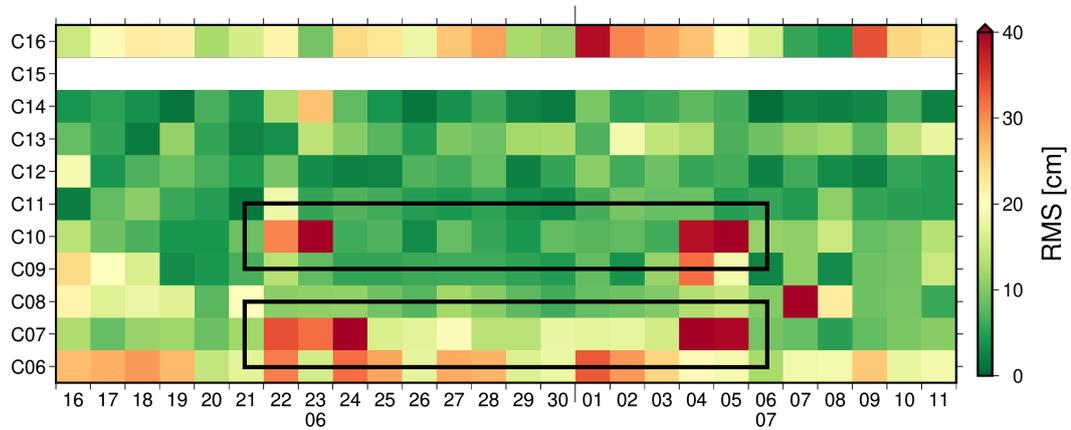
(b) TERM2 parametrization during ON mode.

Fig. 5.6: RMS of midnight discontinuities from August 16, 2020 to September 25 with different parametrizations for the satellites C07 and C10, which are in deep eclipse season during that time.

As can be seen from the values in Table 5.11, the TERM2 parametrization is best suited for BDS-2 IGSO satellites C08, C09 and C10 when using ON mode. However, TERM2 is not applicable for the BDS-2 MEO satellites C11 and C12, yielding the largest RMS values when the satellites changed their attitude mode. The full TERM model with 9 parameters results in the smallest RMS values for the MEO satellites C11 and C12 and the IGSO satellite C07. Comparing the respective TERM parametrization for MEO and IGSO satellites with ECOM7, considerable differences are observed. An improvement by a factor of up to 3 was achieved by using the TERM model. The assumption that ECOM is deficient for modeling SRP for satellites moving in ON mode could be confirmed. Based on the results of this study, the minimized TERM model and the full TERM model are best suited for BDS-2 IGSO and MEO satellites, respectively. These results are in accordance with the findings in Prange et al. (2020).

5.3.3 Comparison with other analysis centers

Based on the analyses conducted within the scope of this thesis, the SRP parametrizations ECOM7 for BeiDou MEO and IGSO satellites adopting YS mode, TERM9 for GEO and MEO satellites in ON mode as well as TERM2 for IGSO satellites in ON mode were found to be most suitable. The time-dependency of the a priori box-wing model demands further research. However, analytical a priori models account for systematic effects which cannot be fully represented by empirical models and therefore were applied in the final solution of this study. Table 5.12 shows the midnight discontinuity RMS values using the described SRP models and the chosen parametrizations when determining all BeiDou satellite types. An outlier detection was performed, rejecting values greater than the median plus four times the median absolute variation.

Tab. 5.12: Overall midnight discontinuity RMS per satellite block from June 16 to December 31, 2020. The values are given in cm. An outlier detection using the median and the median absolute deviation was performed.

GEO2	IGSO2	MEO2	MEO3 C19-C37	MEO3 C41-C46	IGSO3	GEO3
26.2	13.4	5.4	5.4	10.4	17.8	324.6

The European Space Agency (ESA) was the only IGS analysis center that included both midnight epochs in its daily MGEX solution. Hence, it was the only solution that could be used for comparison of the internal orbit consistency. Figure 5.7 shows the RMS values of the orbit overlaps at day boundaries for the ESA and the TUG solution, respectively. ESA only processed BDS-2 MEO and IGSO as well as BDS-3 MEO satellites C19 to C37. For the sake of comparability, only these satellite types were processed in the TUG solution as well. Table 5.13 compares the overall RMS per satellite block of the ESA and TUG solution.

Tab. 5.13: Overall midnight discontinuity RMS of the BDS-2 IGSO, BDS-2 MEO and BDS-3 MEO satellites from June 16 to December 31, 2020. The values from the ESA and the TUG solutions are given in cm.

Instituion	IGSO2	MEO2	MEO3 C19-C37
ESA	12.8	3.0	2.7
TUG	12.1	3.2	3.5
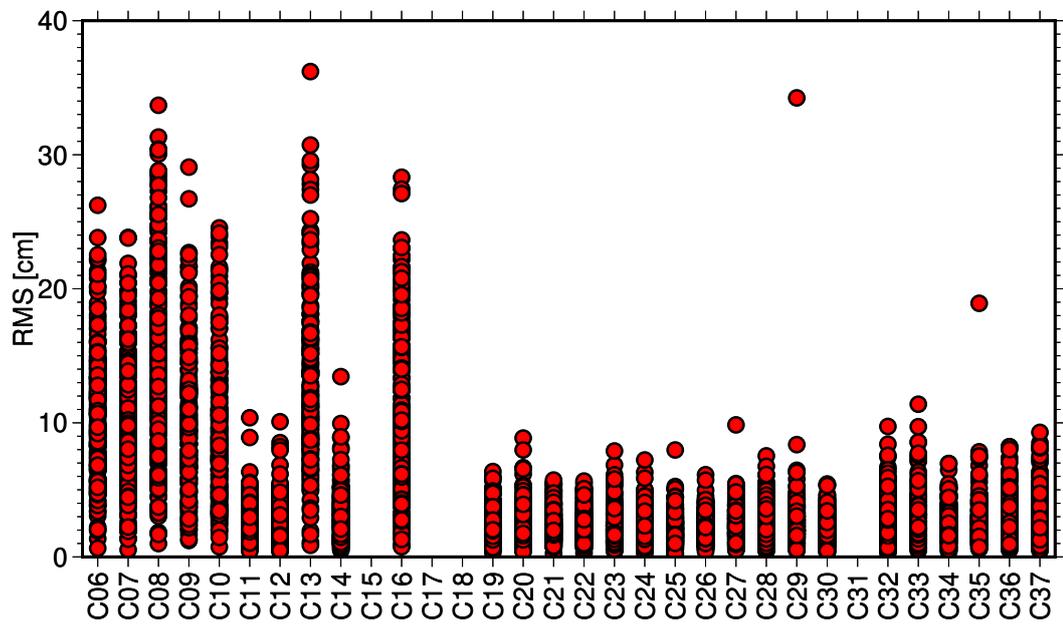
(a) ESA solution
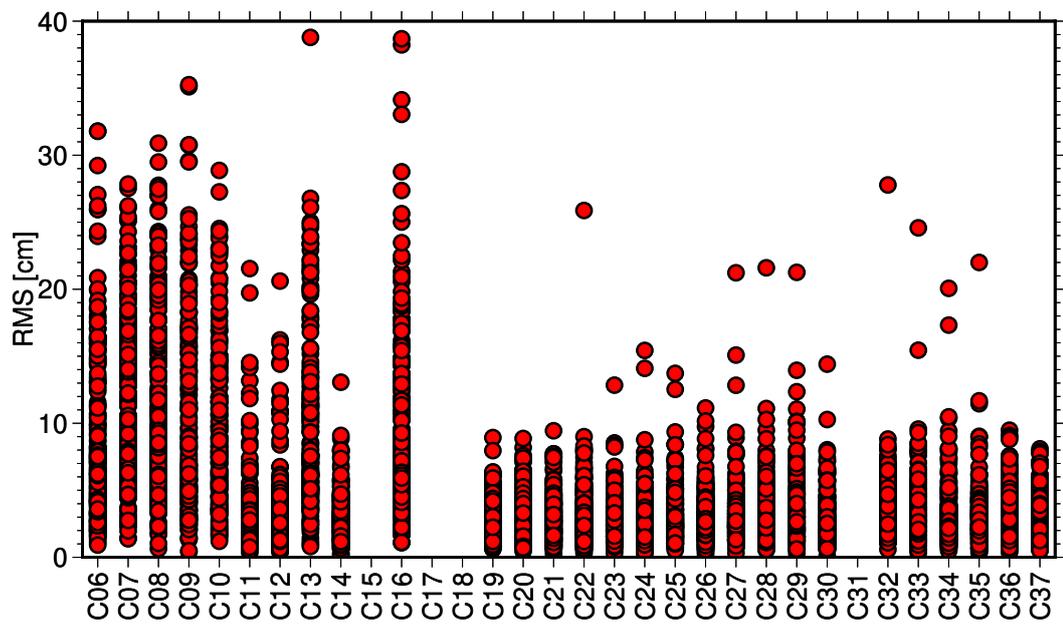
(b) TUG solution

Fig. 5.7: Comparison of the midnight discontinuity RMS values of the ESA and the TUG solution from June 16 to December 31, 2020.

As shown in Figure 5.7, more outliers are present in the TUG solution and the RMS of BDS-3 MEO satellites is higher. The RMS of BDS-2 MEO satellites is comparable to the ESA solution and the internal orbit consistency of the BDS-2 IGSO satellites is slightly better in the TUG solution. This improvement might be attributed to the specific parametrization of the satellites when they change to ON mode. Comparing Tables 5.12 and 5.13, decreased RMS values can be observed. When GEO satellites and BDS-3 satellites that are tracked by a small number of stations were omitted in the processing, the internal orbit consistency of all other determined satellites improved.

The TUG solution was further compared with other IGS analyses centers in terms of 3D orbit differences. The RMS was formed over the orbit differences in radial, along-track and cross-track direction from November 1 to December 31, 2020. This period was chosen since no apparent outliers were detected in any of the solutions. Figure 5.8 shows the respective deviations between TUG and the IGS MGEX analysis centers ESA, GFZ and Wuhan University (WHU).
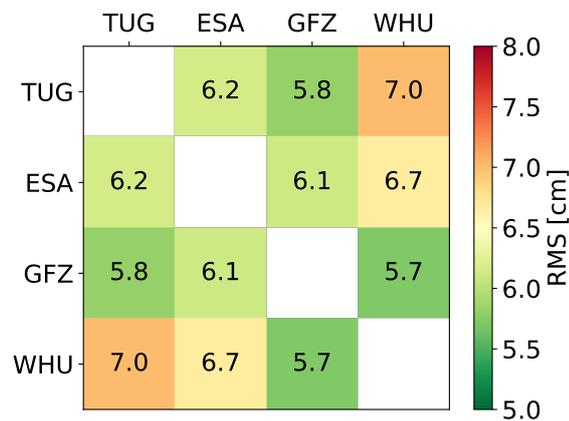
Fig. 5.8: Orbit RMS differences between TUG solution and IGS analysis centers.

The TUG solution fits best to GFZ and matches the WHU solution the least. However, the agreement between the different solutions is at the same level, indicating that the employed processing approach and the proposed SRP parametrization of the TUG solution yield results comparable to solutions from IGS analysis centers.

Summary and outlook

The aim of this thesis was to integrate the BeiDou Navigation Satellite System (BeiDou) into the processing of GNSS constellations applied at Graz University of Technology (TUG), using the Gravity Recovery Object Oriented Programming System (GROOPS) software toolkit. With solar radiation pressure (SRP) being the dominant error source in precise orbit determination, the main focus of this study was on finding an appropriate model for BeiDou. The assessment of different SRP models was complicated by the adoption of different orbit types and attitude modes within the BeiDou constellation and certain maneuvers performed by the satellites during deep eclipse season.

All significant conservative and non-conservative forces acting on the BeiDou satellites were accurately modeled and numerically integrated twice using a moving polynomial method before they were fitted to approximate orbits in the preprocessing step. Processing was based on the raw observation approach (Strasser et al., 2019), which facilitated the incorporation of BeiDou observables due to the renunciation of linear combinations and observation differences.

The Empirical CODE Orbit Model (ECOM) (Arnold et al., 2015), the TERM model (Prange et al., 2020) and an analytical a priori box-wing model (Rodriguez-Solano et al., 2012) were assessed in the course of this study. Various subsets of parameters of the empirical models ECOM and TERM were tested and the impact of the analytical a priori box-wing model was evaluated in the analyses conducted over different periods in the second half of 2020.

The parametrizations found to enhance the internal orbit consistency the most were TERM9 for GEO satellites employing orbit-normal (ON) mode as well as ECOM7 for IGSO and MEO satellites when they adopt yaw-steering (YS) mode. During deep eclipse season, six BDS-2 satellites still switch from YS to ON, whereas four BDS-2 satellites have already abandoned ON mode in favor of the continuous yaw-steering (CYS) mode. The most suitable parametrizations for MEO and IGSO satellites in ON mode were found to be TERM9 and TERM2, respectively.

The analytical box-wing model accounts for systematic effects which cannot be fully represented by the empirical models. The assumption that modeling the biggest part of the SRP induced accelerations a priori using the box-wing model and determining the remaining influences using the empirical models would result in an improved internal orbit consistency could not be verified for all satellites. While some satellites showed significant improvements, the orbit discontinuities of others slightly deteriorated. Furthermore, a temporal dependency on whether the a priori model had a positive or negative impact on the orbit solution was observed. This anomalous influence of the a priori box-wing model requires further investigations.

Applying the respective SRP models with the appropriate set of parameters, RMS values of orbit overlap discontinuities at day boundaries of 26 cm, 13 cm, 5 cm, 5 cm, 10 cm and 18 cm for BDS-2 GEO, BDS-2 IGSO, BDS-2 MEO, BDS-3 MEO and BDS-3 IGSO satellites could be achieved. The evaluation of BDS-3 GEO turned out to be inconclusive. These satellites were only tracked by a small number of stations, and no clear distinction between the SRP models could be found. The final orbit solution was validated against official IGS MGEX products of different analysis centers. The results showed that orbit overlap discontinuities were comparable to those published by the European Space Agency (ESA), and the 3D orbit differences between all considered solutions are at the same level.

BeiDou observation data was processed from a selection of 82 stations of the IGS14 station network. Improved orbit solutions can be expected if a larger station network is used and other GNSS are included in the least-squares adjustment. The integration of well-established GNSS such as GPS would result in improved parameters common to all GNSS, such as receiver clock errors or ionospheric and tropospheric delay parameters. More observing stations would be especially beneficial for BDS-3 IGSO and GEO satellites, which were only tracked by 4 to 11 stations in this study. A promising approach to increasing orbit accuracy is to incorporate inter-satellite link (ISL) measurements. BeiDou satellites launched since March 2015 are equipped with ISL instruments that can measure clock errors and ranges and transfer information between satellites. Yang et al. (2017a) evaluated the combined orbit determination approach and reported substantial accuracy improvements.

Since there are no combined IGS final orbits for BeiDou available yet, this study focused on the internal orbit consistency as evaluation criteria. External orbit validation would be possible with satellite laser ranging (SLR) measurements. However, the processing of SLR observation data is not implemented in the GROOPS software. The issues addressed provide an incentive for further investigations of precise orbit determination of BeiDou satellites and the expansion of the GROOPS software.

Abbreviations

AOD1B	Atmosphere and Ocean De-aliasing Level-1B
ARP	Antenna reference point
AU	Astronomical unit
BDCS	BeiDou Coordinate System
BDS-1	BeiDou Navigation Satellite Demonstration System
BDS-2	BeiDou Regional Navigation Satellite System
BDS-3	BeiDou Global Navigation Satellite System
BDT	BeiDou system time
BeiDou	BeiDou Navigation Satellite System
BIH	Bureau International de l'Heure
BOC	Binary Offset Carrier
BPSK	Binary Phase Shift Keying
CAST	China Academy of Space Technology
CDMA	Code Division Multiple Access
CERES	Clouds and the Earth's Radiant Energy System
CGCS2000	Chinese Geodetic Coordinate System 2000
CHAMP	Challenging Minisatellite Payload
CODE	Center for Orbit Determination in Europe
CTRF2000	China Terrestrial Reference Frame 2000
CYS	Continuous yaw-steering
DFH-3	DongFangHong-3
ECEF	Earth-centered Earth-fixed
ECOM	Empirical CODE Orbit Model
ESA	European Space Agency
FOC	Full Operation Capability

GAS	Ground-based augmentation system
GCRS	Geocentric Celestial Reference System
GEO	Geostationary Earth orbit
GFZ	GeoForschungsZentrum
GLONASS	Globalnaya Navigatsionnaya Sputnikovaya Sistema
GNSS	Global Navigation Satellite System
GOCE	Gravity field and steady-state Ocean Circulation Explorer
GPS	Global Positioning System
GPT3	Global Pressure and Temperature 3
GRACE	Gravity Recovery And Climate Experiment
GRGS	Groupe de Recherche de Géodésie Spatiale
GROOPS	Gravity Recovery Object Oriented Programming System
GSMC	Global short message communication
IAG	International Association of Geodesy
ICGEM	International Centre for Global Earth Models
ICRS	International Celestial Reference System
IERS	International Earth Rotation and Reference Systems Service
IGS	International GNSS Service
IGSO	Inclined geosynchronous orbit
IRNSS	Indian Regional Navigation Satellite System
ISL	Inter-satellite link
ITRF	International Terrestrial Reference Frame
ITRS	International Terrestrial Reference System
LAMBDA	Least-squares ambiguity decorrelation adjustment
LEO	Low Earth orbit
MEO	Medium Earth orbit
MGEX	Multi-GNSS Experiment
NASA	National Aeronautics and Space Administration
NTSC	National Timing Service Center of the Chinese Academy of Science
ON	Orbit-normal
PCO	Phase center offset
PCV	Phase center variation
PHM	Passive hydrogen masers
PNT	Positioning, navigation and timing
PPP	Precise point positioning
PRN	Pseudo-random noise

QMBOC	Quadrature multiplexed Binary Offset Carrier
QPSK	Quadrature Phase Shift Keying
QZSS	Quasi-Zenith Satellite System
RAFS	Rubidium atomic frequency standards
RDSS	Radio determination satellite service
RHCP	Right-Handed Circularly Polarized
RINEX	Receiver Independent Exchange Format
RMS	Root mean square
RNSS	Radio navigation satellite service
RSMC	Regional short message communication
SAR	Search and rescue
SBAS	Satellite-based augmentation system
SECM	Shanghai Engineering Center for Microsatellites
SISRE	Signal in Space Ranging Error
SLR	Satellite laser ranging
SRP	Solar radiation pressure
STEC	Slant total electron content
SVN	Space vehicle number
TFS	Time and frequency system
TUG	Graz University of Technology
TWSTF	Two-way satellite time and frequency transfer
UT1	Universal Time
UTC	Coordinated Universal Time
VCE	Variance component estimation
VIB	Vectorial integer bootstrapping
VMF3	Vienna Mapping Functions 3
WHU	Wuhan University
YS	Yaw-steering

List of Figures

List of Tables

Bibliography

Arnold, D., Meindl, M., Beutler, G., et al. (2015). „CODE's new solar radiation pressure model for GNSS orbit determination". In: *Journal of Geodesy* 89, pp. 775–791. DOI: 10.1007/s00190-015-0814-4.

Bar-Sever, Y. E. (1996). „A new model for GPS yaw attitude". In: *Journal of Geodesy* 70.11, pp. 714–723. ISSN: 09497714. DOI: 10.1007/BF00867149.

Beutler, G. (2005a). *Methods of Celestial Mechanics: Volume I: Physical, Mathematical, and Numeric Principles*. 1st ed. Vol. 1. Springer Berlin Heidelberg. ISBN: 978-3-642-14857-6. DOI: 10.1007/b138225.

– (2005b). *Methods of Celestial Mechanics: Volume II: Application to Planetary System, Geodynamics and Satellite Geodesy*. 1st ed. Springer Berlin Heidelberg. ISBN: 978-3-642-42642-1. DOI: 10.1007/b137725.

Beutler, G., Brockmann, E., Gurtner, W., et al. (1994). „Extended orbit modeling techniques at the CODE processing center of the International GPS Service for Geodynamics (IGS): theory and initial results". In: *Manuscripta Geodaetica* 19.6, pp. 367–386. ISSN: 0340-8825.

Bizouard, C., Lambert, S., Gattano, C., Becker, O., and Richard, J.-Y. (2019). „The IERS EOP 14C04 solution for Earth orientation parameters consistent with ITRF 2014". In: *Journal of Geodesy* 93, pp. 621–633. DOI: 10.1007/s00190-018-1186-3.

Carrere, L., Lyard, F., Cancet, M., et al. (2015). „FES 2014, a new tidal model on the global ocean with enhanced accuracy in shallow seas and in the Arctic region". In: *EGU General Assembly 2015*. Vienna.

Chen, G. and Herring, T. A. (1997). „Effects of atmospheric azimuthal asymmetry on the analysis of space geodetic data". In: *Journal of Geophysical Research: Solid Earth* 102.B9, pp. 20489–20502. ISSN: 2156-2202. DOI: 10.1029/97JB01739.

Chengqi, R. (2012). „Development of the Beidou Navigation Satellite System". In: *Global Navigation Satellite Systems: Report of a Joint Workshop of the National Academy of Engineering and the Chinese Academy of Engineering*. Ed. by L. A. Davis, P. K. Enge, and G. X. Gao. Washington, D.C.: National Academies Press, pp. 17–24. ISBN: 978-0-309-22275-4. DOI: 10.17226/13292.

China Satellite Navigation Office (2013). *BeiDou Navigation Satellite System Open Service Performance Standard (Version 1.0)*. Tech. rep. URL: http://en.beidou.gov.cn/SYSTEMS/Officialdocument/201811/P020181115326719549043.pdf.

China Satellite Navigation Office (2016). *BeiDou Navigation Satellite System Signal In Space Interface Control Document Open Service Signal (Version 2.1)*. Tech. rep. URL: http://en.beidou.gov.cn/SYSTEMS/ICD/201806/P020180608523308843290.pdf.

– (2017a). *BeiDou Navigation Satellite System Signal In Space Interface Control Document Open Service Signal B1C (Version 1.0)*. Tech. rep. URL: http://en.beidou.gov.cn/SYSTEMS/ICD/201806/P020180608519640359959.pdf.

– (2017b). *BeiDou Navigation Satellite System Signal In Space Interface Control Document Open Service Signal B2a (Version 1.0)*. Tech. rep. URL: http://en.beidou.gov.cn/SYSTEMS/ICD/201806/P020180608518432765621.pdf.

– (2017c). *Beidou Timescale Description*. Tech. rep. URL: http://en.beidou.gov.cn/SYSTEMS/Officialdocument/201912/P020191202322231024298.pdf.

– (2018a). *BeiDou Navigation Satellite System Open Service Performance Standard (Version 2.0)*. Tech. rep. URL: http://en.beidou.gov.cn/SYSTEMS/Officialdocument/201812/P020181227424526837905.pdf.

– (2018b). *BeiDou Navigation Satellite System Signal In Space Interface Control Document Open Service Signal B3I (Version 1.0)*. Tech. rep. URL: http://en.beidou.gov.cn/SYSTEMS/ICD/201806/P020180608516798097666.pdf.

– (2019a). *BeiDou Coordinate System Template*. Tech. rep. URL: http://en.beidou.gov.cn/SYSTEMS/Officialdocument/201912/P020191209570814877921.pdf.

– (2019b). *BeiDou Navigation Satellite System Signal In Space Interface Control Document Open Service Signal B1I (Version 3.0)*. Tech. rep. URL: http://en.beidou.gov.cn/SYSTEMS/ICD/201902/P020190227702348791891.pdf.

– (2019c). *Development of the BeiDou Navigation Satellite System (Version 4.0)*. Tech. rep. URL: http://en.beidou.gov.cn/SYSTEMS/Officialdocument/202001/P020200116329195978690.pdf.

– (2019d). *Satellite information of BDS*. URL: http://en.beidou.gov.cn/SYSTEMS/Officialdocument/201912/P020200323536298695483.zip (visited on Dec. 9, 2021).

– (2020a). *BeiDou Navigation Satellite System Signal In Space Interface Control Document Open Service Signal B2b (Version 1.0)*. Tech. rep. URL: http://en.beidou.gov.cn/SYSTEMS/ICD/202008/P020200803539206360377.pdf.

– (2020b). *Completion and Commissioning of the BeiDou Navigation Satellite System (BDS-3)*. URL: http://en.beidou.gov.cn/WHATSNEWS/202008/t20200803_21013.html (visited on Dec. 9, 2021).

– (2020c). *The BDS-3 Constellation Deployment Is Fully Completed Six Months Ahead of Schedule UNOOSA Sends a Congratulation Letter*. URL: http://en.beidou.gov.cn/WHATSNEWS/202006/t20200623_20692.html (visited on Dec. 9, 2021).

– (2021). *Constellation Status*. URL: http://csno-tarc.cn/en/system/constellation (visited on Dec. 9, 2021).

Dai, X., Ge, M., Lou, Y., et al. (2015). „Estimating the yaw-attitude of BDS IGSO and MEO satellites". In: *Journal of Geodesy* 89.10, pp. 1005–1018. ISSN: 14321394. DOI: 10.1007/s00190-015-0829-x.

Desai, S. D. (2002). „Observing the pole tide with satellite altimetry". In: *Journal of Geophysical Research: Oceans* 107.11. DOI: 10.1029/2001JC001224.

Dilssner, F., Schönemann, E., Mayer, V., et al. (2020). *Recent Advances in Galileo and BeiDou Precise Orbit Determination at ESA 's Navigation Support Office*. Tech. rep. 1, pp. 1–27. URL: https://presentations.copernicus.org/EGU2020/EGU2020-18361_presentation.pdf.

Dobslaw, H., Bergmann-Wolf, I., Dill, R., et al. (2017). „A new high-resolution model of non-tidal atmosphere and ocean mass variability for de-aliasing of satellite gravity observations: AOD1B RL06". In: *Geophysical Journal International* 211.1, pp. 263–269. ISSN: 0956-540X. DOI: 10.1093/gji/ggx302.

Dobslaw, H., Flechtner, F., Bergmann-Wolf, I., et al. (2013). „Simulating high-frequency atmosphere-ocean mass variability for dealiasing of satellite gravity observations: AOD1B RL05". In: *Journal of Geophysical Research: Oceans* 118.7, pp. 3704–3711. ISSN: 21699291. DOI: 10.1002/jgrc.20271.

Dow, J. M., Neilan, R. E., and Rizos, C. (2009). „The International GNSS Service in a changing landscape of Global Navigation Satellite Systems". In: *Journal of Geodesy* 83.3-4, pp. 191–198. ISSN: 14321394. DOI: 10.1007/s00190-008-0300-3.

Duan, B., Hugentobler, U., and Selmke, I. (2019). „The adjusted optical properties for Galileo/BeiDou-2/QZS-1 satellites and initial results on BeiDou-3e and QZS-2 satellites". In: *Advances in Space Research* 63.5, pp. 1803–1812. ISSN: 18791948. DOI: 10.1016/j.asr.2018.11.007.

European GNSS Service Centre (2017). *Galileo Satellite Metadata*. URL: https://www.gsc-europa.eu/support-to-developers/galileo-satellite-metadata#2.2 (visited on Dec. 9, 2021).

Fan, L., Jiang, C., and Hu, M. (2017). „Ground track maintenance for BeiDou IGSO satellites subject to tesseral resonances and the luni-solar perturbations". In: *Advances in Space Research* 59.3, pp. 753–761. ISSN: 18791948. DOI: 10.1016/j.asr.2016.09.014.

Fliegel, H. F., Gallini, T. E., and Swift, E. R. (1992). „Global positioning system radiation force model for geodetic applications". In: *Journal of Geophysical Research* 97.B1, pp. 559–568. ISSN: 01480227. DOI: 10.1029/91JB02564.

Folkner, W. M., Williams, J. G., Boggs, D. H., Park, R. S., and Kuchynka, P. (2014). „The Planetary and Lunar Ephemerides DE430 and DE431". In: *IPN Progress Report 42-196*. URL: https://ipnpr.jpl.nasa.gov/progress_report/42-196/196C.pdf.

Fritsche, M., Dietrich, R., Knöfel, C., et al. (2005). „Impact of higher-order ionospheric terms on GPS estimates". In: *Geophysical Research Letters* 32.23, pp. 1–5. DOI: 10.1029/2005GL024342.

Guo, J., Chen, G., Zhao, Q., Liu, J., and Liu, X. (2017). „Comparison of solar radiation pressure models for BDS IGSO and MEO satellites with emphasis on improving orbit quality". In: *GPS Solutions* 21.2, pp. 511–522. ISSN: 15211886. DOI: 10.1007/s10291-016-0540-2.

Guo, J., Xu, X., Zhao, Q., and Liu, J. (2016). „Precise orbit determination for quad-constellation satellites at Wuhan University: strategy, result validation, and comparison". In: *Journal of Geodesy* 90.2, pp. 143–159. ISSN: 14321394. DOI: 10.1007/s00190-015-0862-9.

Guo, J., Zhao, Q., Geng, T., Su, X., and Liu, J. (2013). „Precise Orbit Determination for COM-PASS IGSO Satellites During Yaw Maneuvers“. In: *China Satellite Navigation Conference (CSNC) 2013 Proceedings*. Ed. by J. Sun, W. Jiao, H. Wu, and C. Shi. Berlin, Heidelberg: Springer Berlin Heidelberg, pp. 41–53. ISBN: 978-3-642-37407-4. DOI: `10.1007/978-3-642-37407-4_4`.

Han, C., Cai, Z., Lin, Y., et al. (2013). „Time Synchronization and Performance of BeiDou Satellite Clocks in Orbit“. In: *International Journal of Navigation and Observation* 2013. DOI: `10.1155/2013/371450`.

Han, C., Yang, Y., and Cai, Z. (2011). „BeiDou Navigation Satellite System and its time scales“. In: *Metrologia* 48.4. ISSN: 00261394. DOI: `10.1088/0026-1394/48/4/S13`.

Hauschild, A. (2017). „Combinations of Observations“. In: *Springer Handbook of Global Navigation Satellite Systems*. Ed. by P. J. G. Teunissen and O. Montenbruck. Cham: Springer International Publishing, pp. 583–604. ISBN: 978-3-319-42928-1. DOI: `10.1007/978-3-319-42928-1_20`.

Hofmann-Wellenhof, B., Lichtenegger, H., and Wasle, E. (2007a). „Mathematical models for positioning“. In: *GNSS — Global Navigation Satellite Systems*. Springer Vienna, pp. 161–191. ISBN: 978-3-211-73012-6. DOI: `10.1007/978-3-211-73017-1_6`.

– (2007b). „Observables“. In: *GNSS — Global Navigation Satellite Systems*. Springer Vienna, pp. 105–160. ISBN: 978-3-211-73012-6. DOI: `10.1007/978-3-211-73017-1_5`.

Hofmann-Wellenhof, B. and Moritz, H. (2006). *Physical geodesy (Second, corrected edition)*. Springer, pp. 1–403. DOI: `10.1007/978-3-211-33545-1`.

Hoque, M. M. and Jakowski, N. (2008). „Estimate of higher order ionospheric errors in GNSS positioning“. In: *Radio Science* 43.5. DOI: `10.1029/2007RS003817`.

Huber, P. J. (1981). „Robust Statistics“. In: *Wiley Series in Probability and Mathematics Statistics*. DOI: `10.1002/0471725250`.

Hugentobler, U. and Montenbruck, O. (2017). „Satellite Orbits and Attitude“. In: *Springer Handbook of Global Navigation Satellite Systems*. Ed. by P. J. G. Teunissen and O. Montenbruck. Cham: Springer International Publishing, pp. 59–90. ISBN: 978-3-319-42928-1. DOI: `10.1007/978-3-319-42928-1_3`.

Ince, E. S., Barthelmes, F., Reißland, S., et al. (2019). „ICGEM – 15 years of successful collection and distribution of global gravitational models, associated services, and future plans“. In: *Earth System Science Data* 11.2, pp. 647–674. ISSN: 1866-3516. DOI: `10.5194/essd-11-647-2019`.

International GNSS Service (2021a). *About – International GNSS Service*. URL: `https://www.igs.org/about/` (visited on Dec. 9, 2021).

– (2021b). *Analysis Center Coordinator (ACC) – International GNSS Service*. URL: `https://www.igs.org/acc#analysis-centers` (visited on Dec. 9, 2021).

– (2021c). *MGEX Constellations - BeiDou*. URL: `https://www.igs.org/mgex/constellations/#beidou` (visited on Dec. 9, 2021).

– (2021d). *MGEX Metadata*. URL: `https://igs.org/mgex/metadata/#metadata` (visited on Dec. 9, 2021).

– (2021e). *Network – International GNSS Service*. URL: `https://www.igs.org/network` (visited on Dec. 9, 2021).

Jäggi, A., Hugentobler, U., and Beutler, G. (2006). „Pseudo-stochastic orbit modeling techniques for low-Earth orbiters". In: *Journal of Geodesy* 80.1, pp. 47–60. ISSN: 09497714. DOI: 10.1007/s00190-006-0029-9.

Johnston, G., Riddell, A., and Hausler, G. (2017). „The International GNSS Service". In: *Springer Handbook of Global Navigation Satellite Systems*. Ed. by P. Teunissen and O. Montenbruck. Springer, pp. 967–982. ISBN: 978-3-319-42928-1. DOI: 10.1007/978-3-319-42928-1_33.

Koch, K.-R. (1999). *Parameter Estimation and Hypothesis Testing in Linear Models*. Springer Berlin Heidelberg. DOI: 10.1007/978-3-662-03976-2.

Kouba, J. (2009). „A simplified yaw-attitude model for eclipsing GPS satellites". In: *GPS Solutions* 13.1, pp. 1–12. ISSN: 10805370. DOI: 10.1007/s10291-008-0092-1.

Kvas, A., Brockmann, J. M., Krauss, S., et al. (2021). „GOCO06s – a satellite-only global gravity field model". In: *Earth System Science Data* 13.1, pp. 99–118. DOI: 10.5194/essd-13-99-2021.

Landskron, D. and Böhm, J. (2018). „VMF3/GPT3: refined discrete and empirical troposphere mapping functions". In: *Journal of Geodesy* 92.4, pp. 349–360. ISSN: 14321394. DOI: 10.1007/s00190-017-1066-2.

Li, J., Yang, Y., He, H., and Guo, H. (2017). „An analytical study on the carrier-phase linear combinations for triple-frequency GNSS". In: *Journal of Geodesy* 91.2, pp. 151–166. ISSN: 14321394. DOI: 10.1007/s00190-016-0945-2.

Li, X., Guo, R., Hu, X., et al. (2018a). „Construction of a BDSPHERE solar radiation pressure model for BeiDou GEOs at vernal and autumn equinox periods". In: *Advances in Space Research* 62.7, pp. 1717–1727. ISSN: 18791948. DOI: 10.1016/j.asr.2018.06.038.

Li, X., Hu, X., Guo, R., et al. (2018b). „Orbit and Positioning Accuracy for New Generation Beidou Satellites during the Earth Eclipsing Period". In: *Journal of Navigation* 71.5, pp. 1069–1087. ISSN: 14697785. DOI: 10.1017/S0373463318000103.

Lou, Y., Liu, Y., Shi, C., Yao, X., and Zheng, F. (2014). „Precise orbit determination of BeiDou constellation based on BETS and MGEX network". In: *Scientific Reports* 4, pp. 2–11. ISSN: 20452322. DOI: 10.1038/srep04692.

Marshall, J. A. and Luthcke, S. B. (1994). „Modeling radiation forces acting on topex/poseidon for precision orbit determination". In: *Journal of Spacecraft and Rockets* 31.1, pp. 99–105. ISSN: 00224650. DOI: 10.2514/3.26408.

Massarweh, L., Strasser, S., and Mayer-Gürr, T. (2021). „On vectorial integer bootstrapping implementations in the estimation of satellite orbits and clocks based on small global networks". In: *Advances in Space Research*. ISSN: 0273-1177. DOI: 10.1016/J.ASR.2021.09.023.

Mayer-Gürr, T., Behzadpour, S., Eicker, A., et al. (2021). „GROOPS: A software toolkit for gravity field recovery and GNSS processing". In: *Computers and Geosciences* 155.June. ISSN: 00983004. DOI: 10.1016/j.cageo.2021.104864.

Melbourne, W. G. (1985). „The case for ranging in GPS-based geodetic systems". In: *Proceedings of the first international symposium on precise positioning with the Global Positioning System*. Volume I. Rockville, Maryland: International Union of Geodesy and Geophysics, pp. 373–386.

Milani, A., Nobili, A. M., and Farinella, P. (1987). *Non-gravitational perturbations and satellite geodesy.* Adam Hilger Ltd. ISBN: 0-85274-538-9.

Montenbruck, O. (2017). „Space Applications". In: *Springer Handbook of Global Navigation Satellite Systems*. Ed. by P. J. G. Teunissen and O. Montenbruck. Springer International Publishing, pp. 933–964. ISBN: 978-3-319-42928-1. DOI: 10.1007/978-3-319-42928-1_32.

Montenbruck, O. and Gill, E. (2000). *Satellite Orbits: Models, Methods and Applications*. 1st ed. Springer Berlin Heidelberg. ISBN: 978-3-642-58351-3. DOI: 10.1007/978-3-642-58351-3.

Montenbruck, O., Schmid, R., Mercier, F., et al. (2015). „GNSS satellite geometry and attitude models". In: *Advances in Space Research* 56.6, pp. 1015–1029. ISSN: 18791948. DOI: 10.1016/j.asr.2015.06.019.

Montenbruck, O., Steigenberger, P., Khachikyan, R., et al. (2014). „IGS-MGEX Preparing the Ground for Multi-Constellation GNSS Science". In: *Inside GNSS* January/February, pp. 42–49. URL: http://www.insidegnss.com/auto/janfeb14-MONTENBRUCK.pdf.

Montenbruck, O., Van Helleputte, T., Kroes, R., and Gill, E. (2005). „Reduced dynamic orbit determination using GPS code and carrier measurements". In: *Aerospace Science and Technology* 9.3, pp. 261–271. ISSN: 12709638. DOI: 10.1016/j.ast.2005.01.003.

Park, R. S. *JPL Planetary and Lunar Ephemerides*. URL: https://ssd.jpl.nasa.gov/planets/eph_export.html (visited on Dec. 9, 2021).

Petit, G. and Luzum, B. (2010). „IERS Conventions (2010)". In: *IERS Technical Note No. 36*. URL: http://www.iers.org/TN36/.

Prange, L., Beutler, G., Dach, R., et al. (2020). „An empirical solar radiation pressure model for satellites moving in the orbit-normal mode". In: *Advances in Space Research* 65.1, pp. 235–250. ISSN: 18791948. DOI: 10.1016/j.asr.2019.07.031.

Prange, L., Orliac, E., Dach, R., et al. (2017). „CODE's five-system orbit and clock solution—the challenges of multi-GNSS data analysis". In: *Journal of Geodesy* 91.4, pp. 345–360. ISSN: 14321394. DOI: 10.1007/s00190-016-0968-8.

Rodriguez-Solano, C. J. (2009). *Impact of albedo modelling on GPS orbits (MSc thesis)*. Technische Universität München. URL: https://mediatum.ub.tum.de/doc/1368717/file.pdf.

– (2014). *Impact of non-conservative force modeling on GNSS satellite orbits and global solutions (PhD thesis)*. Technische Universität München.

Rodriguez-Solano, C. J., Hugentobler, U., and Steigenberger, P. (2012). „Adjustable box-wing model for solar radiation pressure impacting GPS satellites". In: *Advances in Space Research* 49.7, pp. 1113–1128. ISSN: 18791948. DOI: 10.1016/j.asr.2012.01.016.

Romero, I. (2020). *The Receiver Independent Exchange Format Version 3.05*. Tech. rep. Darmstadt, Germany: ESA/ESOC/Navigation Support Office. URL: https://files.igs.org/pub/data/format/rinex305.pdf.

Schönemann, E. (2013). *Analysis of GNSS raw observations in PPP solutions (PhD thesis)*. 42. Technische Universität Darmstadt. ISBN: 978-3-935631-31-0. URL: http://tuprints.ulb.tu-darmstadt.de/3843/.

Schönemann, E., Becker, M., and Springer, T. A. (2011). „A new Approach for GNSS Analysis in a Multi-GNSS and Multi-Signal Environment". In: *Journal of Geodetic Science* 1.3, pp. 204–214. ISSN: 2081-9919. DOI: 10.2478/v10156-010-0023-2.

Springer, T. A., Beutler, G., and Rothacher, M. (1999). „Improving the orbit estimates of GPS satellites". In: *Journal of Geodesy* 73.3, pp. 147–157. ISSN: 09497714. DOI: 10.1007/s001900050230.

Steigenberger, P., Hugentobler, U., Hauschild, A., and Montenbruck, O. (2013). „Orbit and clock analysis of Compass GEO and IGSO satellites". In: *Journal of Geodesy* 87.6, pp. 515–525. ISSN: 09497714. DOI: 10.1007/s00190-013-0625-4.

Steigenberger, P., Hugentobler, U., Loyer, S., et al. (2015). „Galileo orbit and clock quality of the IGS Multi-GNSS Experiment". In: *Advances in Space Research* 55.1, pp. 269–281. ISSN: 18791948. DOI: 10.1016/j.asr.2014.06.030.

Strasser, S. (2016). *Precise orbit determination of GNSS satellites using the raw observation approach (MSc thesis)*. Graz University of Technology.

Strasser, S. and Mayer-Gürr, T. (2021). *IGS repro3 products by Graz University of Technology (TUG): Station coordinates (Version v1) [Data set]*. DOI: 10.3217/dataset-3682-0318-2418. URL: https://repository.tugraz.at/records/ewd1h-pnv89 (visited on Dec. 9, 2021).

Strasser, S., Mayer-Gürr, T., and Zehentner, N. (2019). „Processing of GNSS constellations and ground station networks using the raw observation approach". In: *Journal of Geodesy* 93.7, pp. 1045–1057. ISSN: 14321394. DOI: 10.1007/s00190-018-1223-2.

Sun, F. P., Liu, S., Zhu, X. H., and Men, B. H. (2012). „Research and progress of Beidou satellite navigation system". In: *Science China Information Sciences* 55.12, pp. 2899–2907. ISSN: 1674733X. DOI: 10.1007/s11432-012-4724-2.

Švehla, D. and Rothacher, M. (2005). „Kinematic Precise Orbit Determination for Gravity Field Determination". In: *A Window on the Future of Geodesy*. Ed. by F. Sansò. Berlin, Heidelberg: Springer Berlin Heidelberg, pp. 181–188. ISBN: 978-3-540-27432-2. DOI: 10.1007/3-540-27432-4_32.

Swatschina, P. (2012). *Dynamic and Reduced-Dynamic Precise Orbit Determination of Satellites in Low Earth Orbits (Phd thesis)*. 89. Technische Universität Wien. URL: http://publik.tuwien.ac.at/files/PubDat_219297.pdf.

Teunissen, P., Massarweh, L., and Verhagen, S. (2021). „Vectorial integer bootstrapping: flexible integer estimation with application to GNSS". In: *Journal of Geodesy 2021* 95.99, pp. 1–14. ISSN: 1432-1394. DOI: 10.1007/S00190-021-01552-2.

Wang, C., Guo, J., Zhao, Q., and Liu, J. (2018a). „Solar radiation pressure models for BeiDou-3 I2-S satellite: Comparison and augmentation". In: *Remote Sensing* 10.1, pp. 1–11. ISSN: 20724292. DOI: 10.3390/rs10010118.

– (2018b). „Yaw attitude modeling for BeiDou I06 and BeiDou-3 satellites". In: *GPS Solutions* 22.4, pp. 1–10. ISSN: 15211886. DOI: 10.1007/s10291-018-0783-1.

– (2019). „Empirically derived model of solar radiation pressure for BeiDou GEO satellites". In: *Journal of Geodesy* 93.6, pp. 791–807. ISSN: 14321394. DOI: 10.1007/s00190-018-1199-y.

Wu, J. T., Wu, S. C., Hajj, G. A., Bertiger, W. I., and Lichten, S. M. (1992). „Effects of antenna orientation on GPS carrier phase". In: *Astrodynamics 1991*, pp. 1647–1660. URL: https://ui.adsabs.harvard.edu/abs/1992asdy.conf.1647W.

Wu, S. C., Yunck, T. P., and Thornton, C. L. (1991). „Reduced-dynamic technique for precise orbit determination of low earth satellites". In: *Journal of Guidance, Control, and Dynamics* 14.1, pp. 24–30. ISSN: 07315090. DOI: 10.2514/3.20600.

Wu, Z., Zhou, S., Hu, X., et al. (2018). „Performance of the BDS3 experimental satellite passive hydrogen maser". In: *GPS Solutions* 22.2, p. 43. ISSN: 15211886. DOI: 10.1007/s10291-018-0706-1.

Wübbena, G. (1985). „Software developments for geodetic positioning with GPS using TI 4100 code and carrier measurements". In: *Proceedings of the first international symposium on precise positioning with the Global Positioning System*. International Union of Geodesy and Geophysics, pp. 403–412.

Xia, F., Ye, S., Chen, D., and Jiang, N. (2019). „Observation of BDS-2 IGSO/MEOs yaw-attitude behavior during eclipse seasons". In: *GPS Solutions* 23.3. ISSN: 15211886. DOI: 10.1007/s10291-019-0857-8.

Xie, J., Wang, J., and Mi, H. (2012). *Analysis of Beidou navigation satellites in-orbit state*. Vol. 161 LNEE, pp. 111–122. ISBN: 9783642291920. DOI: 10.1007/978-3-642-29193-7_10.

Yang, D., Yang, J., Li, G., Zhou, Y., and Tang, C. (2017a). „Globalization highlight: orbit determination using BeiDou inter-satellite ranging measurements". In: *GPS Solutions* 21.3, pp. 1395–1404. ISSN: 15211886. DOI: 10.1007/s10291-017-0626-5.

Yang, Y. (2009). „Chinese geodetic coordinate system 2000". In: *Chinese Sci Bull* 54, pp. 2714–2721. DOI: 10.1007/s11434-009-0342-9.

Yang, Y., Gao, W., Guo, S., Mao, Y., and Yang, Y. (2019a). „Introduction to BeiDou-3 navigation satellite system". In: *Navigation, Journal of the Institute of Navigation* 66.1, pp. 7–18. ISSN: 00281522. DOI: 10.1002/navi.291.

Yang, Y., Li, J., Xu, J., et al. (2011). „Contribution of the Compass satellite navigation system to global PNT users". In: *Chinese Science Bulletin* 56.26, pp. 2813–2819. ISSN: 10016538. DOI: 10.1007/s11434-011-4627-4.

Yang, Y., Tang, J., and Montenbruck, O. (2017b). „Chinese Navigation Satellite Systems". In: *Springer Handbook of Global Navigation Satellite Systems*. Ed. by P. J. G. Teunissen and O. Montenbruck. Springer, pp. 273–304. DOI: 10.1007/978-3-319-42928-1_10.

Yang, Y., Xu, Y., Li, J., and Yang, C. (2018). „Progress and performance evaluation of BeiDou global navigation satellite system: Data analysis based on BDS-3 demonstration system". In: *Science China Earth Sciences* 61.5, pp. 614–624. ISSN: 18691897. DOI: 10.1007/s11430-017-9186-9.

Yang, Y., Yang, Y., Hu, X., et al. (2019b). „Inter-Satellite Link Enhanced Orbit Determination for BeiDou-3". In: *The Journal of Navigation*, pp. 1–16. DOI: 10.1017/S0373463319000523.

Yunck, T. P., Wu, S. C., Wu, J. T., and Thornton, C. L. (1990). „Precise Tracking of Remote Sensing Satellites With the Global Positioning System". In: *IEEE Transactions on Geoscience and Remote Sensing* 28.1, pp. 108–116. ISSN: 15580644. DOI: 10.1109/36.45753.

Zehentner, N. and Mayer-Gürr, T. (2014). „New Approach to Estimate Time Variable Gravity Fields from High-Low Satellite Tracking Data". In: *Gravity, Geoid and Height Systems*. Ed. by U. Marti. Cham: Springer International Publishing, pp. 111–116. ISBN: 978-3-319-10837-7.

– (2015). „Precise orbit determination based on raw GPS measurements". In: *Journal of Geodesy* 90.3, pp. 275–286. ISSN: 14321394. DOI: 10.1007/s00190-015-0872-7.

Zhang, X., Wu, M., Liu, W., et al. (2017). „Initial assessment of the COMPASS/ BeiDou-3: new-generation navigation signals". In: *Journal of Geodesy* 91.10, pp. 1225–1240. ISSN: 14321394. DOI: 10.1007/s00190-017-1020-3.

Zhang, Z., Li, B., Nie, L., et al. (2019). „Initial assessment of BeiDou-3 global navigation satellite system: signal quality, RTK and PPP". In: *GPS Solutions* 23.4, pp. 1–12. ISSN: 15211886. DOI: 10.1007/s10291-019-0905-4.

Zhao, Q., Wang, C., Guo, J., Wang, B., and Liu, J. (2018). „Precise orbit and clock determination for BeiDou-3 experimental satellites with yaw attitude analysis". In: *GPS Solutions* 22.1, pp. 1–13. ISSN: 15211886. DOI: 10.1007/s10291-017-0673-y.

Ziebart, M., Edwards, S., Adhya, S., et al. (2004). „High Precision GPS IIR Orbit Prediction using Analytical Non-conservative Force Models". In: *Proceedings of the 17th International Technical Meeting of the Satellite Division of The Institute of Navigation (ION GNSS 2004)*, pp. 1764–1770.